DETECTION AND TRACKING OF RADAR TARGETS WITH IN-BAND COMMUNICATION INTERFERENCE FOR RADCOMM SPECTRUM SHARING
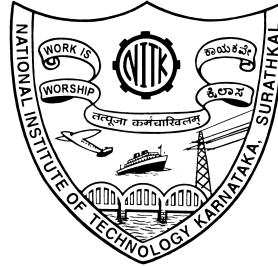
Thesis

Submitted in partial fulfillment of the requirements for the degree of

DOCTOR OF PHILOSOPHY

by

GUNNERY SRINATH

DEPARTMENT OF ELECTRONICS AND COMMUNICATION ENGINEERING,

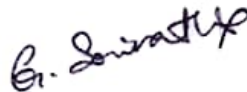NATIONAL INSTITUTE OF TECHNOLOGY KARNATAKA,

SURATHKAL, MANGALORE - 575025

March 2023.

Dedicated to family and friends

DECLARATION

by the Ph.D. Research Scholar

I hereby declare that the Research Thesis entitled **DETECTION AND TRACK-ING OF RADAR TARGETS WITH IN-BAND COMMUNICATION IN-TERFERENCE FOR RADCOMM SPECTRUM SHARING** which is being submitted to the **National Institute of Technology Karnataka, Surathkal** in partial fulfillment of the requirements for the award of the Degree of **Doctor of Philosophy** in **Electronics and Communication Engineering** is a *bonafide report of the research work carried out by me.* The material contained in this Research Thesis has not been submitted to any University or Institution for the award of any degree.

Gunnery Srinath (177067 / 177EC005)

Department of Electronics and Communication Engineering

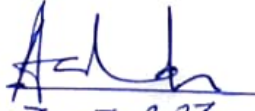Place: NITK, Surathkal.

Date: 27-Mar-2023.

CERTIFICATE

This is to *certify* that the Research Thesis entitled **DETECTION AND TRACKING OF RADAR TARGETS WITH IN-BAND COMMUNICATION INTERFERENCE FOR RADCOMM SPECTRUM SHARING** submitted by **GUNNERY SRINATH**, (Regn. No: 177067) as the record of the research work carried out by him, is *accepted as the Research Thesis submission* in partial fulfillment of the requirements for the award of the degree of **Doctor of Philosophy**.

Dr. Prashantha Kumar H

Research Guide

Dr. Pathipati Srihari

Research Guide

30-3-2023

Prof. Ashvini Chaturvedi

Chairman - DRPC

Acknowledgement

I gratefully acknowledge and thank the many people who have contributed directly and indirectly to this dissertation. To begin with, I express my heartfelt gratitude to Dr. Prashantha Kumar H, Assistant Professor, Department of Electronics and Communication Engineering (ECE), and Dr. Pathipati Srihari, Assistant Professor, Department of ECE of National Institute of Technology Karnataka (NITK), Surathkal, for allowing me to pursue a Ph.D., for their invaluable guidance and encouragement as doctoral advisors.

I also thank my Research Progress Assessment Committee (RPAC), consisting of Dr. Dattatraya N Gaonkar, Associate Professor, Department of Electrical and Electronic Engineering (EEE), and Dr. Aparna P, Assistant Professor, Department of ECE of NITK Surathkal, for the valuable time they have spent on my supervisory meetings, providing valuable comments and feedback on my research work.

I convey my special thanks to Doctoral Thesis Assessment Committee (DTAC) Members, consist of

- Dr. Shobha Sundar Ram, Associate Professor, Department of ECE, Indraprastha Institute of Information Technology (IIIT) New Delhi.

- Dr. Rajshekhar V Bhat, Assistant Professor, Department of Electrical Engineering, Indian Institute of Technology (IIT) Dharwad.

- Dr. Ashvini Chaturvedi, Professor and Head, Department of ECE, NITK Surathkal.

- Dr. U. Shripathi Acharya, Professor and former Head, Department of ECE, NITK Surathkal.

- Dr. Geetha V, Assistant Professor, Department of IT, NITK Surathkal.

sharing scenario and assisting in the development of a new measurement model.

Special thanks to my friends, relatives and villagers of Mahankali Devi Puttur, Tirupati, AP, who have constantly been encouraging, motivating and cheering me in all situations.

This acknowledgement would not be complete without mentioning my family's painstaking efforts and patience. No words are adequate to express my indebtedness to my parents (amma) Smt. G Arundathi Reddy, (nanna) Sri. G Umakantha Reddy, brother (anna) Mr. G Dinesh Reddy, sister-in-law (Vadina) Mrs. G Hema Reddy, aunt (pinni) Smt. G Gayathri Reddy, uncle (babai) Sri. G Venkata Ramana Reddy, and cousins (thammullu) Mr. G SivaRama Krishna Reddy, Mr. G SreeHarsha Reddy for their consistent support, love and good wishes. This achievement of my life would not have been possible without the support and cooperation of my family. Thank you for encouraging me in all of my pursuits and inspiring me to follow my dreams.

Lastly, I express my hearty thanks to those I might have missed mentioning who helped directly or indirectly and cooperated with me in completing this research work.

Abstract

The problem of spectral congestion considers radar and communication system (Rad-Comm) spectrum sharing as an inevitable solution. As these systems share the spectrum, they cause interference to one another. Many researchers started suggesting various solutions to address the in-band interference. Towards this step, addressing the problem from the radar perspective, this thesis makes two primary contributions. The first one is detecting the target-reflected radar signals in the presence of interference from an in-band cyclostationary digital modulated wireless communication signal. The Neyman-Pearson (NP) based optimum detection rules have been derived for the equalization of the interference from in-band communication systems. Sub-optimum detection structures are also derived with the assumption that the in-band interference is a white stationary time-invariant Gaussian process. Further, considering the equalization, modified CFAR receiver structures are also presented. By considering the mathematical models for cyclostationary or periodic in-band interference, the performances of the optimum, sub-optimum and modified CFAR detectors are quantified analytically in terms of detection and false alarm probabilities. The resulting receiver operating characteristic (ROC) curves are analysed as a function of the signal-to-interference ratio (SIR).

Another important contribution considered in this research investigation is target tracking performance of a radar system in the presence of in-band wireless communication transmitters (IWCTs). The distributed radars present in the surveillance region surrounded by multiple in-band wireless communication transmitters (IWCTs) scenario is considered. A new measurement model is proposed by considering both radar returns and returns due to IWCTs. The tracking performance is evaluated using the global nearest neighbour (GNN) tracker with an extended Kalman filter (EKF) for the received measurement set. The track-to-track association (T2TA) is performed to identify the true target track on multiple tracks produced owing to the presence of IWCTs. The track-to-track fusion (T2TF) is carried out to improve the true target estimates. The position root mean square error (PRMSE) is used to quantify the target estimation accuracy. The posterior Cramer–Rao lower bounds (PCRLBs)

quantifying the achievable estimation accuracies are also presented. The simulation results reveal that the T2TA of tracks from multiple radars identify the true target track, and T2TF improves the PRMSE.

As an additional third contribution, the spectrum sharing radar (SSR) is considered that uses the total available bandwidth (BW) for both radar-based sensing and communication. Unlike traditional radar, the SSR divides the total available BW into radar-only and mixed-use bands. Taking such BW sharing into account, this research investigates the performance of SSR in an information-theoretic sense. To evaluate performance, mutual information (MI), spectral efficiency (SE), and capacity (C) metrics are used. Initially, a clean environment (no multipath) is considered in order to evaluate performance metrics in the mixed-use band with and without successive interference cancellation (SIC). The MI and SE are calculated in the mixed-use band with and without successive interference cancellation (SIC). Also, the performance metrics are extended to account for the multipath environment. In addition, the MI, SE, and C of traditional radar and communication systems are taken into account to compare the performance of SSR.

Furthermore, this research presents target estimation performance improvement in the cooperative RadComm spectrum sharing system model. Due to cooperation, target returns results from the communication transmitter are also exploited to improve the target estimation performance. The Cramer-Rao lower bound (CRLB) is considered as a metric to evaluate the target estimation performance. The cooperative system model is compared with the non-cooperative RadComm spectrum sharing operation and stand-alone radar system operation. Simulation results reveals that the cooperative RadComm spectrum sharing system model provides improved performance compared to non-cooperative and stand-alone operations.

Contents

List of Figures

ix

List of Tables

Abbreviations and Nomenclature

Abbreviations

S-D	S-Dimensional
BER	bit error rate
BS	base station
BW	bandwidth
CA	cell-averaging
CDR	communication data rate
CFAR	Constant-False-Alarm Rate
CI	covariance intersect
CIB	communication isolated sub-band
CKF	cubature Kalman filter
CPM	continuous phase modulation
CR	cognitive radio
CRLB	Cramer-Rao Lower Bound
CS	censored
CUT	cell under test
CV	constant velocity
DFRC	dual-functional radar-communication
EI	ellipsoidal intersect
EKF	extended Kalman filter
FC	fusion center
FIM	Fisher information matrix
FMCW	frequency-modulated continuous-wave
FOD	first-order difference
GNN	global nearest neighbor
HCN	heterogeneous cellular networks
IF	intermediate frequency

IMF	information matrix fusion
IMM	Interactive multiple models
IRF	information reduction factor
ISB	isolated sub-band
ISI	intersymbol interference
IWCT	in-band wireless communication transmitter
KF	Kalman filter
LFM	linear frequency modulation
MDCBF	multi-domain collaborative-based filter
MHT	multiple hypothesis tracker
MI	mutual information
MIMO	multi-input multi-output
ML	maximum likelihood
MS	mobile station
NN	nearest neighbor
NP	Neyman-Pearson
OFDM	orthogonal frequency division multiplexing
OS	order statistic
PCRLB	Posterior Cramer-Rao lower bound
PDA	probabilistic data association
PKF	particle Kalman filter
PRMSE	position root mean square error
RadComm	radar and communication system
RCC	radar-communication coexistence
RCS	radar cross-section
RF	radio frequency
RIB	radar isolated sub-band
RMI	radar mutual information
ROC	receiver operating characteristic
SAR	synthetic aperture radar
SCI	sampling covariance intersect
SE	spectral efficiency
SIC	successive interference cancellation
SINR	signal-to-interference-plus-noise ratio

SIR	signal-to-interference ratio
SISO	single-input single-output
SPR	subcarrier power ratio
SRCRLB	square root CRLB
SSR	spectrum sharing radar
T2TA	track-to-track association
T2TF	track-to-tack fusion
TM	trimmed mean
TV-FRESH	time-varying frequency shift
UKF	unscented Kalman filter

Nomenclature

$\mathbb{E}$	expectation operator
$\mathbf{F}$	state transition matrix
$\mathbf{H}$	measurement transition matrix
$\mathbf{K}$	Kalman gain
$\mathbf{P}$	state covariance matrix
$\mathbf{Q}$	process noise covariance matrix
$\mathbf{R}$	measurement noise covariance matrix
$\mathcal{H}$	hypothesis
$\mathcal{N}$	Gaussian density
Tr	trace operator
Var	variance operator
k	discrete time index
p	probability
P_D	probability of detection
P_{FA}	probability of false alarm
t_s	sampling time
$'$	transposition operator

Chapter 1

Introduction

1.1   Radar and communication system (RadComm) spectrum sharing

Due to rapid advances in information and communication technologies during the last decade, the available spectrum has become congested, and there are demands for higher radio frequency (RF) spectrum for upcoming 5G, 6G and other communications. Further, the increase in the usage of various wireless technologies yielded spectrum scarcity (Forecast *et al.*, 2019). Due to this, wireless users' accommodation and providing good quality of service as per their requirements are becoming extremely difficult. The significant portion of RF spectrum reserved for radar systems dedicated to sensing applications. There is a need to explore a way to utilize/ share the existing radar bands for communication system purposes. This necessity has created huge interest among radar engineers to explore this further. Sharing the underutilized, permanently allocated, and a large amount of available radar bandwidth with the communication systems serves the wireless user demands and improves the effective utilization of the spectrum (Blunt and Perrins, 2018).

A radar system transmits a known signal and detects target reflected signals in a wireless environment (Richards *et al.*, 2010). In contrast, the main aim of a communication system is the transfer of information from one node to another via a wireless channel with known or estimated characteristics (Lathi and Ding, 2018). As these two functionalities conflict with each other, these systems are designed in isolation by imposing constraints from regulatory authorities in respective countries (Paul *et al.*, 2017). This isolated approach does not inherently afford to exploit the mutual benefits

of separate radar and communication systems or mitigate the interference between them.

The spectrum sharing between radar and communication system (RadComm) is becoming inevitable because of increased wireless usage (Forecast *et al.*, 2019; Blunt and Perrins, 2018; Paul *et al.*, 2017; Zhang *et al.*, 2021*a*). The RadComm spectrum sharing research is broadly categorized into two sub-topics: radar-communication coexistence (RCC) and dual-functional radar-communication (DFRC) system design (Blunt and Perrins, 2018). In RCC, the radar and communication systems work independently in a cooperative/ non-cooperative manner within the same frequency band. As these systems operate in the same frequency band, they cause interference to each other. On the other hand, in DRFC systems, a single system possesses both radar and communication system functionalities. Since radar and communication are accommodated within the same system, interference occurs. The first category of research aims to develop efficient interference management techniques so that the two systems can operate without undue interference. Alternatively, DFRC techniques focus on designing joint systems that simultaneously perform wireless communication and remote sensing. This benefits both sensing and signalling operations via real-time cooperation, de-congests the RF environment and allows a single hardware platform for both functionalities.

Thus, owing to the spectrum scarcity, the radar and communication system sharing a joint spectrum or operating in the same band finds increasing impetus and poses exciting challenges to radio frequency (RF) engineers.

1.2   Literature review

Multiple techniques have been proposed in the literature to address the problems resulting from the spectrum sharing of radar and communication systems and make it a reality. These approaches address the problem from the communication system point of view (Nartasilpa *et al.*, 2018; Zheng *et al.*, 2018; Carrick *et al.*, 2019), from the radar system point of view (Zilz and Bell, 2018; Shajaiah *et al.*, 2015; Zilz and Bell, 2019), and by considering the joint dual function radar and communication system (Liu *et al.*, 2018; Khawar *et al.*, 2018; Qian *et al.*, 2018). Some other architecture-oriented

algorithms address the same problem from the transmitter side (null projection, optimal waveform design and time division scheduling (Kuan-Wen Huang *et al.*, 2015; Shi *et al.*, 2018; Cheng *et al.*, 2018)), from the receiver side (spatial, temporal and spectral based processing (Paisana *et al.*, 2018, 2017; Herschfelt and Bliss, 2018)), and by developing a joint system (dual-function system, joint waveform and joint detection (Ahmed *et al.*, 2018; Hassanien *et al.*, 2016)).

Nevertheless, in literature, the RadComm spectrum sharing research seems to exist in two different directions (Munir *et al.*, 2022). The first category of research addresses the problems arising from the independent operation of radars and communication devices in the same spectrum in a cooperative/ non-cooperative manner (Zheng *et al.*, 2019). The second direction contributes to developing a joint system with radar and communication functionalities (Hassanien *et al.*, 2019; Ma *et al.*, 2020). This section outlines these two research directions to place this dissertation in the context of existing work. Also, this section reviews the literature on radar target detection and tracking algorithms to maintain relevance to the work carried out.

1.2.1 Radar-communication coexistence (RCC)

The effect of an unmitigated radar system interference on a communication system receiver is evaluated in (Nartasilpa *et al.*, 2018) in terms of bit error rate (BER). Apart from that, to minimize the BER, complex constellation designs are also proposed in (Nartasilpa *et al.*, 2018). A spatial processing technique that mitigates the in-band main lobe wireless interference is proposed in (Geng *et al.*, 2015). This beamforming technique uses the principle of orthogonality in a coherent multi-input multi-output (MIMO) radar. Taking advantage of an array of antennas at the receiver end and signal processing from a combined temporal, spectral and spatial perspective, a multi-domain collaborative-based filter (MDCBF) is proposed in (Mao *et al.*, 2016). Exploiting the concept of cognitive radio (CR) and taking advantage of a MIMO radar structure, the theoretical feasibility of interference mitigation between spectrum-sharing radar and communication systems is shown in (Deng and Himed, 2013). The effect of interference in RCC, from a communication system perspective, is presented in (Nartasilpa *et al.*, 2016). Besides, in (Bică and Koivunen, 2019) it is assumed that the radar and communication system are located apart; the target time

delay parameter is estimated by designing the optimal waveform for the radar system, with a constraint on Cramér–Rao lower bound (CRLB). Also, it is demonstrated that using additional constraints like transmitted power and subcarrier power ratio (SPR) while designing the optimized radar waveform reduces delay ambiguities. In (Carrick et al., 2019), using the concept of cyclostationarity, a time-varying frequency shift (TV-FRESH) filter is proposed to decode orthogonal frequency division multiplexing (OFDM) signals in the presence of additive linear frequency modulated (LFM) pulsed radar interference. Moreover, the efficacy of the proposed filter was shown in the form of BER curves.

Furthermore, the statistical model for in-band wireless communication interference and its effect on the adaptive threshold-based detector at the radar receiver is analysed in (Zilz and Bell, 2018). The results in (Zilz and Bell, 2018) show that interference follows non-Gaussian statistics, and the detection of targets using a cell averaging detector provides inadequate performance in identifying the target and demands for alternative and efficient detection schemes. A novel whitening filter followed by matched filter detector is proposed to detect the radar targets in the presence of in-band communication interference (Zilz and Bell, 2019). In (Martone and Amin, 2021), considering the RadComm spectrum sharing in a cooperative and non-cooperative manner, a thorough literature survey and future research directions are presented.

1.2.2 Dual-functional radar-communication (DFRC)

A comprehensive survey of RadComm spectrum sharing is provided in (Paul *et al.*, 2017; Zhang *et al.*, 2021*a*), and (Zhang *et al.*, 2021*b*). The (Hassanien *et al.*, 2016) and (Sahin *et al.*, 2017) discuss using a single radar waveform that can embed the communication symbols for communication purposes and vice-versa. Especially in (Sahin *et al.*, 2017), a novel continuous phase modulation (CPM) based information-bearing waveform is proposed, without degrading the spectral characteristics, for improving radar target detection and maintaining high power with constant envelope constraint for long-range target visibility. In another communication, the single-input single-output (SISO) and multi-input multi-output (MIMO)-based architectures for the joint RadComm have been investigated (Qian *et al.*, 2018). The system design

4

in (Qian *et al.*, 2018) is based on the maximization of signal-to-interference-plus-noise ratio (SINR) at the radar receiver. Further, in (Qian *et al.*, 2018), by maintaining the achieved SINR at the radar receiver, the maximization of communication rate constraint is additionally imposed for communication purposes. Authors in (Bliss, 2014) have derived the novel estimation and information rate bounds for a DFRC system, and its performance is evaluated using the derived bounds. Besides, the extension of joint performance bounds with clutter is presented in (Chiriyath and Bliss, 2015). In addition, the same performance bounds have been extended for the case of frequency-modulated continuous-wave (FMCW) radar (Paul and Bliss, 2015).

Further, in (Tian *et al.*, 2019*b*), a joint RadComm is considered, where overall bandwidth is shared among the radar and communication system in an independent coexistence, and a partial band coexistence manner is presented. In an independent coexistence, the overall BW of is split into two subbands one for radar only operation and other for communication system operation. Whereas in partial band coexistence, the joint RadComm system can operate radar and communication functions in the same band. Moreover, in (Tian *et al.*, 2019*b*), the performance is analysed in terms of mutual information (MI) and communication data rate. In (Tian *et al.*, 2019*a*), the performance is evaluated in the form of a localization estimation rate and communication data rate by considering the three different cases (isolated sub-band (ISB), communication isolated sub-band (CIB), and radar isolated sub-band (RIB) situation). Here, the localization estimation rate is analogous to the data information rate of the communication system. In (Sneh *et al.*, 2022), a software prototype implementation of IEEE 802.11ad based joint RadComm transceiver has been provided and its performance is analysed. Using tools from stochastic geometry (SG), in (Ram *et al.*, 2022) the network optimization of joint RadComm system is performed to increase the system's throughput.

The DFRC system design for automotive applications has been studied in (Zhang *et al.*, 2021*c*; Tang *et al.*, 2021). The joint transmit waveform design and receiver design for the DFRC system are studied in (Tsinos *et al.*, 2021). In contrast to other works, in (Tsinos *et al.*, 2021), the radar performance is optimized without knowing a predetermined radar beam pattern. In (Tian *et al.*, 2019), the performance of the DFRC systems is analysed in terms of radar mutual information (RMI) and

communication data rate (CDR) for radar and communication systems. The analysis assumes that the DFRC system transmits/receives the radar and communication signals on the isolated bands (isolation-based scheme) and the same band (sharing-based scheme). Further, in (Tian *et al.*, 2019) for an isolated-based scheme, the RMI/CDR maximization of the DFRC system is solved independently with the constraint on optimal power allocation solutions. At the same time, the joint maximization of RMI/CDR for the DFRC system is solved for a sharing-based scheme (Tian *et al.*, 2019). An ultra-wideband chaotic radar with wireless synchronization command is proposed in (Wang *et al.*, 2020) for target localization and tracking.

1.2.3 Target Detection and Tracking

The detection and location of an object/ target by means of a return signal is the major purpose of a radar system. The Constant-False-Alarm Rate (CFAR) detector is an important detection criteria in radar applications. CFAR sets an adaptive threshold (in contrast to fixed threshold Neyman-Pearson (NP) detector) to identify a radar target buried in unwanted interference (Richards, 2014). The CFAR threshold is estimated from the data in the neighbouring cells by maintaining the desired false alarm probability. Different CFAR detectors are present in the literature cell-averaging (CA), Smallest-of CA-CFAR, Greatest-of CA-CFAR, trimmed mean (TM) or censored (CS) CFAR, order statistic (OS) CFAR (Richards, 2014; Richards *et al.*, 2010; Levanon, 1988). The detection performance of the CA-CFAR detector is presented in (Hansen and Ward, 1972). The performance of the linear-law-based CA-CFAR is evaluated in (Raghavan, 1992), and it is compared with the square-law-based detector. In (Rohling, 1983), the CFAR threshold schemes to identify the multiple targets in clutter background is presented. To identify the targets in non-homogeneous clutter environments, an intelligent, dynamic threshold calculation based variability index CFAR is developed (Smith and Varshney, 2000). To improve the safety of low-flying objects equipped with millimeter-wave radar, a first-order difference (FOD)-CFAR method is proposed in (Jiang *et al.*, 2016).

Target tracking is an essential requirement, where one or more sensors are employed to estimate the time-varying kinematics of targets within the given surveillance region. The measurements are from diverse sources such as the targets of interest,

clutter, etc. The main objective of target tracking is to partition the received measurements and form tracks for the targets of interest by estimating parameters like position, velocity, acceleration, turn, intensity, etc. Target tracking typically contains filtering, data association, and track management. The Kalman filter (KF) provides an optimal estimate under the considerations of linearity and Gaussian distribution (Bar-Shalom *et al.*, 2004). Whereas, converted Kalman filter, extended Kalman filter (EKF), cubature Kalman filter (CKF), unscented Kalman filter (UKF), and particle Kalman filter (PKF) (Bar-Shalom *et al.*, 2004), Interactive multiple models (IMM), etc.. (Bar-Shalom *et al.*, 2011) are widely used to address the non-linearity. When it comes to the data association, nearest neighbour (NN) and global nearest neighbour (GNN) are traditional association methods, which use a single measurement out of all available measurements falling within the validation gate (Sinha *et al.*, 2012). In contrast, the probabilistic data association (PDA) method applies the weighted sum of all the measurements within the validation gate (Bar-Shalom *et al.*, 2009). The optimal approach for target tracking was demonstrated using a multiple hypothesis tracker (MHT) under the assumption of propagating all the hypotheses into tracks (Blackman, 2004). Logic-based track maintenance and quality-based track maintenance are popularly used for track management (Jiang *et al.*, 2014).

The target tracking can be performed by using single/multiple sensors either in centralized or distributed configurations (Bar-Shalom *et al.*, 2011). In distributed target tracking, track-to-track association (T2TA) is an important block to distinguish and assign the tuples corresponding to the targets (Bar-Shalom, 1981). The tuples of tracks reported by the T2TA module are fused to attain the global estimates. Generally, track-to-track fusion (T2TF) is classified into correlation free and correlation-based fusion approaches (Smith and Singh, 2006). The correlation-based fusion technique requires the exact cross covariances among the local tracks of the same target. Hence, a large amount of information exchange is required between the fusion centre (FC) and the local trackers, making this method realizable for practical scenarios (Bakr and Lee, 2017). Theoretically, information matrix fusion (IMF) or centralized tracking provides an optimal estimate/fused track (Bar-Shalom *et al.*, 2011). The correlation-free fusion-based algorithms work independently of cross covariances, which allow the fusion to be performed at any local tracker without the

participation of the fusion centre. The ellipsoidal intersect (EI) (Sijs *et al.*, 2010), co-variance intersect (CI) (Chen *et al.*, 2002), sampling covariance intersect (SCI) (Tian *et al.*, 2010) etc., comes under the correlation free fusion methods. Besides, these three methods provide the fused estimate by approximating the intersection region of individual ellipsoids. Among them, the EI, CI works better for two sensor-based fusion. On the other hand, the SCI has more flexibility to fuse the data from more sensors.

1.3   Motivation and research objectives

Most of the literature in RadComm spectrum sharing primarily focuses on detection, waveform design perspective, and deriving the theoretical bounds. The target tracking-based contributions in RadComm spectrum sharing are rarely reported. To realize efficient spectrum sharing RadComm systems, there is a need to further explore and develop alternative and effective detection and tracking algorithms. In this connection, there is a necessity to provide improved detection schemes to address the problem of in-band communication interference in RadComm spectrum sharing. In addition, there is a strong requirement to design and evaluate the performance of target tracking algorithms in the presence of in-band wireless communication transmitters (IWCTs). Furthermore, the dual functional RadComm systems, capable of utilizing the same BW for both radar and communication purposes are becoming popular, there is a need to analyse the performance of such systems. With this motivation, the proposed research intends to develop alternative and efficient detection and tracking algorithms suitable for the RadComm spectrum sharing scenario. Based on this, the objectives of the proposed research are as follows:

- Detection of radar targets in the presence of in-band wireless communication system interference.

- Tracking of radar targets with in-band wireless communication system interference.

- Performance analysis/ improvements in radar and communication system spectrum sharing scenario.

1.4 Proposed approaches for each identified research objective

1.4.1 Detection of radar targets in the presence of in-band wireless communication interference

This research work addresses the problem of in-band interference in RadComm spectrum sharing at the detection level from a temporal radar signal processing perspective. This work considers the problem of detection of target reflected radar signal by exploiting the cyclostationary features of in-band wireless communication interference. Instead of detecting the cyclostationary signals in additive noise (Gardner *et al.*, 2006; Karami *et al.*, 2015), this work addresses the problem of detecting target-reflected radar signals in the presence of cyclostationary wireless communication interference. First, with three different assumptions that the target-reflected radar signal is a) deterministic, b) with a random phase, and c) random, the Neyman-Pearson (NP) based optimum, missynchronized, and sub-optimum detection rules are derived, and their structures are presented. The optimum detector is the one where proper equalization is made to compensate for the interference component by passing through the equalizer/whitening filter and further processed for detection. If the equalization to the interference component is improper/ missynchronized, it is treated as missynchroized detection. Next, instead of equalizing/ compensating the interference, if it is treated as white Gaussian and further proceeded for detection, then it is called the sub-optimal detection. Second, in each case, the performance metrics such as detection and false alarm probabilities are derived. Third, in each case, a thorough performance analysis is conducted for the new detection structures. Fourth, for the detection of random signals with in-band interference, a modified CFAR detector is proposed, and it has been compared with the NP based detector. The development follows a similar signal processing/detection structure as presented in (Zilz and Bell, 2019), where the main focus is to derive an equalizer/whitening filter with the deterministic target return signal assumption. In contrast, the focus is not on deriving an equalizer/whitening filter. In this work, given the equalizer/whitening filter parameters, the detection structures are developed, and their performance analysis is conducted.

1.4.2 Tracking of radar targets with in-band wireless communication interference in RadComm spectrum sharing

A RadComm spectrum sharing scenario is considered, where multiple mono-static radars are present over a surveillance region to detect the radar targets and are surrounded by multiple in-band wireless communication transmitters (IWCTs). Even though a single target is present in the scenario, the radar receives multiple measurements owing to IWCTs. Hence, there is a need to distinguish true target measurements from all the evolved measurements. Regarding, this research work considers the effect of in-band wireless communication interference on target tracking in RadComm spectrum sharing. A new measurement model is proposed for multiple radars surrounded by the multiple IWCTs scenario. This new measurement model considers all the measurements evolved due to radar, IWCTs, and false alarms. This research work proposes to use distributed radars with a local tracker by considering all the available measurements and performing target tracking using the extended Kalman filter (EKF) and global nearest neighbour (GNN) association. The work suggests considering all the local tracks evolved from all sensors and performing an S-D assignment-based track-to-track association (T2TA) to identify the true target tracks rather than falsified tracks evolved due to the presence of IWCTs. Once the actual tracks are separated from all the grown tracks using T2TA, the track-to-track fusion (T2TF) is performed to achieve the global tracks. Here, the correlation-free fusion algorithms (ellipsoidal intersect (EI), covariance intersect (CI), and sampling covariance intersect (SCI)) are used for fusion. The target estimation accuracy is quantified using position root mean square error (PRMSE) and compared with its achievable theoretical lower bounds (PCRLBs).

1.4.3 Performance analysis/ improvements in RadComm spectrum sharing scenario

This work considers spectrum sharing radar (SSR), assuming that the total BW is split for radar-only and mixed-use purposes. The SSR performance is analysed using MI and SE metrics from the radar perspective in an information-theoretic sense and capacity (C) metric is considered from communication perspective. First, the MI of SSR is evaluated for the allocated radar-only BW. Next, the MI of SSR in

a mixed-use band is evaluated in two cases, with SIC and without SIC. Hence, the total MI is calculated as a summation of MI in radar-only and mixed-use bands. In addition to MI, the SE metric is introduced to evaluate the spectral utilization of the SSR. In contrast to MI and SE, the communication C is calculated for the mixed-use band (since it is the only band, which carries communication system information). To comprehensively look into the problem, the multipath environment between the target-to-receiver of SSR is also incorporated and evaluated the SSR performance pertaining to MI, SE, and C. Finally, the performance of the SSR is compared with the traditional radar and communication system. Further, the cooperative RadComm spectrum sharing system model is considered. With the cooperation, the complete statistics of the communication signal are shared with the radar. It helps radar in using the target reflected signals due to the communication transmitter, which in turn improves the target estimation performance. This research work presents the target estimation performance in terms of Cramer-Rao Lower Bound (CRLB) as a performance metric. To show the efficacy of the cooperative nature, the target estimation performance is also calculated for the non-cooperative nature of the RadComm spectrum sharing case and stand-alone radar system operation case.

All the results in this research work are obtained using MATLAB R2020b on a computer with 16 GB RAM Intel(R) Xeon(R) @ 3.50GHz.

1.5   Contribution of the thesis

In this thesis, some of the important problems associated with radar and communication system (RadComm) spectrum sharing are addressed from a radar perspective at the detection and tracking level. The key contributions of the thesis are as follows:

- Detection of radar targets with in-band communication interference

  - A new Neyman-Pearson (NP) based optimum, missynchronized, sub-optimum, and modified CFAR detection structures are proposed to detect radar targets in the presence of in-band communication interference.

  - The detection and false alarm probabilities are derived considering the target-reflected radar signal as deterministic, signal with a random phase, and completely random signal cases.

– The performance of the proposed detectors is analysed in terms of receiver operating characteristic (ROC) curves.

- Tracking of radar targets with in-band communication interference

  – A new measurement model is proposed for multiple radars surrounded by the multiple IWCTs scenario and performed distributed tracking.

  – An S-D assignment-based track-to-track association (T2TA) is formulated to identify the actual target tracks.

  – The track-to-track fusion (T2TF) is performed using the correlation free fusion algorithms ellipsoidal intersect (EI), covariance intersect (CI), and sampling covariance intersect (SCI) to improve the target estimation accuracy.

- Performance analysis/ improvements in RadComm spectrum sharing

  – The spectrum sharing radar (SSR) is considered assuming the available bandwidth is split for radar-only use and mixed-use of both radar and communication purposes. Also assumed that there exists a multipath between the target-to-radar receiver channel.

  – The performance of the SSR is analysed using MI and SE metrics from the radar perspective, the capacity (C) metric from the communication perspective.

  – The overall MI of SSR is calculated as a summation of MI in radar-only band plus MI in mixed usage band. The mixed usage band MI is further evaluated using with/without SIC. The metric is compared against the traditional radar.

  – Similar to MI, the overall SE of the SSR is also calculated and compared with traditional radar.

  – The capacity metric of SSR is also calculated in mixed-use band and compared with traditional communication system.

  – The target estimation performance improvement is shown by considering the new cooperative RadComm spectrum sharing system model in terms

of CRLB as a performance metric.

1.6   Overview

The rest of the thesis is organised as follows. Chapter 2 presents the detection of radar targets in the presence of in-band wireless communication interference. Chapter 3 deals with the target tracking part. Even though a single target is present in the surveillance, the problem of receiving multiple tracks at the radar receiver owing to in-band wireless communication transmitters (IWCTs) is addressed. Chapter 4 presents the performance analysis of spectrum sharing radar (SSR). Here, the SSR shares the bandwidth (BW) among the radar-only and mixed-use of both radar and communication purposes is considered, and the performance is analysed in an information-theoretic perspective. While Chapter 5 discusses the target estimation performance improvement in cooperative RadComm spectrum sharing. Finally, the concluding remarks and future research directions are presented in Chapter 6.

Further, in this thesis, all the scalar variables are represented with regular font, vectors with bold font small characters and matrices with bold font upper case characters.

Chapter 2

Detection of Radar Targets in the Presence of In-band Wireless Communication System Interference

This chapter presents the detection of target-reflected radar signals in the presence of in-band wireless communication system interference. Considering the three different cases of target-reflected radar signals, namely, deterministic signals, signals with random phase, and completely random signals, the optimum detection rules are derived, and the corresponding receiver structures for the equalization of the interfering signal are presented. Further, considering the equalization, modified CFAR receiver structures are also presented. The results are quantified using detection, false alarm probabilities, and corresponding receiver operating characteristic (ROC) curves.

2.1   Motivation and system model

In this section, the motivation for this study and the system model assumed therein are presented. Figure 2.1 illustrates the in-band operation of a radar and communication system with RadComm spectrum sharing. In Figure 2.1, where the radar is trying to detect the targets of interest (radar system functionality), a mobile station (MS) and a base station (BS) are communicating with each other (communication system functionality) in in-band. As these systems operate in the same band, they cause interference to one another, which provides the motivation for this study. As the primary interest of this research is from a radar perspective, Figure 2.2 shows the radar receiver structure for the RadComm spectrum sharing system model.

The received signal at the radar receiver, shown in Figure 2.2, consists of the sig-
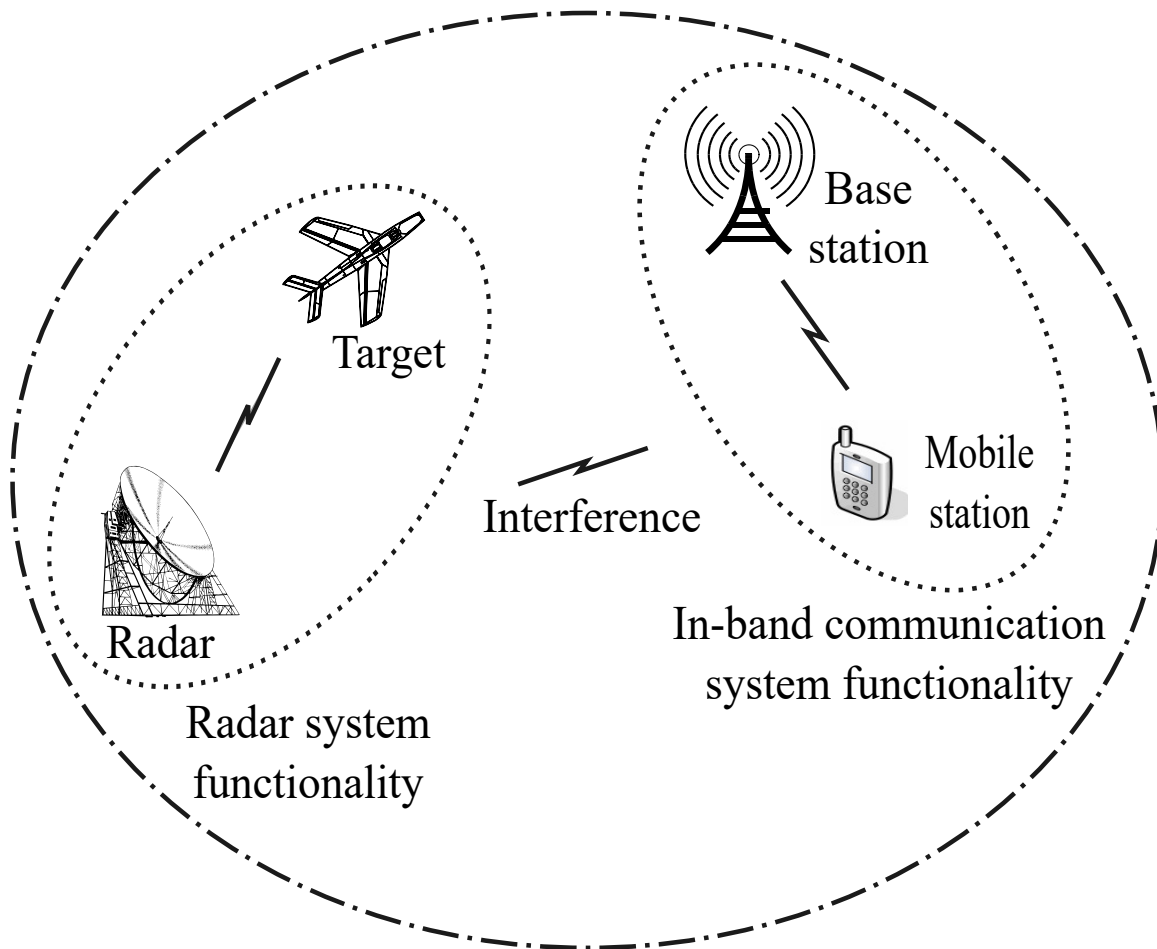
Figure 2.1: System model (in-band operation of radar and communication systems).
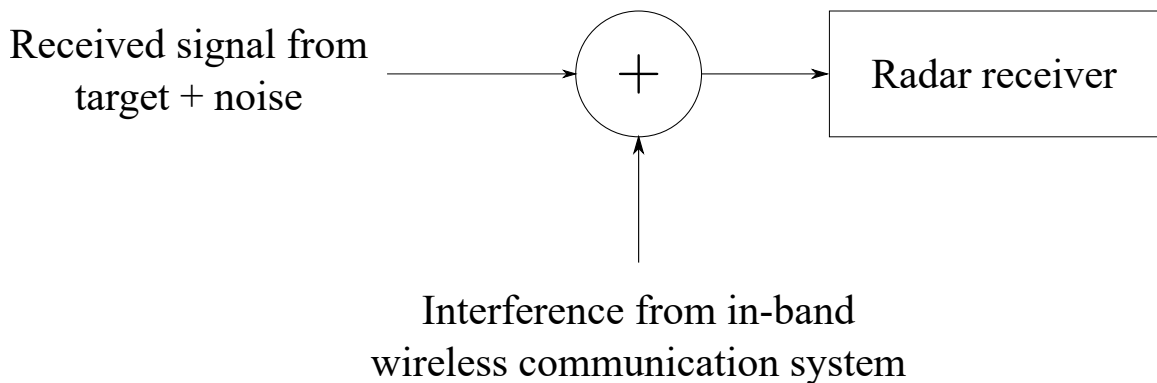
Figure 2.2: Radar receiver structure for a spectrum-sharing radar.

nal of interest, in-band interference and noise. The problem of detecting the radar signal, corrupted by in-band cyclostationary digital modulated wireless communication and noise, can be modelled as a conventional hypothesis testing problem. Under hypothesis $\mathcal{H}_1$, the received signal (denoted by $r(t)$) consists of the signal of interest (denoted by $s(t)$), with additive in-band cyclostationary digital modulated

wireless communication interference (denoted by $s_I(t)$), and noise (denoted by $w(t)$). Whereas, under hypothesis $\mathcal{H}_0$, the received signal consists of only the interference plus noise. The mathematical equivalent of this conventional hypothesis testing problem is given by

$$r(t) = \begin{cases} s(t) + s_I(t) + w(t), & \text{under } \mathcal{H}_1, \\ s_I(t) + w(t), & \text{under } \mathcal{H}_0, \end{cases} \quad t \in T \qquad (2.1)$$

where T is the period of observation of $r(t)$.

The in-band wireless communications interference $s_I(t)$ can be interpreted as the sum of N independent communication sources, with each source emitting M data symbols. This allows us to write $s_I(t)$ as (Proakis and Salehi, 2007; Zilz and Bell, 2018)

$$s_I(t) = \sum_N \sum_M s_{I_n}(mT_m)g(t_n - mT_m) \qquad (2.2)$$

where T_m is the pulse duration of the mth symbol and $g(.)$ is the shaping waveform, which can be a rectangular pulse or intersymbol interference (ISI) tolerable raised cosine pulse (Proakis and Salehi, 2007).

As the intensity of $s_I(t)$ is much higher than the noise level (Zilz and Bell, 2018), in general, the conventional hypothesis testing problem given in (2.1) can be reduced to

$$r(t) = \begin{cases} s(t) + s_I(t), & \text{under } \mathcal{H}_1, \\ s_I(t), & \text{under } \mathcal{H}_0, \end{cases} \quad t \in T \qquad (2.3)$$

By multiplying the received signal $r(t)$ with a known time-varying factor $\frac{\langle s_{I_0} \rangle}{s_{I_0}(t)}$, the cyclostationary time-varying intensity $s_I(t)$ is converted into the optimum detection of a white stationary process $\tilde{s}_I(t)$ with time-invariant intensity $\langle s_{I_0} \rangle = \int_T s_{I_0}(t)dt$. Here, $s_{I_{\tilde{T}}}(t) = s_I(t + \tilde{T})$, $\tilde{T} = T, 2T, \ldots$, T is the period and $s_{I_0}(t)$ represents for the initial period. The time-varying factor can be found by training (e.g., switch-off the radar transmitter and sense/listen to the in-band wireless communication interference) the radar receiver for some period of time (Zilz and Bell, 2019). The process of multiplying $r(t)$ with a known time-varying factor $\frac{\langle s_{I_0} \rangle}{s_{I_0}(t)}$ can be interpreted as an output of an equalizer/whitening filter. The equivalent hypothesis testing problem is

$$\tilde{r}(t) = \begin{cases} \tilde{s}(t) + \tilde{s}_I(t), & \text{under } \mathcal{H}_1, \\ \tilde{s}_I(t), & \text{under } \mathcal{H}_0, \end{cases} \quad t \in T \qquad (2.4)$$

where $\tilde{r}(t)$ is defined as

$$\tilde{r}(t) = \left(\frac{1}{a(t)}\right) r(t), \tag{2.5}$$

and $a(t)$ is defined as

$$a(t) \triangleq \frac{s_{I_0}(t)}{\langle s_{I_0} \rangle}, \tag{2.6}$$

while $\tilde{s}(t)$ and $\tilde{s}_I(t)$ can be defined similarly. After passing through the equalizer/whitening filter, the optimum detection of the conventional hypothesis testing problem defined in (2.1) is equivalent to the detection of a signal of interest in white stationary process of time-invariant intensity given in (2.4) because there exists a one-to-one mapping between $r(t)$ and $\tilde{r}(t)$.

The sub-optimum detection of the conventional hypothesis testing problem defined in (2.1) is given by

$$r(t) = \begin{cases} s(t) + \tilde{s}_I(t), & \text{under } \mathcal{H}_1, \\ \tilde{s}_I(t), & \text{under } \mathcal{H}_0, \end{cases} \quad t \in T \tag{2.7}$$

which means that the sub-optimum detector does not apply any equalization to the received signal $r(t)$. Instead, it interprets $r(t)$ as a summation of the target signal and the white stationary time-invariant Gaussian interference (under $\mathcal{H}_1$). The time-varying cyclostationary interference $s_I(t)$ can be replaced with its time-average constant value $\langle s_{I_0} \rangle$. This, in turn, replaces the time-varying autocorrelation of $s_I(t)$ with the time-invariant autocorrelation of $\tilde{s}_I(t)$, given by

$$R_{\tilde{s}_I \tilde{s}_I}(\tau) = \mathbb{E}\left[s_I(t_1) s_I(t_2)\right] = \langle s_{I_0} \rangle \delta(\tau) \tag{2.8}$$

In this work, assuming the three cases for return signal as a) deterministic, b) with random phase, and c) random, for each case, the optimum, missynchronized, and sub-optimum detectors are presented. The optimum detector is the one where proper equalization is made to compensate for the interference component by passing through the equalizer/whitening filter and further processed for detection. If the equalization to the interference component is improper/ missynchronized, it is treated as missynchroized detection. Next, instead of equalizing/ compensating the interference, if it is treated as white Gaussian and further proceeded for detection, it is called the sub-optimal detection. The sub-optimal detection is considered because it is the traditional method (composite signal consisting of the intended signal component plus

white Gaussian noise) considered in the radar target detection process and to compare with the proposed optimal detector. In optimum detection, it is proposed that the interference is compensated by passing through the equalizer, but compensation need not be perfect all the time. Sometimes, it may be improper/missynchronized, to quantify its effect, and to compare with the optimal and sub-optimal detectors, the missynchroized detection scheme is also considered.

The hypothesis testing problem for optimum, missynchronized detection is given by (2.4), and for sub-optimum detection is given by (2.7). To derive the decision rules for the assumed cases, the Neyman-Pearson (NP) criterion based minimization of the probability of miss detection for a tolerable false alarm value is used (Kay, 1998). For the assumed NP criterion, the test is to compare the likelihood ratio to the threshold (Kay, 1998; Poor, 2013; Van Trees et $al.$, 2013). Therefore, for each assumed case of target reflected signal, the detection rule follows

$$\Lambda[\{r(t) : t \in T\}] \underset{\mathcal{H}_0}{\overset{\mathcal{H}_1}{\gtrless}} \gamma, \qquad (2.9)$$

where $\Lambda[.]$ is the likelihood ratio or sufficient statistic, defined in (2.10), and γ is the threshold that depends on the false alarm probability values and the signal-to-interference ratio (SIR) levels. Then,

$$\Lambda[\{r(t)\}] \triangleq \frac{f_{R/\mathcal{H}_1}(r/\mathcal{H}_1)}{f_{R/\mathcal{H}_0}(r/\mathcal{H}_0)}, \qquad (2.10)$$

where $f_{(.)}(.)$ denotes the corresponding conditional density function.

The performance of the receiver/detector is evaluated in terms of detection and false alarm probabilities, P_D, P_{FA}, respectively. The probability of miss detection $P_M = 1 - P_D$ can also be used as a measure of evaluation in place of P_D. Also, a modified CFAR receiver structure is proposed, and its performance analysis is presented. Further, the performance of the modified CFAR detector is compared with NP based detector.

2.2 Detection of target reflected radar signals and performance analysis

In this section, the detection rules are derived, and their structures are presented for the three different assumed cases of target reflected radar signals. The performances

of the resulting detection structures are thoroughly analysed in terms of P_D, P_{FA}, and receiver operating characteristic (ROC) curves.

2.2.1   Case I: Deterministic signals

The detection of completely deterministic signals in an in-band communication interference, which is unrealistic and assumed only to demonstrate the derivation process, is considered. The hypothesis testing for the scenario considered is given in (2.1) with $s(t)$ being defined as

$$s(t) \;=\; A \cos\left(\frac{2\pi Mt}{T}\right), \qquad t \in T \tag{2.11}$$

where M is a positive integer, A is the known amplitude and T is the time period.

Therefore, the optimum detector for (2.1), which is equivalent to (2.4), is given by (2.9) with

$$\Lambda[\{r(t)\}] = \int_T \{[s(t)]/a(t)\} r(t) \; dt \tag{2.12}$$

$$\gamma = \langle s_{I_0} \rangle \ln(\lambda) + \int_T \{[s^2(t)]/a(t)\} \; dt \tag{2.13}$$

where $s(t)$ is given in (2.11), $a(t)$ is given in (2.6) and λ is a deterministic quantity with prior probabilities. Equation (2.12) represents a whitening filter/equalizer followed by a correlator/matched filter receiver. Based on (2.12), the receiver structure for the case of detecting deterministic signals with an in-band interference is shown in Figure 2.3. The corresponding equivalent mathematical form of the receiver structure is shown in Figure 2.4.

$r(t)$
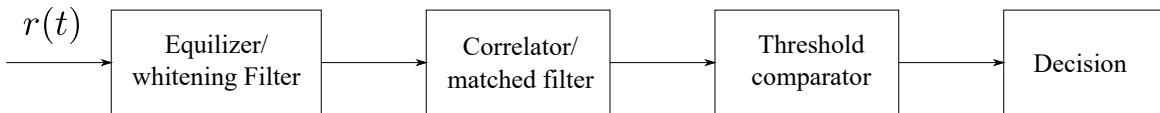
Figure 2.3: Optimum receiver structure for a deterministic signal buried in in-band wireless communication interference.

The performance of the receiver in (2.12) is specified by the ROC curves (Richards, 2014). Define the weighted energy as

$$E_a \triangleq \int_T [s^2(t)]/a(t) \; dt \tag{2.14}$$
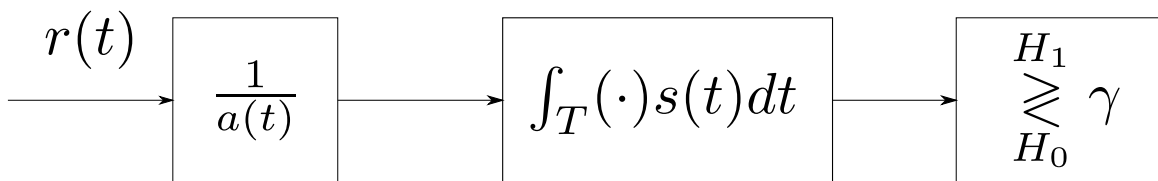
Figure 2.4: Mathematical form of an optimum receiver structure for a deterministic signal buried in in-band wireless communication interference.

As per the NP criterion, the threshold γ in (2.13) is determined from the probability density of $\Lambda[\{r(t)\}]$, defined in (2.12). From (2.12), we have

$$\mathbb{E}\left(\Lambda|\mathcal{H}_0\right) = 0, \ \mathbb{E}\left(\Lambda|\mathcal{H}_1\right) = E_a \text{ and } \mathrm{Var}\left(\Lambda\right) = \frac{\langle s_{I_0}\rangle E_a}{2} \tag{2.15}$$

where $\mathbb{E}(.)$ denotes the expectation operation, $\mathrm{Var}(.)$ denotes variance, and E_a is given in (2.14). Hence, the performance of the receiver is given by (Whalen, 2013)

$$P_{FA} = \frac{1}{\sqrt{2\pi}} \int_u^\infty \exp\{-x^2/2\} \ dx \tag{2.16}$$

$$P_D = \frac{1}{\sqrt{2\pi}} \int_{u-\alpha_a}^\infty \exp\{-x^2/2\} \ dx \tag{2.17}$$

where

$$u \triangleq \gamma \left(\frac{2}{\langle s_{I_0}\rangle E_a}\right)^{1/2} \tag{2.18}$$

$$\alpha_a^2 \triangleq \frac{2E_a}{\langle s_{I_0}\rangle} \tag{2.19}$$

α_a in (2.19) is interpreted as the SIR value.

Further, (2.16) and (2.17) is written as

$$P_{FA} = \frac{1}{2}\mathrm{erfc}\left(\frac{u}{\sqrt{2}}\right) \tag{2.20}$$

$$P_D = \frac{1}{2}\mathrm{erfc}\left(\frac{u-\alpha_a}{\sqrt{2}}\right) \tag{2.21}$$

From (2.20) and (2.21), the P_D as a function of P_{FA} is given by

$$P_D = \frac{1}{2}\mathrm{erfc}\left(\mathrm{erfc}^{-1}\left(2P_{FA}\right) - \frac{\alpha_a}{\sqrt{2}}\right) \tag{2.22}$$

The sub-optimum detector for the hypothesis testing problem defined in (2.1) for the case of $s(t)$ given in (2.11) will replace $s_{I_0}(t)$ with $\langle s_{I_0}\rangle$ in (2.12) and (2.13). The sub-optimum detector structure follows a similar structure as the optimum detector

shown in Figure 2.4, with $a(t) = 1$ or no equalization/whitening effect . The performance equations for the sub-optimum detector are given in (2.16) and (2.17), with u and α_a being replaced with $\frac{\tilde{u}}{\sqrt{J}}$ and $\frac{\alpha_1}{\sqrt{J}}$, respectively. Then, $\tilde{u}$ is given by

$$\tilde{u} \triangleq \gamma \left(\frac{2}{\langle s_{I_0} \rangle E_1} \right)^{1/2} \tag{2.23}$$

where E_1 is equal to E_a given in (2.14) with $a(t) = 1$. That is,

$$E_1 = E_a \Big|_{a(t)=1} = \int_T \{s^2(t)\} \ dt \tag{2.24}$$

and

$$J \triangleq \frac{\int_T [s^2(t)] a(t) dt}{\int_T [s^2(t)] dt} = \frac{E_{1/a}}{E_1} \tag{2.25}$$

Here, α_1 is given by

$$\alpha_1 = \sqrt{\frac{2E_1}{\langle s_{I_0} \rangle}} \tag{2.26}$$

where E_1 is given in (2.24).

In general, for the sub-optimum detector, J is always equal to 1. The J is interpreted as a tuning factor, which in turn relates to the SIR value given in (2.19). With these, the detection and false alarm probabilities for the sub-optimum detector, $\tilde{P}_D$ and $\tilde{P}_{FA}$, respectively, written as

$$\tilde{P}_{FA} = \frac{1}{2} \text{erfc} \left(\frac{\tilde{u}}{\sqrt{2J}} \right) \tag{2.27}$$

$$\tilde{P}_D = \frac{1}{2} \text{erfc} \left(\frac{\tilde{u} - \alpha_1}{\sqrt{2J}} \right) \tag{2.28}$$

Similar to (2.22), from (2.27) and (2.28), we can write

$$\tilde{P}_D = \frac{1}{2} \text{erfc} \left[\text{erfc}^{-1} \left(2\tilde{P}_{FA} \right) - \frac{\alpha_1}{\sqrt{2J}} \right] \tag{2.29}$$

The SIR boost B, which is required to make the performance of the optimum and sub-optimum detectors equal in the presence of cyclostationary interference. For a given P_{FA}, to make $P_D = \tilde{P}_D$, the required value of B that is given by

$$B \triangleq \frac{J\alpha_a^2}{\alpha_1^2} = \frac{JE_a}{E_1} \tag{2.30}$$

Lemma 1. *The value of the SIR boost B defined in (2.30) is always greater than or equal to* 1.

Proof. From (2.30), using (2.19), (2.25), (2.26), we can write

$$B = \frac{E_a E_{1/a}}{E_1^2} \tag{2.31}$$

From the Cauchy–Schwarz inequality (Steele, 2004), we can write

$$\left[\int_T s^2(t)dt\right]^2 \leq \int_T [s^2(t)]a(t)dt \int_T [s^2(t)]\frac{1}{a(t)}dt \tag{2.32}$$

which leads to $E_1^2 \leq E_a E_{1/a}$. Thus confirming that the SIR boost B is always greater than or equal to 1 (i.e., $B \geq 1$ always). $\qquad\square$

The mathematical model for the wireless communication interference $s_I(t)$ is considered below.

A   Example: Cyclostationary/periodic square wave interference intensity

Consider $s_I(t)$ as a periodic square wave over one period, which is given by

$$s_I(t) = \begin{cases} \langle s_{I_0}\rangle l & 0 \leq t \leq nT, \\ \langle s_{I_0}\rangle m & nT \leq t \leq T. \end{cases} \tag{2.33}$$

For self-consistency, assume

$$l = n^{-1}(1 - mn), \qquad 0 < m, n \leq 1 \tag{2.34}$$

Over one period, this kind of interference is expected if there is substantial interference for some time and less interference for the remaining time.

From (2.14), (2.24), (2.25) for $s(t)$ and $s_I(t)$ given in (2.11) and (2.33), respectively, we have

$$E_1 = \frac{A^2}{2}T \tag{2.35}$$

$$E_a = E_1\left\{\frac{n}{l} + \frac{1-n}{m} + \left[\frac{mn - ln}{4\pi Mlmn}\right]\sin(4\pi Mn)\right\} \tag{2.36}$$

$$J = \left\{ln + m(1 - n) + \left[\frac{ln - mn}{4\pi Mn}\right]\sin(4\pi Mn)\right\} \tag{2.37}$$

While from (2.30), using (2.35), (2.36), (2.37), B is written as

$$B = \left\{n + \frac{l(1-n)}{m} + \left[\frac{mn - ln}{4\pi Mmn}\right]\sin(4\pi Mn)\right\} \times$$
$$\left\{n + \frac{m(1-n)}{l} + \left[\frac{ln - mn}{4\pi Mln}\right]\sin(4\pi Mn)\right\} \tag{2.38}$$

For time-symmetric $s_I(t)$ given in (2.33) $\left(\text{i.e., for } n = \frac{1}{2}\right)$, from (2.38), (2.34), we have $B = [m(2-m)]^{-1}$. From (2.34), as m lies between 0 and 1, B is always positive, which supports the previously mentioned Theorem 1. For smaller values of m, the value of B is very large, which means that even if there is a high interference over a shorter interval, the optimum detector compensates its effect, whereas the sub-optimum detector does not.

From (2.22), (2.29), (2.30), (2.35), (2.36), (2.37), the detection and false alarm probabilities of the optimum and sub-optimum detector as a function of SIR and SIR boost are written as

$$P_D = \frac{1}{2}\text{erfc}\left[\text{erfc}^{-1}(2P_{FA}) - \sqrt{\frac{B}{2}}\alpha_1\right] \tag{2.39}$$

$$\tilde{P}_D = \frac{1}{2}\text{erfc}\left[\text{erfc}^{-1}\left(2\tilde{P}_{FA}\right) - \frac{\alpha_1}{\sqrt{2}}\right] \tag{2.40}$$

B   The penalty due to missynchronization

In practice, a meaningful performance comparison between the optimum and sub-optimum detectors in the presence of in-band wireless communication interference can be found by comparing the P_D and P_{FA} of the missynchronized optimum detector with the corresponding sub-optimum detector. Denote $\hat{a}(t)$ as the missynchronized whitening/equalizing factor. Also define $\hat{P}_D$ and $\hat{P}_{FA}$ as the detection and false alarm probabilities of the missynchronized optimum detector, respectively. The equations for $\hat{P}_{FA}$, $\hat{P}_D$ are given by (2.16), (2.17) with u and α_a being replaced with $\frac{\hat{u}}{\sqrt{\hat{J}}}$ and $\frac{\alpha_{\hat{a}}}{\sqrt{\hat{J}}}$, respectively. Then, $\hat{u}$ is given by

$$\hat{u} \triangleq \gamma \left(\frac{2}{\langle s_{I_0}\rangle E_{\hat{a}}}\right)^{1/2} \tag{2.41}$$

where $E_{\hat{a}}$ is given in (2.14) by replacing $a(t)$ with $\hat{a}(t)$ and $\hat{J}$ is defined as

$$\hat{J} \triangleq \frac{\int_T \left\{[s^2(t)]\left(\frac{a(t)}{\hat{a}^2(t)}\right)\right\} dt}{\int_T \left\{[s^2(t)]\left(\frac{1}{\hat{a}(t)}\right)\right\} dt} = \frac{E_{\hat{a}^2/a}}{E_{\hat{a}}} \tag{2.42}$$

The missynchronized SIR $\alpha_{\hat{a}} = \sqrt{\frac{2E_{\hat{a}}}{\langle s_{I_0}\rangle}}$. Therefore, it follows from (2.16), (2.17), (2.41), (2.42) that

$$\hat{P}_{FA} = \frac{1}{2}\text{erfc}\left(\frac{\hat{u}}{\sqrt{2\hat{J}}}\right) \tag{2.43}$$

$$\hat{P}_D = \frac{1}{2}\text{erfc}\left(\frac{\hat{u} - \alpha_{\hat{a}}}{\sqrt{2\hat{J}}}\right) \tag{2.44}$$

Similar to (2.22), from (2.43) and (2.44), the $\hat{P}_D$ is written as

$$\hat{P}_D = \frac{1}{2}\text{erfc}\left[\text{erfc}^{-1}\left(2\hat{P}_{FA}\right) - \frac{\alpha_{\hat{a}}}{\sqrt{2\hat{J}}}\right] \tag{2.45}$$

Similar to (2.30), the SIR boost is given by

$$\hat{B} = \frac{\hat{J}E_a}{E_{\hat{a}}} = \frac{\hat{J}\alpha_a^2}{\alpha_{\hat{a}}^2} = \frac{E_a E_{\hat{a}^2/a}}{E_{\hat{a}}^2} \geq 1 \tag{2.46}$$

Thus, from (2.45) and (2.46), it follows that

$$\hat{P}_D = \frac{1}{2}\text{erfc}\left[\text{erfc}^{-1}\left(2\hat{P}_{FA}\right) - \frac{\alpha_a}{\sqrt{2\hat{B}}}\right] \tag{2.47}$$

For the signal $s(t)$ given in (2.11), with interference characteristics given in (2.33), the performance of the missynchronized optimum detector is analysed here. Missynchronization is mathematically modeled as

$$\hat{a}(t) = a\left(t + \varpi\frac{T}{2}\right), \qquad 0 \leq \varpi \leq 1 \tag{2.48}$$

For mathematical simplicity, it is assumed that $n = \frac{1}{2}$. Then, from (2.33), the $s_I(t)$ is written as

$$s_I(t) = \begin{cases} \langle s_{I_0}\rangle l & 0 \leq t \leq \frac{T}{2}, \\ \langle s_{I_0}\rangle m & \frac{T}{2} \leq t \leq T. \end{cases} \tag{2.49}$$

where $l = (2 - m)$ and $0 < m \leq 1$.

The performance of this missynchronized optimum receiver is evaluated using (2.47). For the worst-case (100%) analysis of missynchronized optimum receiver, the $\varpi = 1$ is assumed. From (2.46), (2.49), we have

$$\hat{B} = \frac{l^2}{m(l + m)} = \frac{(2 - m)^2}{2m} \tag{2.50}$$

and from (2.19), (2.26), (2.49), we also have

$$\alpha_a = \alpha_1\sqrt{\frac{l + m}{2lm}} = \frac{\alpha_1}{\sqrt{(2 - m)m}} \tag{2.51}$$

25

Thus, from (2.47), (2.50), and (2.51), we have

$$\hat{P}_D = \frac{1}{2}\text{erfc}\left[\text{erfc}^{-1}\left(2\hat{P}_{FA}\right) - \frac{\alpha_1}{(2-m)^{3/2}}\right] \tag{2.52}$$

Similarly, for the 50% missynchronization case ($\varpi = 1/2$), from (2.46)

$$\hat{B} = \frac{1}{2}\left\{1 + \frac{l^2}{m(l+m)}\right\} = \frac{1}{2}\left\{1 + \frac{(2-m)^2}{2m}\right\} \tag{2.53}$$

Thus, from (2.47)

$$\hat{P}_D = \frac{1}{2}\text{erfc}\left[\text{erfc}^{-1}\left(2\hat{P}_{FA}\right) - \frac{\alpha_1}{\sqrt{(2m - m^2)\left(1 + \frac{(2-m)^2}{2m}\right)}}\right] \tag{2.54}$$

2.2.2 Case II: Signals with random phase

In this subsection, the signal used for the hypothesis testing problem defined in (2.1) is

$$s(t) = s(t,\phi) = A\cos\left(\frac{2\pi M t}{T} + \phi\right), \qquad t \in T \tag{2.55}$$

where M is a positive integer, and ϕ is a uniformly distributed random variable over the interval 0 to 2π. The probability density function (PDF) of ϕ is given by

$$f(\phi) = \begin{cases} \frac{1}{2\pi}, & \phi \in [0, 2\pi], \\ 0, & \text{elsewhere.} \end{cases} \tag{2.56}$$

The (2.55) can also be represented in its complex envelope form, given by

$$s(t,\phi) = Re\left\{A\exp\left[j\left(\frac{2\pi M t}{T} + \phi\right)\right]\right\}, \qquad t \in T \tag{2.57}$$

The likelihood ratio defined in (2.10) is generalized for the $s(t)$ defined in (2.55) as

$$\Lambda[\{r(t)\}] \triangleq \mathbb{E}_\phi\left[\frac{f_{R/\mathcal{H}_1}(r/\mathcal{H}_1)}{f_{R/\mathcal{H}_0}(r/\mathcal{H}_0)}\right] \tag{2.58}$$

where $\mathbb{E}_\phi[.]$ denotes the expectation operation.

The optimum detector for the hypothesis testing problem defined in (2.1) for the $s(t)$ given in (2.55) having $\Lambda[\{r(t)\}]$ as (2.58) is given by (2.9) with

$$\Lambda[\{r(t)\}] \triangleq \int_\phi \exp\left\{\frac{2}{\langle s_{I_0}\rangle}\int_T\left[\frac{s(t,\phi)}{a(t)}\right]r(t)\,dt\right\}f(\phi)\,d\phi, \tag{2.59}$$

$$\gamma \triangleq \lambda\exp\left\{\frac{1}{\langle s_{I_0}\rangle}\int_T\frac{s^2(t,\phi)}{a(t)}\,dt\right\}, \tag{2.60}$$

26

where $f(\phi)$ is defined in (2.56).

The likelihood ratio defined in (2.59) is written for the $s(t, \phi)$, defined in (2.55) as (Whalen, 2013)

$$\Lambda[\{r(t)\}] = I_0 \left(\frac{2Aq}{\langle s_{I_0} \rangle} \right) \qquad (2.61)$$

where $I_0(.)$ in (2.61) is the modified Bessel function of the first kind of order zero (Abramowitz and Stegun, 1948) and q is defined as

$$q = \frac{1}{2} \left| \int_T \frac{r(t)}{a(t)} \exp \left(-j \frac{2\pi M t}{T} \right) dt \right| \qquad (2.62)$$

In this case, from (2.61) the hypothesis test is

$$I_0 \left(\frac{2Aq}{\langle s_{I_0} \rangle} \right) \mathop{\gtrless}_{\mathcal{H}_0}^{\mathcal{H}_1} \gamma \qquad (2.63)$$

Since, the Bessel function $I_0(.)$ is a monotonically increasing function, the test is carried out by comparing q to threshold γ', i.e.,

$$q \mathop{\gtrless}_{\mathcal{H}_0}^{\mathcal{H}_1} \gamma' \qquad (2.64)$$

For mathematical convenience, the test is carried out with q^2 as

$$q^2 \mathop{\gtrless}_{\mathcal{H}_0}^{\mathcal{H}_1} \gamma'' \qquad (2.65)$$

This test is called the quadrature/square law detector (Whalen, 2013) for the problem defined in (2.1), when the signal has an unknown/random phase (for the $s(t)$ given in (2.55)). The receiver structure for the detection equation in (2.65) is shown in Figure 2.5.

The correlation operation in (2.62) is also represented as the sample output of the matched filter, with the impulse response as

$$h(t) = \exp \left(-j \frac{2\pi M (T - t)}{T} \right) \qquad (2.66)$$

In terms of $h(t)$ given in (2.66), (2.62) is rewritten as

$$q = \frac{1}{2} \left| \frac{r(t)}{a(t)} * h(t) \right| \qquad (2.67)$$

where $*$ represents the convolution operation.

The detection equations in (2.62), (2.67) are the base-band level representations, that are appropriate for a digital receiver. For analog processing, the same manipulations can be carried out at the band pass level or at any convenient radio frequency
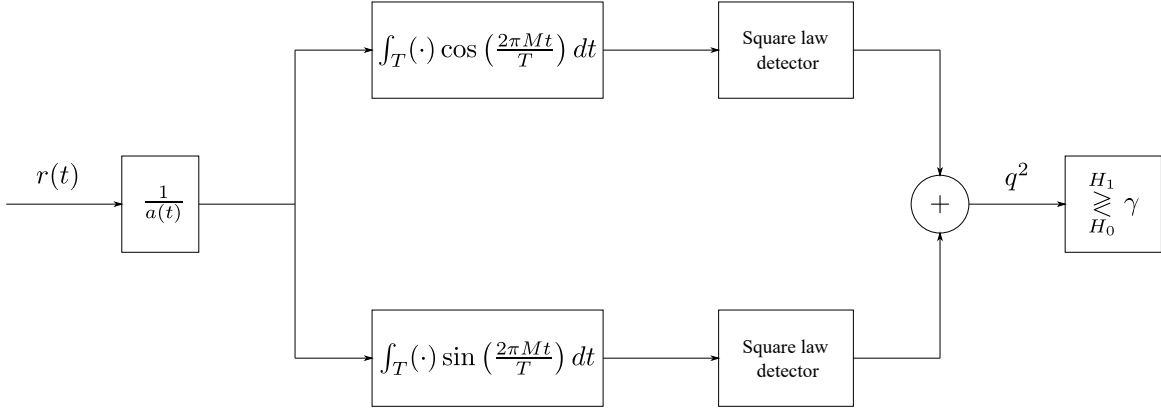
Figure 2.5: Optimum receiver structure for a known signal with random phase buried in in-band wireless communication interference.

(RF) band, to which the RF signals are down-converted (e.g., intermediate frequency (IF) band) (Whalen, 2013). The receiver structure for the matched filter based detection equation in (2.67) is shown in Figure 2.6.
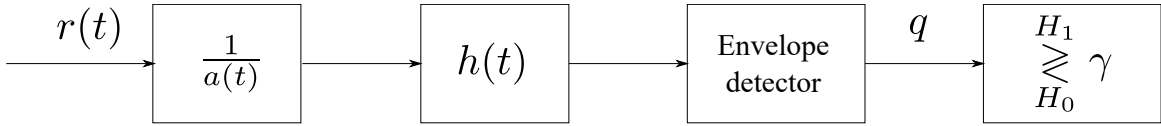
Figure 2.6: Matched filter form of the optimum receiver structure for a known signal with random phase buried in in-band wireless communication interference.

Now, the performance of the detector represented in (2.64) is evaluated in-terms of P_D and P_{FA}. For this, the density function of the test statistics q under two hypothesis $\mathcal{H}_1, \mathcal{H}_0$ is required, given by (Whalen, 2013)

$$f_{\mathcal{H}_1}(q) = \frac{q}{\sigma_a^2} \exp\left[-\frac{q^2 + \zeta_a^2}{2\sigma_a^2}\right] I_0 \left(\frac{q\zeta_a}{\sigma_a^2}\right) \tag{2.68}$$

$$f_{\mathcal{H}_0}(q) = \frac{q}{\sigma_a^2} \exp\left[-\frac{q^2}{2\sigma_a^2}\right] \tag{2.69}$$

where

$$\sigma_a^2 = \frac{\langle s_{I_0} \rangle}{2} \int_T \frac{\cos^2\left(\frac{2\pi Mt}{T}\right)}{a(t)} \, dt \tag{2.70}$$

and

$$\zeta_a = \frac{A \int_T \frac{1}{a(t)} dt}{2} \tag{2.71}$$

The detailed proof to obtain $f_{\mathcal{H}_1}(q)$, $f_{\mathcal{H}_0}(q)$ is availabel in Appendix A.1.

Under $\mathcal{H}_1$ and $\mathcal{H}_0$, the density functions of the sufficient statistics q given in (2.68) and (2.69), represent the Rician and Rayleigh densities, respectively. Using the detection statistics defined in (2.64), the probability of false alarm P_{FA} is obtained as

$$P_{FA} = \int_{\gamma'}^{\infty} f_{\mathcal{H}_0}(q) \, dq = \exp\left(-\frac{\gamma'^2}{2\sigma_a^2}\right) \tag{2.72}$$

Then, it is rewritten as

$$\frac{\gamma'}{\sigma_a} = \sqrt{-2\ln(P_{FA})} \tag{2.73}$$

Using (2.68), the probability of detection P_D is

$$P_D = \int_{\gamma'}^{\infty} f_{\mathcal{H}_1}(q) \, dq = Q_M\left(\frac{\zeta_a}{\sigma_a}, \frac{\gamma'}{\sigma_a}\right) \tag{2.74}$$

where $Q_M(.)$ is the Marcum Q-function (Nuttall, 1975; Proakis and Salehi, 2007).

The sub-optimum detector for the hypothesis testing problem, as given in (2.1), $s(t)$ defined in (2.55) is given in (2.9), where $\Lambda\left[r(t)\right]$ and γ are given in (2.59) and (2.60), respectively, with $a(t) = 1$. Its structure is similar to the one in Figure 2.5, without the $\frac{1}{a(t)}$ block (i.e., $a(t) = 1$). Similar to (2.63), the detection statistics for the sub-optimum detector is given by

$$I_0\left(\frac{2A\tilde{q}}{\langle s_{I_0}\rangle}\right) \underset{\mathcal{H}_0}{\overset{\mathcal{H}_1}{\gtrless}} \gamma \tag{2.75}$$

Since the Bessel function is monotonic, the sufficient statistic is

$$\tilde{q} \underset{\mathcal{H}_0}{\overset{\mathcal{H}_1}{\gtrless}} \gamma' \tag{2.76}$$

with $\tilde{q}$ as

$$\tilde{q} = \frac{1}{2}\left| \int_T r(t) \exp\left(-j\frac{2\pi M t}{T}\right) dt \right| \tag{2.77}$$

Similarly, from (2.72) and (2.74), the performance equations for the sub-optimum detector are given by

$$\tilde{P}_{FA} = \exp\left(-\frac{\gamma'^2}{2\sigma_1^2}\right) \tag{2.78}$$

$$\tilde{P}_D = Q_M\left(\frac{\zeta_1}{\sigma_1}, \frac{\gamma'}{\sigma_1}\right) \tag{2.79}$$

where σ_1 and ζ_1 are similar to the forms (2.70) and (2.71), respectively, with $a(t) = 1$. For the performance analysis, an example for the $s_I(t)$ is considered below.

29

A   Example

For a square wave $s_I(t)$ expressed in (2.33), from (2.70) and (2.71), we have

$$\zeta_a = \frac{AT}{2}\left(\frac{n}{l} + \frac{1-n}{m}\right) \tag{2.80}$$

$$\sigma_a^2 = \frac{\langle s_{I_0} \rangle T}{4}\left\{\frac{n}{l} + \frac{1-n}{m} + \left[\frac{mn-ln}{4\pi Mlmn}\right]\sin(4\pi Mn)\right\} \tag{2.81}$$

Therefore,

$$\frac{\zeta_a}{\sigma_a} = \left(\frac{\zeta_a^2}{\sigma_a^2}\right)^{\frac{1}{2}} = \sqrt{\frac{2E_1}{\langle s_{I_0} \rangle}c} \tag{2.82}$$

where E_1 is defined in (2.35) and c some constant, given by

$$c = \frac{\left(\frac{n}{l} + \frac{1-n}{m}\right)^2}{\left\{\frac{n}{l} + \frac{1-n}{m} + \left[\frac{mn-ln}{4\pi Mlmn}\right]\sin(4\pi Mn)\right\}}.$$

It is conventional to define the ratio in (2.82) as the signal-to-interference ratio (SIR) (Whalen, 2013), given by

$$\alpha_a(\text{dB}) = 20\log\left(\frac{\zeta_a}{\sigma_a}\right) = 10\log\left(\frac{2E_1}{\langle s_{I_0} \rangle}c\right) \tag{2.83}$$

Therefore, from (2.74) in conjunction with (2.82) and (2.83), we have

$$P_D = Q_M\left(\sqrt{\left[\frac{2E_1}{\langle s_{I_0} \rangle} + c\right](dB)}, \sqrt{-2\ln(P_{FA})}\right) \tag{2.84}$$

Similarly, for the sub-optimum detection, from (2.79)

$$\tilde{P}_D = Q_M\left(\sqrt{\left[\frac{2E_1}{\langle s_{I_0} \rangle}\right](dB)}, \sqrt{-2\ln\left(\tilde{P}_{FA}\right)}\right) \tag{2.85}$$

For a given P_{FA}, from (2.84) and (2.85), c is interpreted as the SIR boost.

2.2.3   Case III: Random signals

In Case II, the signal $s(t)$ specified in (2.55) has a deterministic complex envelope $A\exp\left[j\left(\frac{2\pi Mt}{T}\right)\right]$, with random phase ϕ. While this is an acceptable model in some scenarios, a more realistic model is a signal that has both, random amplitude and phase. The emitted RF signal undergoes refraction, reflection, diffraction, absorption, polarization and scattering over the wireless medium (Seybold, 2005; Jordan and

Balmain, 1968). Thus, in contrast to the first two cases, the signal $s(t)$ that has been considered here is a more realistic signal, with random amplitude and phase. Here, $s(t)$ is given by

$$s(t) = As(t, \phi) = A \cos \left(\frac{2\pi M t}{T} + \phi \right), \qquad t \in T \tag{2.86}$$

where M is a positive integer, the phase ϕ is a uniformly distributed random variable and amplitude A follows the Rayleigh density, whose PDF is given by

$$f_A(a) = \frac{A}{\sigma_{A_0}^2} \exp \left(\frac{-A^2}{2\sigma_{A_0}^2} \right) u(A) \tag{2.87}$$

with density parameter

$$\sigma_{A_0}^2 = \frac{\mathbb{E}_A \left(A^2 \right)}{2} \tag{2.88}$$

where $\mathbb{E}(.)$ denotes the expectation operation, and $u(A)$ is the unit-step function.

The assumption of (2.87) is valid due to the fact that the received signal is the coherent summation of all the reflected signals from small scattering elements on a large object (i.e., target) (Whalen, 2013; Richards, 2014). Therefore, for the $s(t)$ defined in (2.86), the optimum detection rule for the hypothesis testing problem defined in (2.1) is given by (2.9) with

$$\Lambda[\{r(t)\}] \triangleq \int_\phi \int_A \exp \left\{ \frac{2}{\langle s_{I_0} \rangle} \int_T \left[\frac{As(t, \phi)}{a(t)} \right] r(t) \, dt \right\} f_A(a) \, f(\phi) \, dA \, d\phi \tag{2.89}$$

$$\gamma \triangleq \lambda \exp \left\{ \frac{1}{\langle s_{I_0} \rangle} \mathbb{E}_A \left(\int_T \frac{As^2(t, \phi)}{a(t)} \, dt \right) \right\} \tag{2.90}$$

From (2.89) and (2.90), after taking the expectation, the optimum detector becomes independent of the unknown random variables A and ϕ. Then, the optimum detector is given by $q > \gamma$ (under $\mathcal{H}_1$), where q is defined in (2.62). The detector structure follows a similar structure as in Case II (only random phase), as shown in Figure 2.5. However, in contrast to Case II, the performance equations (i.e., P_D, P_{FA}) depends on A. Using (2.74) and (2.87), the detection probability P_D is given by

$$P_D = \mathbb{E}_A [P_D(A)] = \mathbb{E}_A \left[Q_M \left(\frac{\zeta_a}{\sigma_a}, \frac{\gamma}{\sigma_a} \right) \right] \tag{2.91}$$

where $\mathbb{E}_A(.)$ denotes expectation operation with respect to A, whose PDF is given in (2.87), and the remaining parameters follow (2.74).

After taking the expectation, the closed-form expression for P_D is given by (Grad-shteyn and Ryzhik, 2014)

$$P_D = \exp\left\{\frac{-2\gamma^2}{\left[\sigma_{A_0}^2 T^2 g^2 + 4\sigma_a^2\right]}\right\} \tag{2.92}$$

where

$$g = \left(\frac{n}{l} + \frac{1-n}{m}\right) \tag{2.93}$$

The sub-optimum detector for the $s(t)$ defined in (2.86), with the hypothesis testing problem defined in (2.1), follows (2.89) and (2.90) with $a(t) = 1$. The receiver structure also follows a similar structure as the optimum detector, as shown in Figure 2.5, without the $a(t)$ block. Similar to (2.92), the detection probability for the sub-optimum detector is given by

$$\tilde{P}_D = \exp\left\{\frac{-2\gamma^2}{\sigma_{A_0}^2 T^2 + 4\sigma_1^2}\right\} \tag{2.94}$$

Here, P_{FA} and $\tilde{P}_{FA}$ are similar to those in (2.72) and (2.78), respectively. Closed-form expressions for the detection and false alarm probabilities are given by considering some examples for interference.

A   Example

For a square wave $s_I(t)$ expressed in (2.33), from (2.70), we have

$$\sigma_1^2 = \frac{\langle s_{I_0}\rangle T}{4} \tag{2.95}$$

$$\sigma_a^2 = \sigma_1^2 h \tag{2.96}$$

where

$$h = \left\{\frac{n}{l} + \frac{1-n}{m} + \left[\frac{mn-ln}{4\pi Mlmn}\right]\sin(4\pi Mn)\right\} \tag{2.97}$$

As the amplitude of $s(t)$ defined in (2.86) is random, we define the average energy E_{avg} rather than the instantaneous energy E, which is given by

$$E_{avg} = \mathbb{E}_A(A^2)\frac{T}{2} = \sigma_{A_0}^2 T \tag{2.98}$$

where $\sigma_{A_0}^2$ is defined in (2.88).

The average SIR is defined as

$$\alpha_{avg}^2 = \frac{2E_{avg}}{\langle s_{I_0}\rangle} = \frac{\sigma_{A_0}^2 T^2}{2\sigma_1^2} \tag{2.99}$$

For the optimum detector, from (2.73), we have

$$\gamma^2 = -2\sigma_a^2 \ln(P_{FA}) \tag{2.100}$$

From (2.92), (2.99) and (2.100), we can write

$$P_D = P_{FA}^{\left(1+\frac{\alpha_{avg}^2}{2}c\right)^{-1}} = P_{FA}^{\left(1+\frac{E_{avg}}{\langle s_{I_0}\rangle}c\right)^{-1}}, \tag{2.101}$$

where

$$c = \frac{g^2}{h}, \tag{2.102}$$

whose g and h are defined in (2.93) and (2.97) respectively.

Similarly, for the sub-optimum case, from (2.78), we have

$$\gamma^2 = -2\sigma_1^2 \ln\left(\tilde{P}_{FA}\right) \tag{2.103}$$

From (2.94), (2.99) and (2.103), we can write

$$\tilde{P}_D = \tilde{P}_{FA}^{\left(1+\frac{\alpha_{avg}^2}{2}\right)^{-1}} = \tilde{P}_{FA}^{\left(1+\frac{E_{avg}}{\langle s_{I_0}\rangle}\right)^{-1}} \tag{2.104}$$

By looking at (2.101) and (2.104), the term c is interpreted as an SIR boost that has been achieved by the optimum detector to compensate for the effect of the interference and to get a better P_D compared to the sub-optimum one.

2.2.4 Constant-False-Alarm Rate (CFAR) detector

This sub-section presents the detection of random signals in an in-band communication interference using the cell-averaging CFAR detector. The NP detector sets a fixed threshold based on the known initial interference power statistics and desired P_{FA}. It does not adapt its threshold for the change in interference power (Richards, 2014). Also, knowing the interference statistics is impossible, and calculating the threshold is difficult. To overcome this problem, the CFAR calculates the interference power from its neighbouring cells and sets the threshold adaptively, and maintains the constant desired P_{FA} (Richards, 2014; Richards *et al.*, 2010). Here, the in-band wireless communication transmitters (IWCTs) inject direct interference of higher values (Blunt and Perrins, 2018), applying the CFAR directly on the received data may lead to miss detection of the target (Zilz and Bell, 2018; Sanders *et al.*, 2006). Further,

the threshold in the cell-averaging CFAR is calculated as the average of the neighbouring cells, which also contains the interference that sets the threshold higher. In this chapter, CFAR refers to cell-averaging based CFAR, unless specified. So, using CFAR as a detector in RadComm spectrum sharing scenarios demands some kind of preprocessing to nullify the in-band interference. In this research work, a modified CFAR detector is considered, where the received data is first passed through the equalizer/whitening filter followed by the CFAR detector and a decision-maker. It is assumed that the equalizer/whitening filter compensates for the interference and makes it white Gaussian. The modified CFAR receiver structure is shown in Figure 2.7. The received signal for the hypothesis testing problem given in (2.1) with the modified CFAR receiver follows (2.4) (after preprocessing). The signal considered here are random signals and follow Rayleigh voltage, given by (2.86). The samples received after passing through the equalizer and A/D converter are stored in the data window.
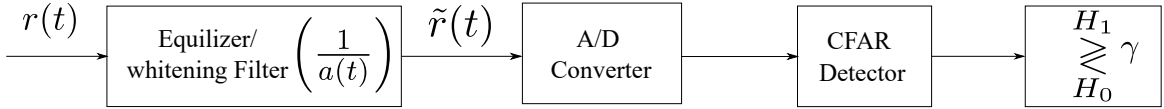
Figure 2.7: Modified CFAR receiver structure.

Figure 2.8 shows the architecture of the CFAR detector. The CFAR window consists of a cell under test (CUT), lagging, leading reference windows, and guard cells. The CUT is the resolution cell to which the CFAR threshold is applied. With the assumption that target may be present in the neighbouring cells of the CUT, a fixed number of cells surrounding the CUT are treated as guard cells $(\tilde{r}_{1_G}, \ldots, \tilde{r}_{N_G})$, the data in the guard cells is excluded for threshold calculation. This CFAR window slides over the data window to detect the target presence. The CFAR detector makes the decision of whether the target is present (Hypothesis $\mathcal{H}_1$) or not (Hypothesis $\mathcal{H}_0$), by comparing the square law output of the CUT data sample $(\tilde{r}_{\text{CUT}})$, with the adaptive threshold, and it is calculated using the N neighbouring cells $(\tilde{r}_1, \ldots, \tilde{r}_N)$. The decision rule is given by

$$\text{Decision} = \begin{cases} \mathcal{H}_1, & |\tilde{r}_{\text{CUT}}|^2 > k\frac{1}{N}\sum_{n=1}^{N}|\tilde{r}_n|^2, \\ \mathcal{H}_0, & |\tilde{r}_{\text{CUT}}|^2 \le k\frac{1}{N}\sum_{n=1}^{N}|\tilde{r}_n|^2. \end{cases} \qquad (2.105)$$

Here, constant k is called proportionality CFAR constant and is a function of desired P_{FA}.

Figure 2.8: The Constant-False-Alarm Rate (CFAR) detector architecture.

Here the performance of the modified CFAR detector is evaluated in terms of P_D and P_{FA}. After the equalization, the interference statistics become white Gaussian, and the target return signal follows Rayleigh voltage statistics. Hence the probability density of the square law output of the received signal $z = |\tilde{r}|^2$ under $\mathcal{H}_0$ and $\mathcal{H}_1$ hypothesis follows exponential distribution (Levanon, 1988), which is represented as

$$f_{\mathcal{H}_0}(z) = \begin{cases} \frac{1}{\sigma_a^2} \exp\left(\frac{-z}{\sigma_a^2}\right), & z \geq 0 \\ 0, & z < 0 \end{cases} \tag{2.106}$$

$$f_{\mathcal{H}_1}(z) = \begin{cases} \frac{1}{\zeta_a^2 + \sigma_a^2} \exp\left(\frac{-z}{\zeta_a^2 + \sigma_a^2}\right), & z \geq 0 \\ 0, & z < 0 \end{cases} \tag{2.107}$$

Here, σ_a, ζ_a are defined in (2.70), and (2.71) respectively.

The (2.107) is rewritten in terms of SIR as

$$f_{\mathcal{H}_1}(z) = \begin{cases} \frac{1}{\sigma_a^2(1+\text{SIR}_a)} \exp\left(\frac{-z}{\sigma_a^2(1+\text{SIR}_a)}\right), & z \geq 0 \\ 0, & z < 0 \end{cases} \tag{2.108}$$

where $\text{SIR}_a = \frac{\zeta_a^2}{\sigma_a^2}$.

For a square wave $s_I(t)$ expressed in (2.33), using (2.70), and (2.71), the SIR_a is given

by

$$\text{SIR}_a = \frac{2E_{avg}}{\langle s_{I_0} \rangle} \times c, \tag{2.109}$$

where E_{avg}, c are defined in (2.98), (2.102).

For the decision rule given in (2.105), using the (2.106), (2.108), the average P_D and P_{FA} is given by (Richards *et al.*, 2010)

$$P_D = \left(1 + \frac{k/N}{1 + \left(\frac{2E_{avg}}{\langle s_{I_0} \rangle} \right) c} \right)^{-N}$$

$$P_{FA} = \left(1 + \frac{k}{N} \right)^{-N} \tag{2.110}$$

To plot the ROC curves, (2.110) is rewritten by eliminating the CFAR constant k as

$$\left. \frac{2E_{avg}}{\langle s_{I_0} \rangle} \right|_{CFAR} = \frac{(P_D/P_{FA})^{1/N} - 1}{c \left(1 - P_D^{1/N} \right)} \tag{2.111}$$

Since CFAR compares the square law output to the adaptive threshold for decision, the square law NP detector is considered for comparison. The P_D and P_{FA} for square law NP detector is given by

$$P_D = \exp \left(\frac{-T}{\sigma_a^2 (1 + \text{SIR}_a)} \right)$$

$$P_{FA} = \exp \left(\frac{-T}{\sigma_a^2} \right) \tag{2.112}$$

where, SIR_a is defined in (2.109), T is NP threshold.

Similar to (2.111), (2.112) is rewritten by eliminating the threshold T as

$$\left. \frac{2E_{avg}}{\langle s_{I_0} \rangle} \right|_{NP} = \frac{1}{c} \left[\frac{\ln (P_{FA})}{\ln (P_D)} - 1 \right] \tag{2.113}$$

The ROC curves for the modified CFAR and NP detectors are plotted using (2.111) and (2.113).

2.3   Numerical results and discussions

Based on the theoretical analysis presented in Section 2.2, this Section presents the numerical results and discussions. Figures 2.9–2.14 show the receiver performance for the completely deterministic case considered in Section 2.2.1 with varying degrees of interference intensity (given by parameter m) and varying degrees of non-stationarity/symmetry (given by parameter n). Figures 2.9 and 2.10 show the receiver

performance in terms of detection probability as a function of SIR with a fixed probability of false alarm. Figures 2.11 and 2.12 show the receiver operating characteristic (ROC) curves for the same case. Figures 2.13 and 2.14 show the receiver performance due to missynchronization. Figures 2.15–2.16 show the receiver performance for the moderately acceptable random phase case considered in Section 2.2.2. In particular, Figure 2.15 shows the detection performance in terms of detection probability as a function of SIR for a fixed false alarm probability, while Figure 2.16 shows the corresponding ROC curves. The rest of the figures show the receiver performance for the realistic case random amplitude and phase considered in Section 2.2.3.

For the unrealistic deterministic signals case in Section 2.2.1, based on (2.39) and (2.40), Figure 2.9 shows the detection probability of the receiver as a function of SIR $\left(\frac{2E_1}{\langle s_{I_0} \rangle} \right)$ with varying degrees of interference intensity (m) for a fixed probability of false alarm $(P_{FA} = 10^{-2})$ and a fixed degree of non-stationarity/symmetry $\left(n = \frac{1}{2} \right)$. With the assumed square wave interference defined in (2.33), the interpretation of m and n is as follows: The value of n defines the non-stationarity/symmetry of the square wave, whereas the value of m defines the amplitude/intensity of the square wave interference. For example, for one period T and $n = \frac{1}{2}$, $m = \frac{1}{4}$ means that the square wave interference is symmetric, the first-half amplitude/intensity $\left(\text{which is equal to } l = n^{-1}(1 - mn) = \frac{7}{4} \right)$ of the square wave is higher, and that the next-half intensity/amplitude (which is equal to $m = \frac{1}{4}$) is lower.

With the assumptions made, from Figure 2.9, it is observed that the detection probability as a function of SIR decreases as the degree of interference intensity (m) increases (for the symmetric assumption (i.e., $n = \frac{1}{2}$) and for a fixed probability of false alarm). Further, it is seen that as m increases, the optimum detector performance approaches the sub-optimum detector performance. Because, for $n = \frac{1}{2}$, as m increases, the interference intensity over the two half-widths of the square wave interference becomes equal, the equalization/whitening is not effective when compared to the large amplitude difference between the two half-widths of the square wave. Besides, at lower values of m, one finds a significant difference that the optimum detector brings with equalization/whitening compared to the sub-optimum one. Furthermore, it is observed that for SIR = 5 dB, the detection probabilities of the optimum detector with $m = \frac{1}{4}, \frac{2}{4}, \frac{3}{4}$ and for the sub-optimum detector are $0.8541, 0.6009, 0.4932$ and

0.4640, respectively.
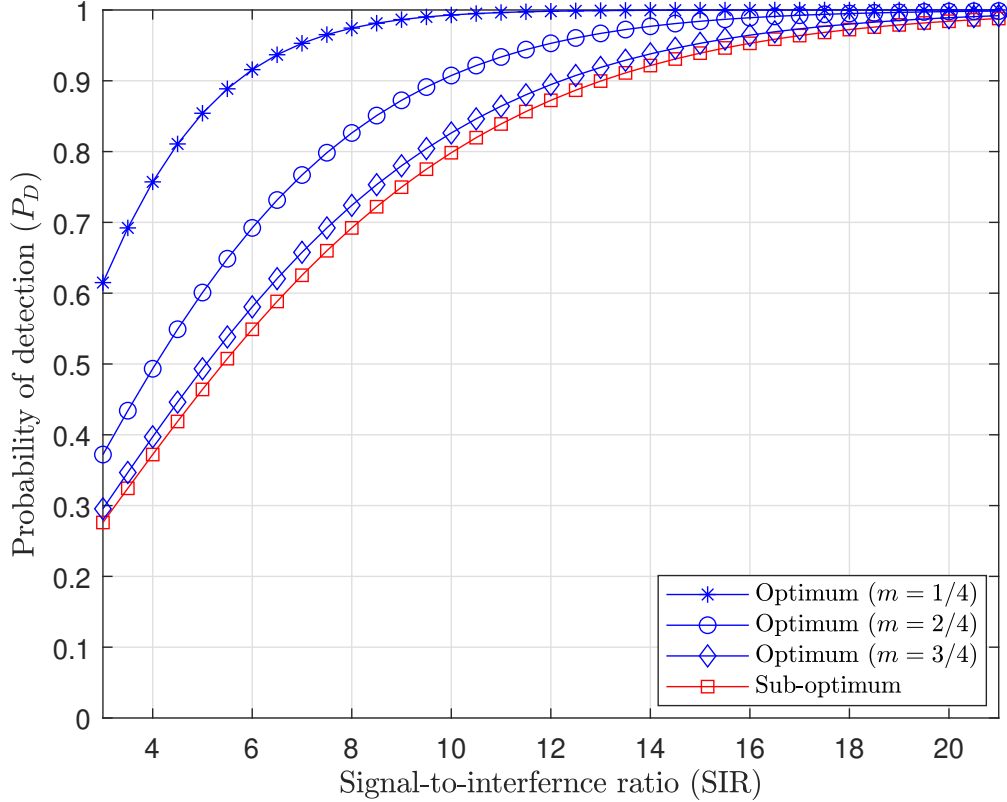
Figure 2.9: Receiver performance for the unrealistic deterministic case: Detection probability as a function of SIR with varying degrees of interference intensity (m).

Figure 2.10 shows the detection probability of the receiver for the unrealistic deterministic signal case as a function of SIR with varying degrees of non-stationarity/symmetry (n), fixed probability of false alarm $(P_{FA} = 10^{-2})$ and degree of interference intensity $\left(m = \frac{1}{2}\right)$ based on (2.39) and (2.40). It is observed that, for the assumed equal degree of interference intensity/amplitude $\left(\text{i.e., } m = \frac{1}{2}\right)$, as n increases, the detection probability as a function of SIR decreases and approaches that of the sub-optimum detector. As n increases, the optimum detector appears to relax the non-stationarity constraint and moves towards the assumption of stationary interference. It is also observed that for SIR $= 5$ dB, the detection probabilities for the optimum detector with $n = \frac{1}{4}, \frac{2}{4}, \frac{3}{4}$ and for the sub-optimum detector are $0.7903, 0.6009, 0.4860$ and 0.4640, respectively.

Figure 2.11 shows the receiver operating characteristic (ROC) curves for the un-
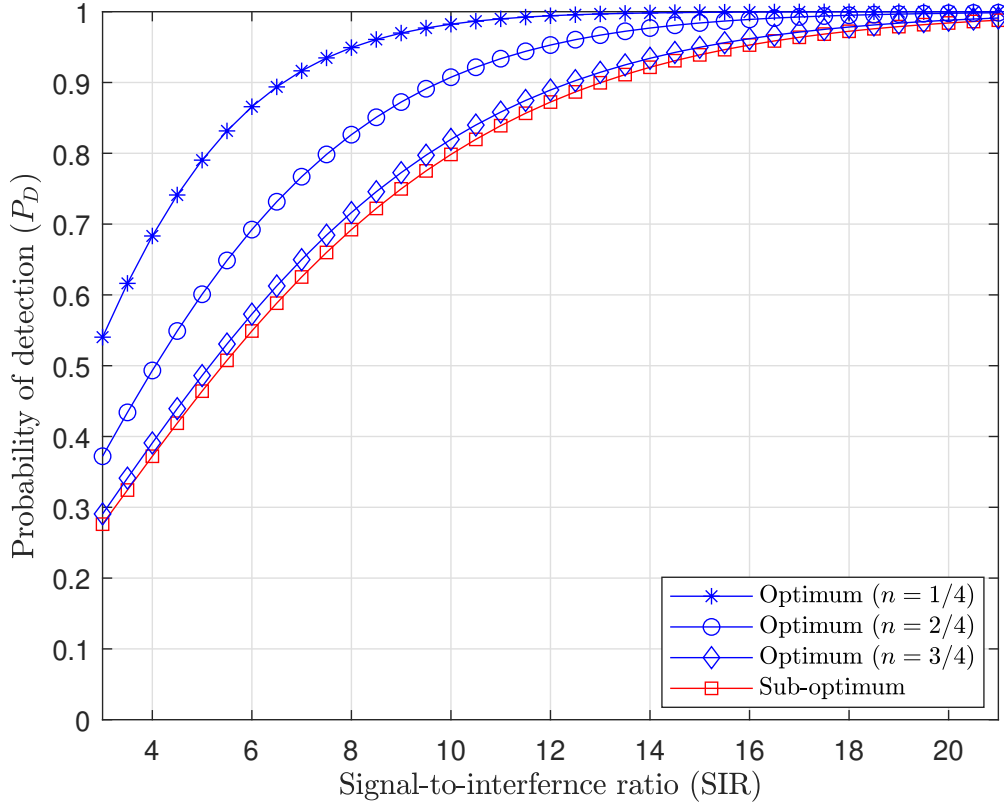
Figure 2.10: Receiver performance for the unrealistic deterministic signal case: Detection probability as a function of SIR with varying degrees of non-stationarity/symmetry (n).

realistic deterministic signals case with varying m, fixed SIR (5 dB) and $n = \frac{1}{2}$, based on (2.39) and (2.40). It is observed that, for the symmetric assumption $\left(\text{i.e., } n = \frac{1}{2}\right)$ and fixed SIR, the ROC curves trail one another, as the degree of interference intensity (m) increases. The reason for this is similar to the one that is presented in the observations of Figure 2.9. Further, it is observed that the optimum detector has a better probability of detection for some false alarm probability values, when compared to the sub-optimum one. Besides, it is also observed that for a false alarm probability of 0.05, the detection probability of the optimum detector with $m = \frac{1}{4}, \frac{2}{4}, \frac{3}{4}$ and for the sub-optimum detector is $0.9587, 0.8257, 0.7468$ and 0.7228, respectively.

Figure 2.12 shows the ROC curves for the unrealistic deterministic signals case with varying n, fixed SIR (5 dB) and $m = \frac{1}{2}$, based on (2.39) and (2.40). It is observed that, for the equal interference intensity/amplitude assumption $\left(\text{i.e., } m = \frac{1}{2}\right)$ and for fixed SIR, the ROC curves trail one another, as the degree of non-stationarity/symmetry (n) increases. Besides that, for a particular false alarm probability value, the optimum
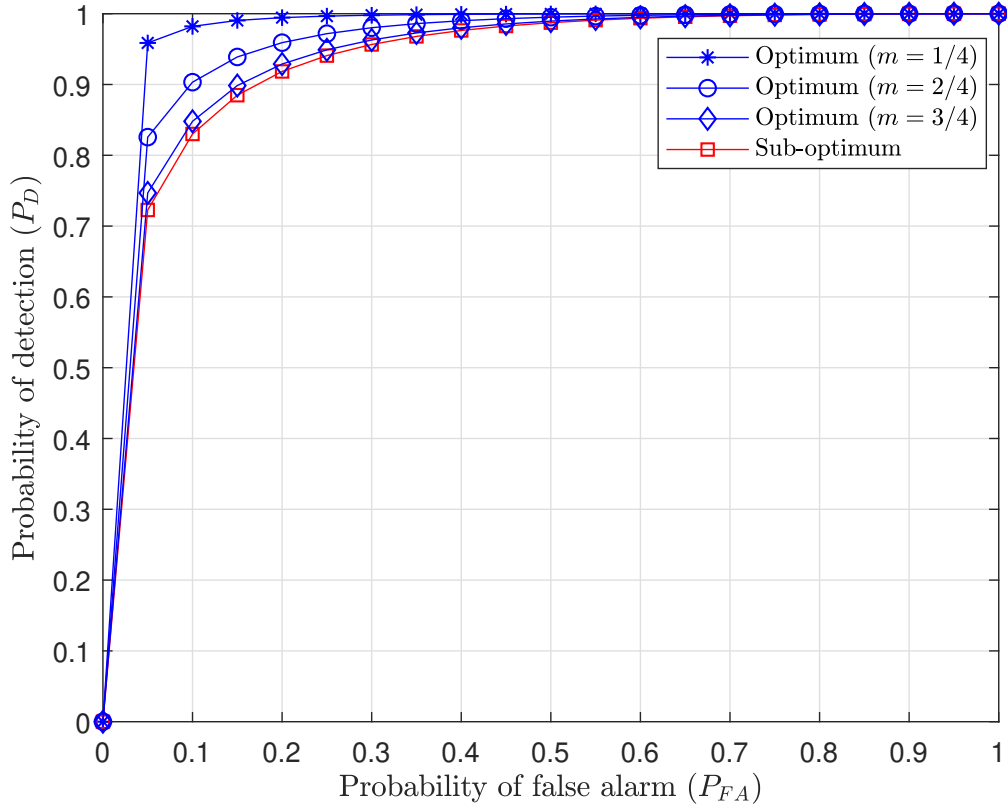
Figure 2.11: Receiver performance for the unrealistic deterministic signal case: Receiver operating characteristic (ROC) curves with varying degrees of interference intensity (m).

detector has a better probability of detection, when compared to the sub-optimum one. Further, it is also observed that for a false alarm probability of 0.05, the detection probabilities for the optimum detector with $n = \frac{1}{4}, \frac{2}{4}, \frac{3}{4}$ and the sub-optimum detector are $0.6320, 0.4953, 0.4224$ and 0.4088, respectively.

If there is missynchronization in the equalization/whitening stage, based on (2.52), (2.54) and (2.40), Figure 2.13 shows the detection probability of the receiver for the unrealistic deterministic signals case as a function of SIR with varying degrees of interference intensity (m), fixed probability of false alarm $(P_{FA} = 10^{-2})$ and degree of non-stationarity/symmetry $\left(n = \frac{1}{2}\right)$. It is observed that, for the lower values of m, where there is a significant difference in the interference intensity/amplitude between the two half-widths of the square wave interference, the performance of the missynchronized optimum detector is below that of the sub-optimum detector. It is also observed that as m increases, even though there is a missynchronization, the optimum detector is performing nearly equal or just above the sub-optimum detec-

40
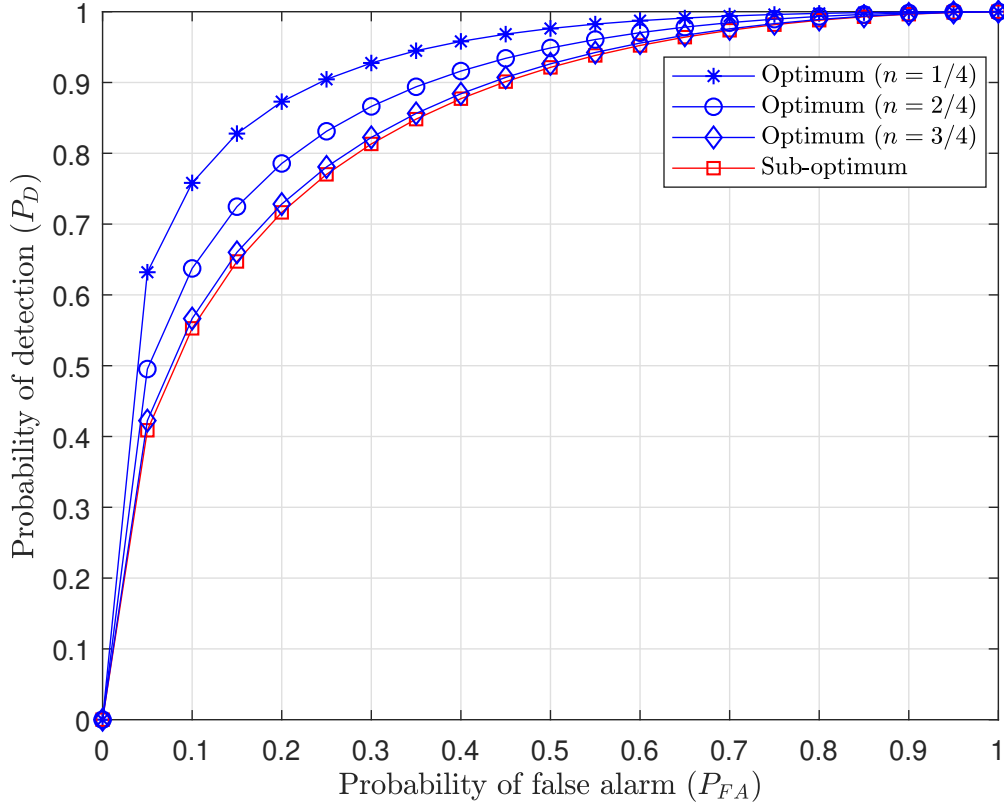
Figure 2.12: Receiver performance for the unrealistic deterministic signal case: Receiver operating characteristic (ROC) curves with varying degrees of non-stationarity/symmetry (n).

tor. It is because of the fact that, as m increases, the interference intensity becomes flat, the missynchronization does not impact much on the detection probability. Furthermore, it is observed that the worst-case 100% missynchronization performance is below the 50% missynchronization case. Moreover, it is observed that for SIR = 5 dB, the detection probabilities of the 100%, 50% missynchronized optimum detectors with $m = \frac{1}{4}, \frac{2}{4}, \frac{3}{4}$ and the sub-optimum detector are $0.1684, 0.2962,\ 0.2726, 0.3818,$ $0.4746, 0.4838$ and 0.4640, respectively. In addition, Figure 2.13 shows that for the same SIR and for $m = \frac{1}{2}$, when compared to perfect synchronization case (i.e., Figure 2.9), the performance of the 100% and 50% missynchronization case is reduced by approximately 54.6% and 36.5% respectively.

Based on (2.52), (2.54), and (2.40), Figure 2.14 shows the missynchronized receiver performance of the unrealistic deterministic signals case in terms of ROC curves, with varying m, fixed SIR (5 dB), and $n = \frac{1}{2}$. It is observed that, for the symmetric assumption (i.e., $n = \frac{1}{2}$), fixed SIR, and the ROC curves of the missynchronized optimum
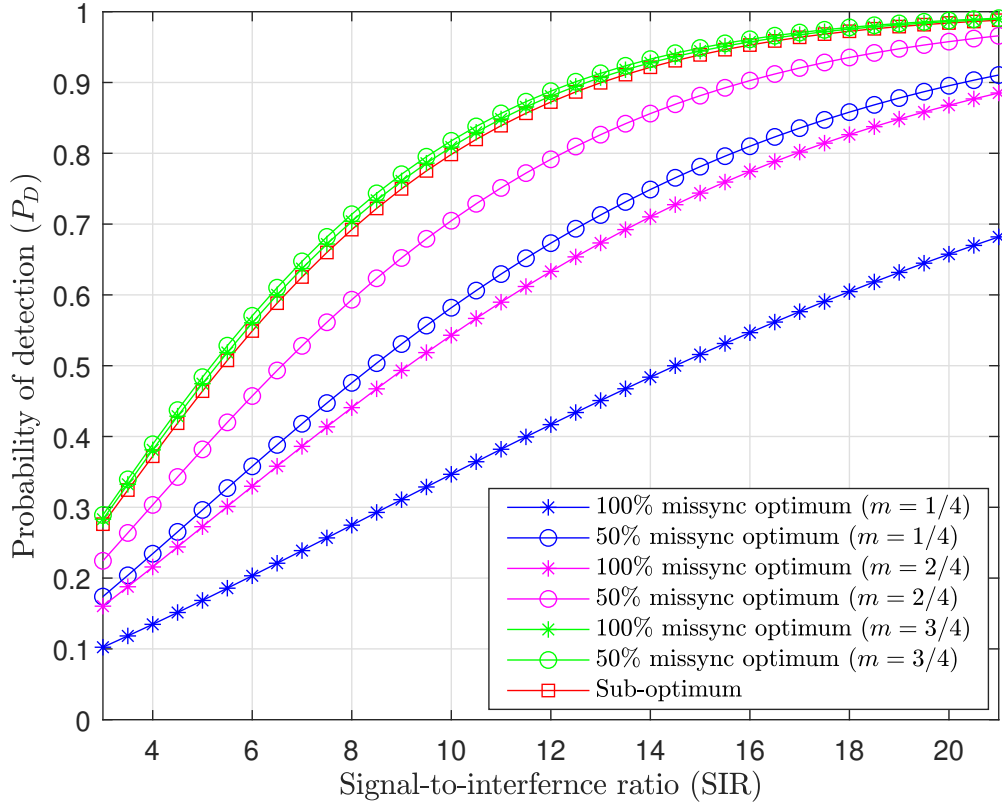
Figure 2.13: Receiver performance for the unrealistic deterministic signal case with missynchronization: Detection probability as a function of SIR with varying degrees of interference intensity (m).

detector are below the sub-optimum one at lower values of m and nearly equal or just above the sub-optimum one at higher values of m. Besides, the 100% missynchronization ROC curves are below the 50% missynchronization ROC curves, i.e., perfect (100%) missynchronization is always worse than imperfect (50%) missynchronization. Further, it is observed that for a false alarm probability of 0.05, the detection probabilities of the 100%, 50% missynchronized optimum detectors with $m = \frac{1}{4}, \frac{2}{4}, \frac{3}{4}$ and the sub-optimum detector is $0.3902, 0.5581, 0.5305, 0.6483, 0.7318, 0.7392$ and 0.7228, respectively.

For the moderately acceptable signals with random phase case (Section 2.2.2), based on (2.84) and (2.85), Figure 2.15 shows the detection probability of the receiver as a function of SIR with varying degrees of interference intensity (m), fixed probability of false alarm ($P_{FA} = 10^{-2}$) and degree of non-stationarity/symmetry $\left(n = \frac{1}{2}\right)$. Even in this case, for the symmetric assumption $\left(\text{i.e., } n = \frac{1}{2}\right)$ and the fixed probability of false alarm, the detection probability as a function of SIR decreases as the degree
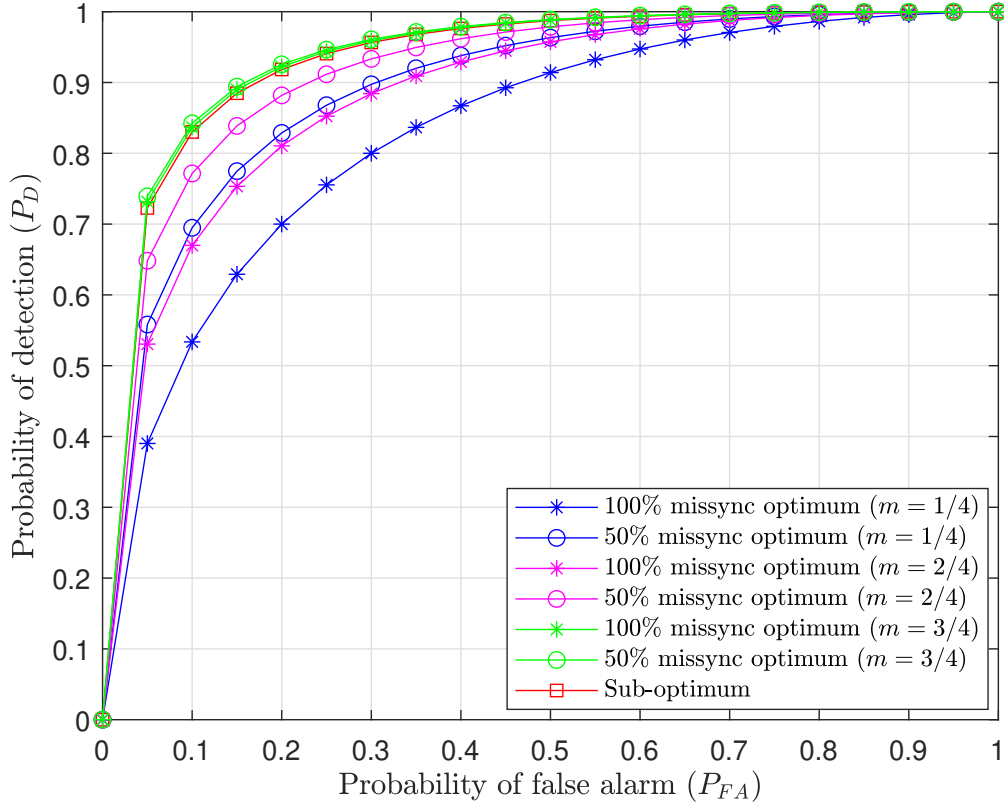
Figure 2.14: Receiver performance for the unrealistic deterministic signal case with missynchronization: Receiver operating characteristic (ROC) curves with varying degrees of interference intensity (m).

of interference intensity (m) increases. The significant difference in terms of detection probability that the optimum detector brings with the equalization/whitening effect is seen, when compared to the sub-optimum one. It is observed that for SIR $= 5$ dB, the detection probabilities for the optimum detector with $m = \frac{1}{4}, \frac{2}{4}, \frac{3}{4}$ and for the sub-optimum detector are $0.5267, 0.3633, 0.2934$ and 0.2734, respectively.

Figure 2.16 shows the receiver operating characteristic (ROC) curves for the moderately acceptable random phase signals, with varying m, fixed SIR (5 dB), and $n = \frac{1}{2}$, based on (2.84) and (2.85). It is observed that, with the symmetric assumption (i.e., $n = \frac{1}{2}$) and fixed SIR, the ROC curves trail one another as the degree of interference intensity (m) increases. In addition, the optimum detector has a better probability of detection for a particular false alarm probability when compared to the sub-optimum one. It is also observed that for a false alarm probability of 0.05, the detection probabilities of the optimum detector, with $m = \frac{1}{4}, \frac{2}{4}, \frac{3}{4}$ and the sub-optimum detector, are $0.75, 0.6027, 0.5271$, and 0.5037, respectively.
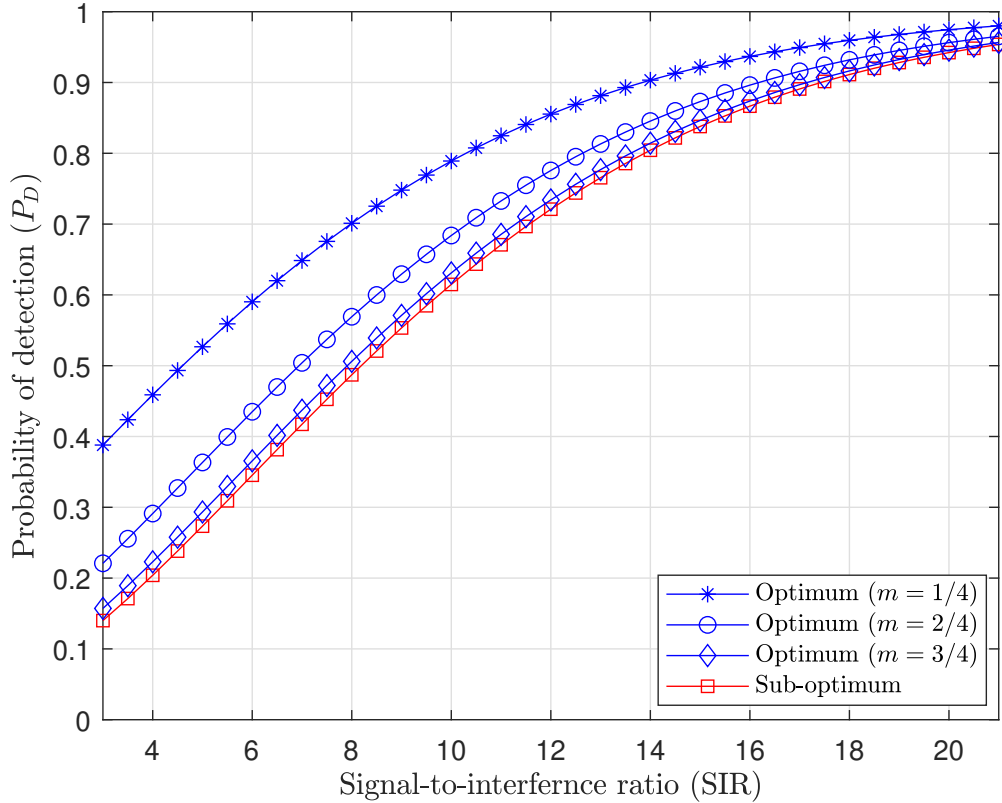
Figure 2.15: Receiver performance for the moderately acceptable random phase case: Detection probability as a function of SIR with varying degrees of interference intensity (m).

For the more realistic, completely random signals case, based on (2.101) and (2.104), Figure 2.17 shows detection probability of the receiver as a function of SIR, with varying degrees of interference intensity (m), fixed probability of false alarm $(P_{FA} = 10^{-2})$ and degree of non-stationarity/symmetry $\left(n = \frac{1}{2}\right)$. In Section 2.2.3, (2.101) and (2.104) indicate the performance for SIR as $\frac{E_1}{\langle s_{I_0}\rangle}$, rather than $\frac{2E_1}{\langle s_{I_0}\rangle}$. Nonetheless, for uniformity with the convention in Sections 2.2.1 and 2.2.2, this study continues to use the latter. From Figure 2.17, it is observed that, with the symmetric assumption $\left(\text{i.e., } n = \frac{1}{2}\right)$ and fixed probability of false alarm, the detection probability as a function of SIR decreases as the degree of interference intensity (m) increases. The significant difference that the optimum detector brings is seen with the equalization/whitening effect, when compared to the sub-optimum one, in terms of detection probability. Further, it is observed that for SIR $= 5$ dB, the detection probabilities of the optimum detector with $m = \frac{1}{4}, \frac{2}{4}, \frac{3}{4}$ and the sub-optimum detector are $0.5036, 0.3455, 0.2848$, and 0.2683, respectively.
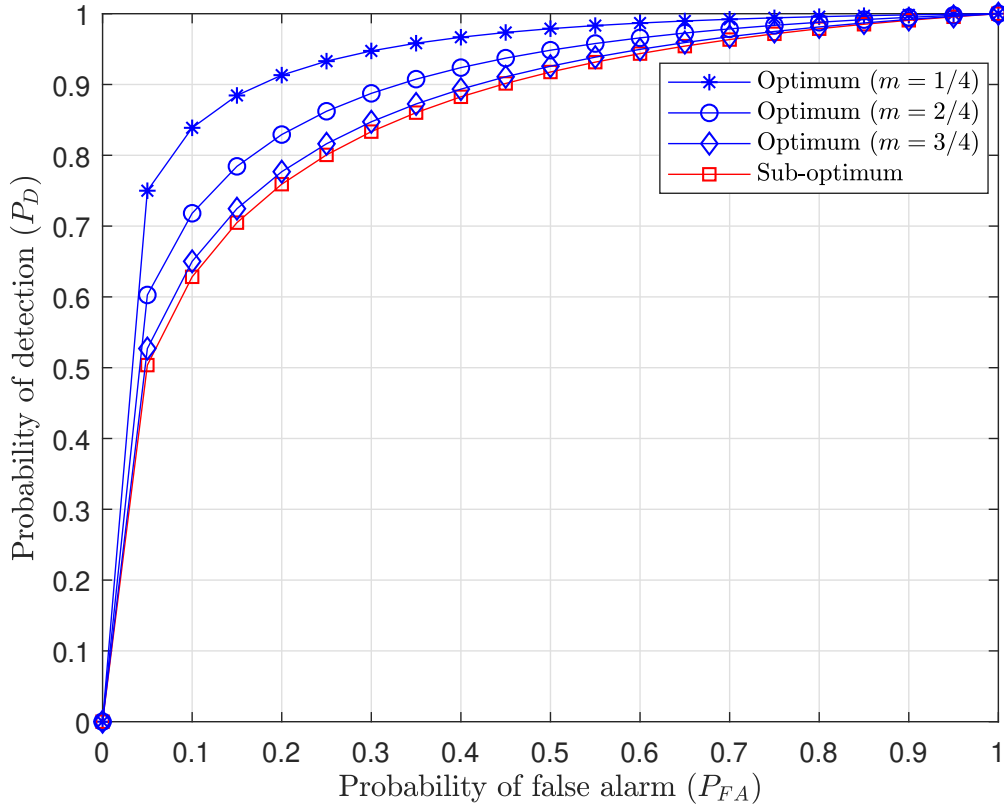
Figure 2.16: Receiver performance for the moderately acceptable random phase case: Receiver operating characteristic (ROC) curves with varying degrees of interference intensity (m).

Figure 2.18 shows ROC curves for the realistic completely random signals case with varying m, fixed SIR (5 dB) and $n = \frac{1}{2}$, based on (2.101) and (2.104). It is observed that, for the symmetric assumption $\left(\text{i.e., } n = \frac{1}{2}\right)$ and fixed SIR, the ROC curves fall behind one another, as the degree of interference intensity (m) increases. Further, it is observed that the optimum detector has a better probability of detection for a particular false alarm probability, when compared to the sub-optimum one. Furthermore, it is also observed that, for a false alarm probability of 0.05, the detection probabilities of the optimum detector with $m = \frac{1}{4}, \frac{2}{4}, \frac{3}{4}$ and the sub-optimum detector are $0.6401, 0.5009, 0.4471$, and 0.4249, respectively.

Table 2.1 shows the comparison of results of the three cases for a fixed SIR of 5dB, $P_{FA} = 10^{-2}$ and degree of cyclostationarity, degree of interference intensity of 0.5. The performance degradation is seen from the simplest deterministic case to the most realistic random signal case. This is because of the lack of information, as we move from the completely deterministic assumption to the completely random signal

45
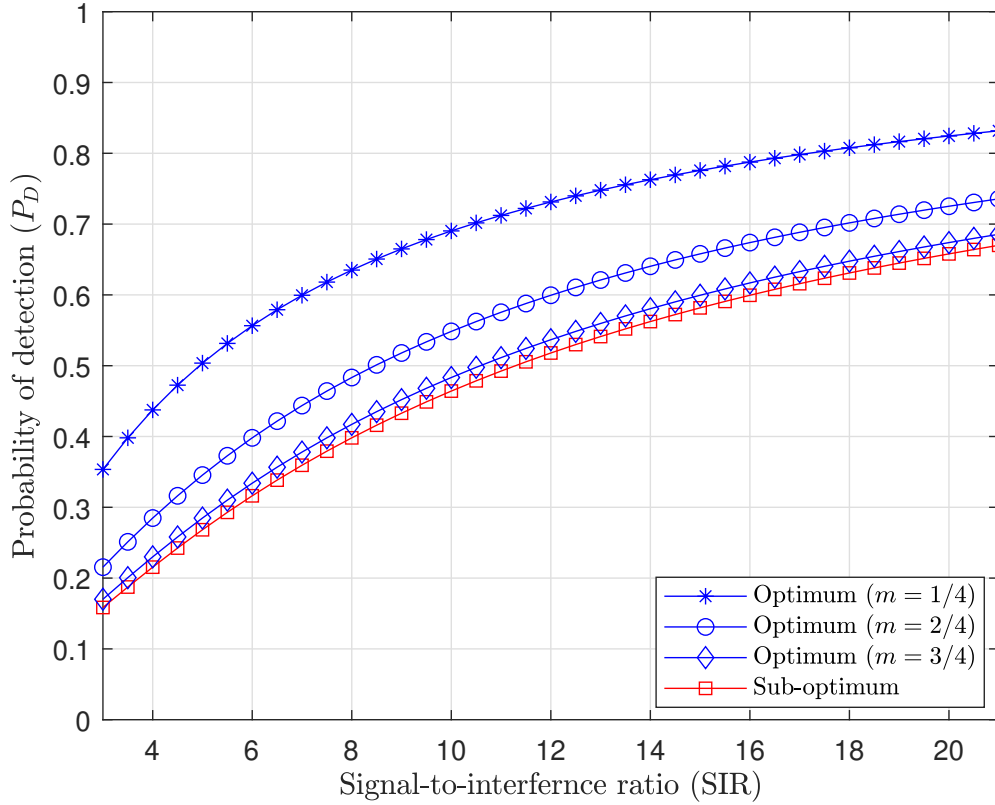
Figure 2.17: Receiver performance for the realistic random signal case: Detection probability as a function of SIR with varying degrees of interference intensity (m).

Table 2.1: Comparison of three cases for a fixed SIR = 5dB, $P_{FA} = 10^{-2}$ and $m = n = \frac{1}{2}$.

Case	Opti P_D	Sub-opti P_D
Sync Deterministic case	0.6009	0.4640
100% Missync Deterministic case	0.2726	0.4640
50% Missync Deterministic case	0.3818	0.4640
Signal with random phase	0.3633	0.2734
Completely random signal	0.3455	0.2683

assumption. Also, the optimal detector has better P_D than the sub-optimal one in all three cases. In contrast, the missynchronized detector performance falls behind the sub-optimal one. Therefore, improper equalization of interference may cost the performance degradation in the detection process.

Figure 2.19 shows the performance of the modified CFAR and NP detector with
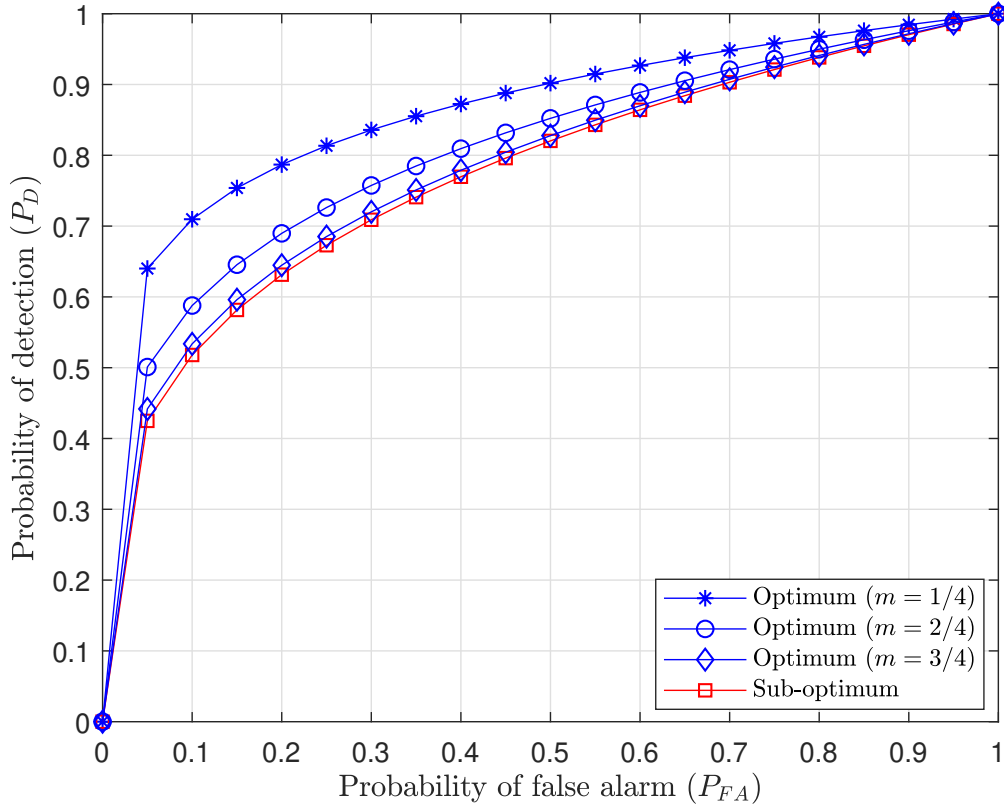
Figure 2.18: Receiver performance for the realistic random signal case: ROC curves with varying degrees of interference intensity (m).

varying degree of interference intensity and fixed $P_{FA} = 10^{-2}$. Also, it compares with standard CFAR and NP detectors, where the equalization to the in-band interference is ignored. The number of reference cells considered in CFAR is 16. These performance curves for modified CFAR and NP are based on (2.111) and (2.113). Whereas, for the standard CFAR and NP, the curves are plotted based on the same equations without considering the equalization (i.e., $a(t) = 1$, which inturn results $c = 1$). Figure 2.19 reveals that the proposed modified detectors (both CFAR, and NP) are outperforming the standard detectors for different interference intensity levels. For $m = 1/2$, where interference intensity is treated higher, with the proper equalization, the modified detectors have better P_D. As m increases, the interference intensity becomes flat, both modified and standard detectors have comparable performance. Further, it is noted that for a specific value of m, the CFAR (either modified or standard) performance falls behind the NP detector. It is because of the fact that the CFAR adapts the threshold for a small change in the interference and demands
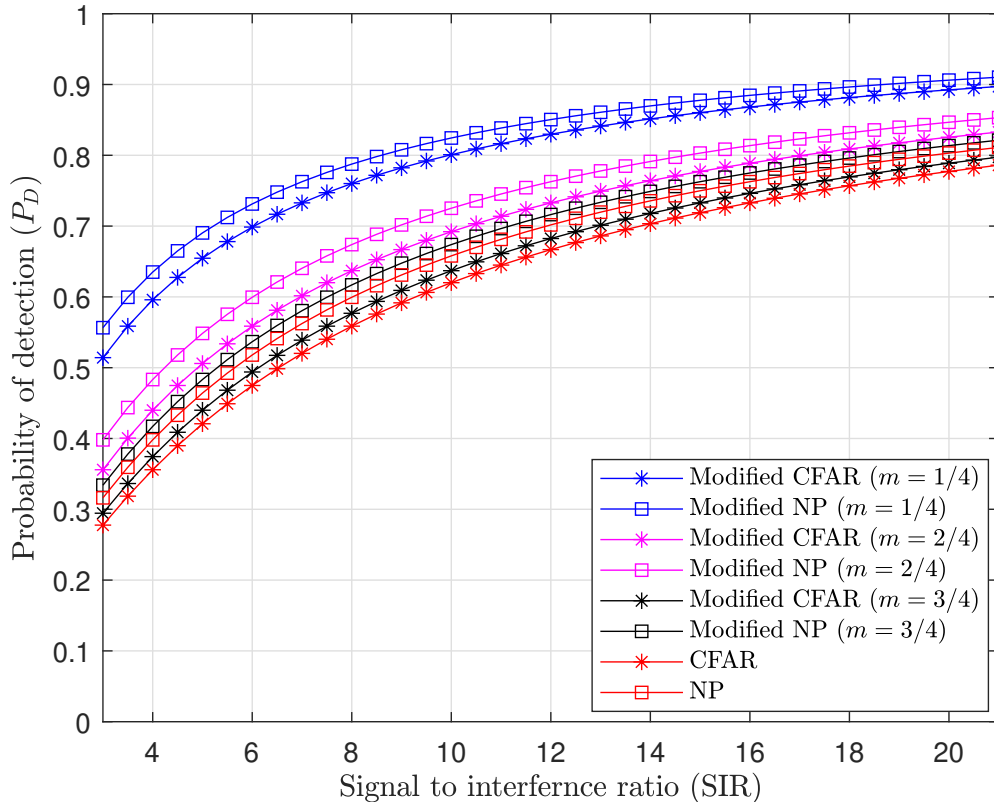
Figure 2.19: Modified CFAR and NP Receiver performance with varying degrees of interference intensity (m).

a higher SIR to get the same P_D as that of the NP detector. For a fixed P_D, the SIR difference between two curves is treated as CFAR SIR loss. The CFAR SIR loss can be improved by considering a large number of reference bins (i.e., with the increase in N) for threshold calculation.

A simple example is considered to evaluate the performance of the CFAR detector, with and without equalizer, by incorporating the in-band communication interference. A single target embedded in independent noise, with in-band interference having an average SINR of 12 dB, is examined. A data window of 1000 range cells is considered. It is assumed that the target is present at the 500th range cell. A CFAR detector is considered with 20 guard cells, 40 training cells, and a desired P_{FA} of 10^{-3}. The output of the CFAR detector without equalizer and with considering equalizer block is shown in Figure 2.20 and 2.21, respectively. In both the figures, the solid red line indicates the CFAR threshold, black dashed line indicates NP fixed threshold. Also, the Y-axis represents dB values. It is evident from Figure 2.20 that the standard CFAR
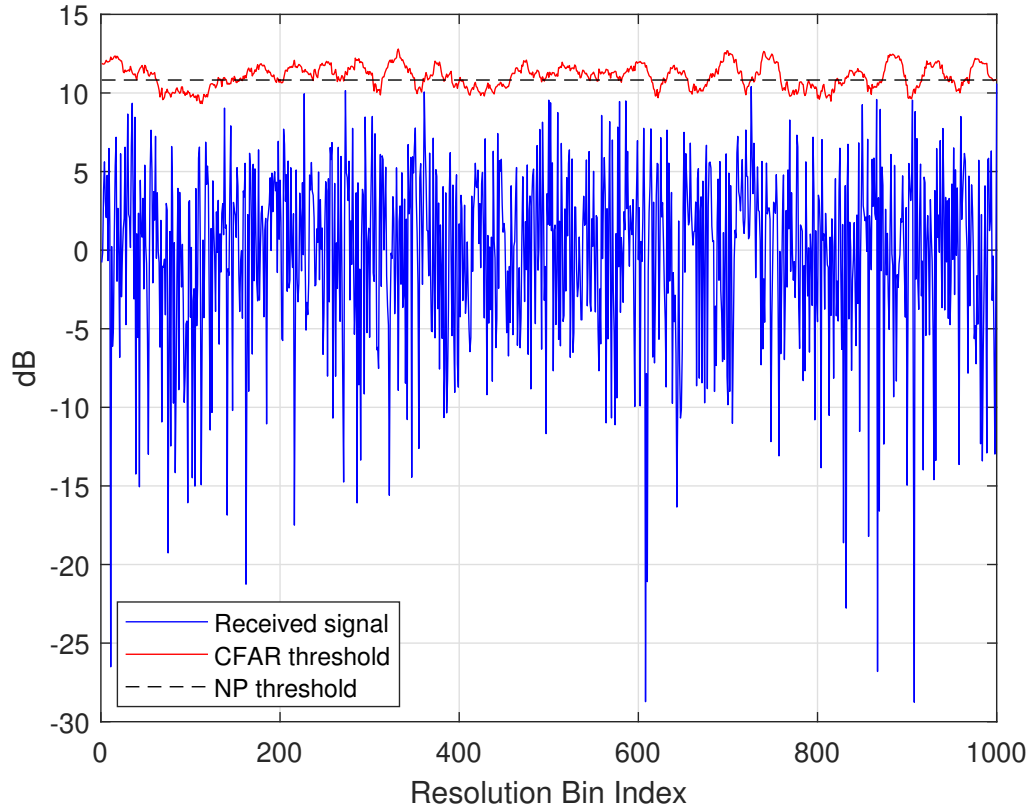
Figure 2.20: Standard CFAR output (without equalizing the in-band interference).

detector is unable to detect the target. On the other hand, Figure 2.21 illustrates the proposed modified CFAR is able to detect the presence of the target. This is because, in standard CFAR, the equalization to the interference is not performed; the in-band interference is present in all the cells. The CFAR calculates the threshold using the neighbouring cells to set a higher threshold that yields the target buried under interference. In contrast, in a modified CFAR detector, the received signal is first passed through the equalizer, which eliminates the in-band interference that provides the target detection. Furthermore, in both the Figures 2.20 and 2.21, for a given P_{FA}, the CFAR threshold is higher than the NP, indicating the higher SINR requirement, as a result of CFAR loss.
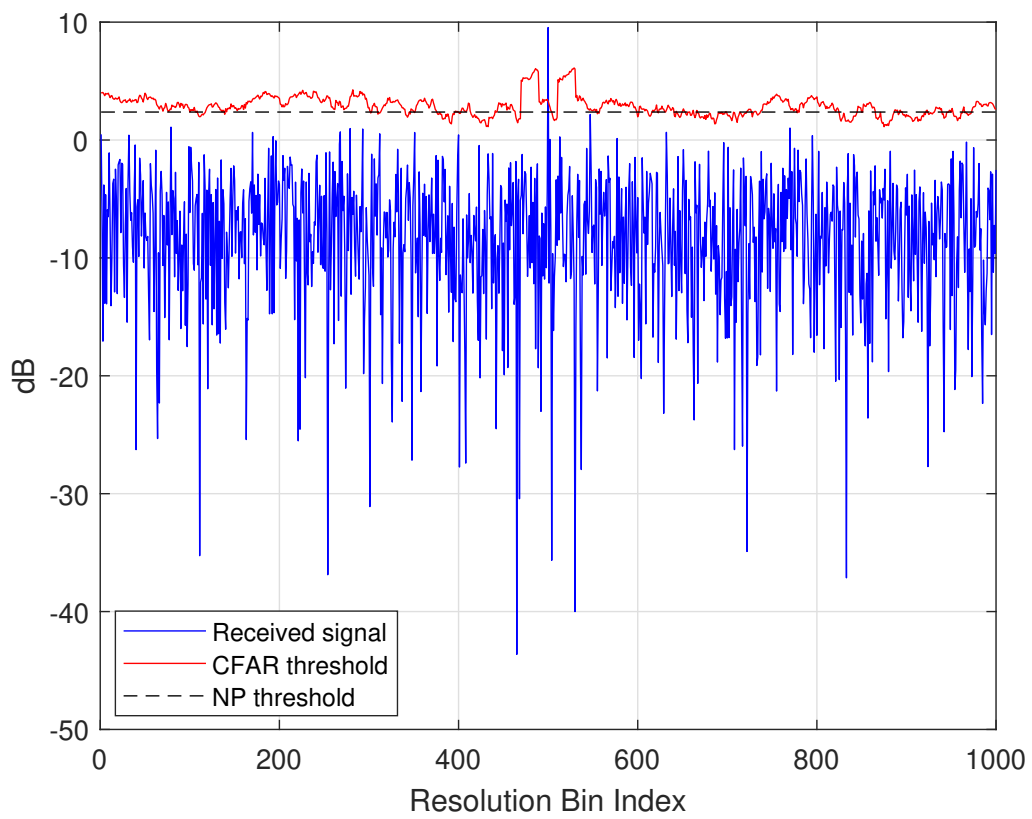
Figure 2.21: Modified CFAR output (equalizing the in-band interference).

Chapter 3

Tracking of Radar Targets with In-band Wireless Communication System Interference

In this Chapter, considering the distributed radars surrounded by multiple in-band wireless communication transmitters (IWCTs), a new measurement model is proposed. The new measurement model incorporates both radar returns and returns due to IWCTs. The tracking performance is evaluated using the global nearest neighbour (GNN) tracker with an extended Kalman filter (EKF) for the received measurement set. A large number of tracks are resulted due to IWCTs, and identifying the actual target track is ambiguous. The track-to-track association (T2TA) is performed to resolve the ambiguity and identify the true target track on multiple tracks produced owing to the presence of IWCTs. Once the true target tracks from each radar are identified, using the T2TA, the track-to-track fusion (T2TF) is carried out to improve the estimates of the true target. The results are quantified with position root mean square error (PRMSE) and the posterior Cramer–Rao lower bound (PCRLB). The simulation results reveal that the association and fusion of tracks from multiple radars identify the true target track with good accuracy. Further, the results disclose that, as the number of radars increases, the T2TA and fusion improved the PRMSE.

3.1   Problem formulation

A radar and communication system (RadComm) spectrum sharing scenario is considered, where N mono-static radars are present over a surveillance region to detect the radar targets and are surrounded by M in-band wireless communication trans-

mitters (IWCTs). The radar static locations are $\{\mathbf{x}_n^r\}_{n=1}^N$ and IWCTs locations are $\{\mathbf{x}_m^c\}_{m=1}^M$, as shown in Figure 3.1. Due to the in-band operation of IWCTs, the radar system receives the target echoes from both the mono-static emission and in-band transmitter emission. Also, it receives direct path signals from wireless transmitters. These two directions of signal reception are referred to as surveillance channels and reference channels. In Figure 3.1, the thick lines and dotted lines indicate surveillance and reference channels, respectively. Therefore, the received signal at the nth radar receiver, for a given target surrounded by M IWCTs, is given by

$$s_r^n(t) = \begin{cases} \sum_{n=1}^N s_{r_n}(t) + \sum_{m=1}^M s_{r_{c_m}}(t) + w(t) = s_{r_{sur_n}}(t) \\ \sum_{m=1}^M s_{r_{c_{d_m}}}(t) + w(t) = s_{r_{ref_n}}(t). \end{cases} \tag{3.1}$$

Here, $s_{r_n}(t)$ is the target return from n^{th} radar and $s_{r_{c_m}}(t)$ is the target echo from the mth surrounding communication system transmitter. In addition, $s_{r_{c_{d_m}}}(t)$ is the direct path signal from the surrounding m^{th} IWCT and $w(t)$ is the receiver noise. Further, $s_{r_{sur_n}}(t)$, $s_{r_{ref_n}}(t)$ are the received signals, received through surveillance and reference channel of the nth radar, respectively.
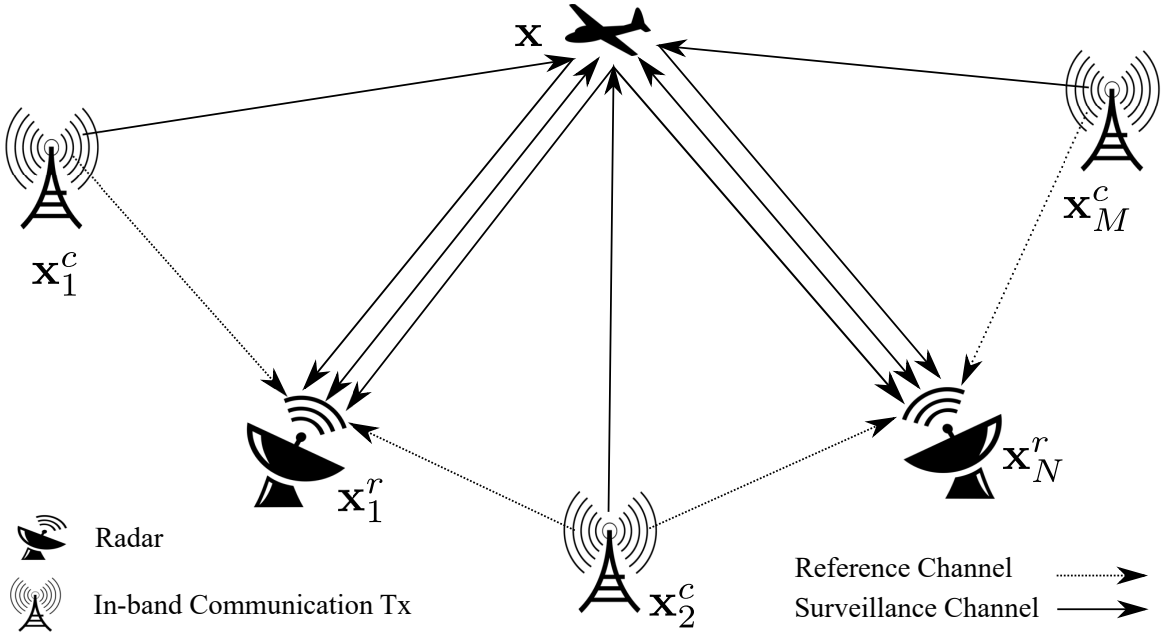
Figure 3.1: System model illustrating RadComm spectrum sharing scenario.

For simplicity, a single radar and a single in-band transmitter in a clean environment (unity target detection probability, zero false alarms) is assumed. The corre-
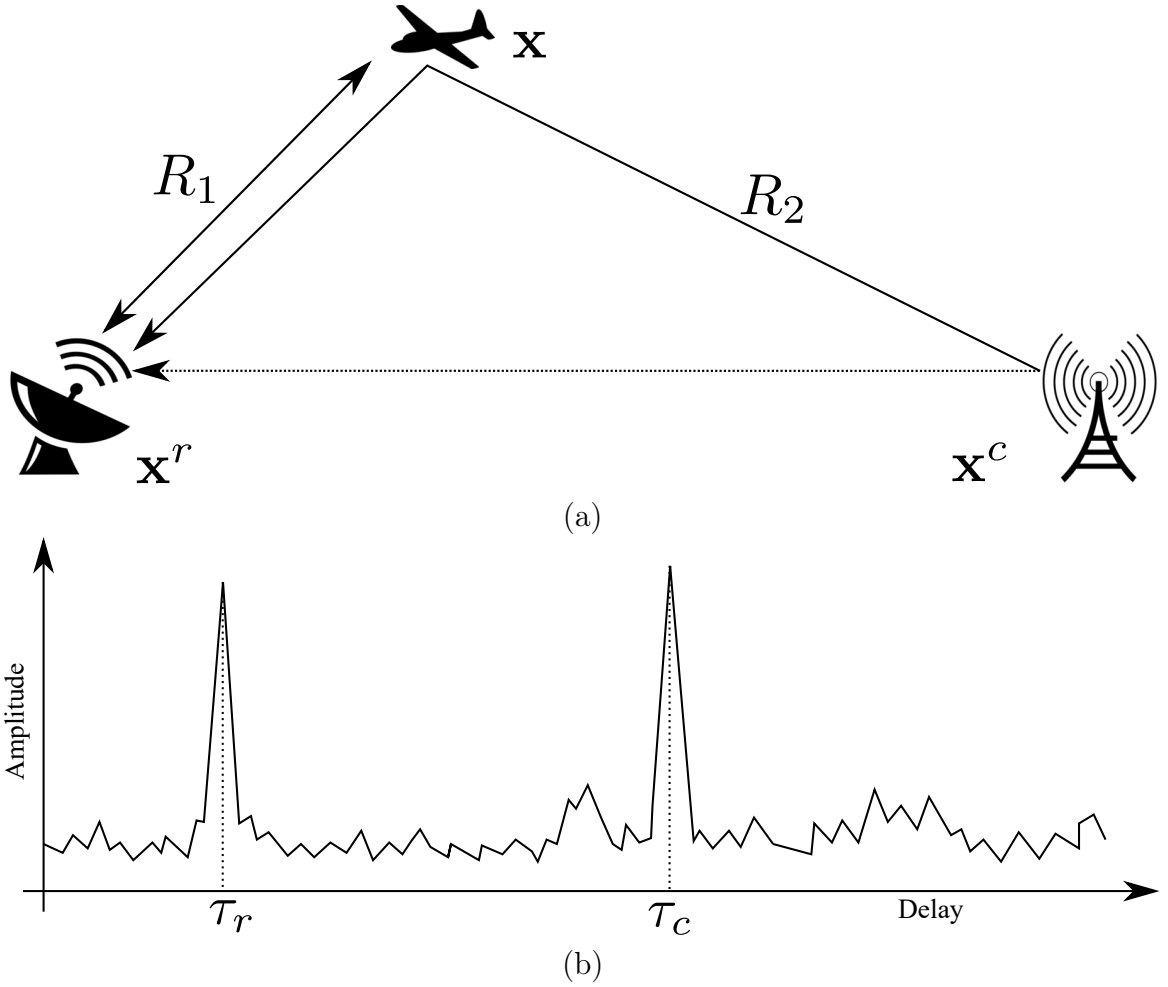
Figure 3.2: Reduced system model with single in-band transmitter and the corresponding correlator output.

sponding geometry is depicted in Figure 3.2a. The received signal is processed with matched filter-based receiver (Richards *et al.*, 2010). The correlator output at the receiver, depicts peaks at τ_r and τ_c, as shown in Figure 3.2b. This is because the radar receiver correlates the received signals with its own transmitted signal and the direct path reference signals received from IWCTs. The τ_r is the delay owing to the radar only return, and the corresponding range is given by $\frac{c\tau_r}{2}$. In contrast, τ_c is due to communication signal return. However, the radar assumes it as its own return (because of inadequate knowledge about the presence of IWCTs), and the corresponding range is calculated as $\frac{c\tau_c}{2}$. Here, c is the speed of light in free space. Hence, the presence of a single target and a single in-band transmitter in a given region results in two measurements at the radar receiver. As shown in Figure 3.2a, if R_1 is the distance from radar ($\mathbf{x}^r$) to a target ($\mathbf{x}$), R_2 is the distance between the in-band wireless

transmitter ($\mathbf{x}^c$) to target ($\mathbf{x}$), the τ_r and τ_c is given by

$$\begin{aligned}
\tau_r &= \frac{2R_1}{c} \quad \text{and} \\
\tau_c &= \frac{(R_1 + R_2)}{c},
\end{aligned} \tag{3.2}$$

respectively. It is assumed that radar also receives the bearing information, apart from the range information. However, the bearing information is the same for both cases because the direction of arrival of target returns are in the same direction.

Even though a single target is present in this scenario, the radar receives multiple measurements owing to IWCTs. Hence, there is a need to distinguish true target measurements from all the evolved measurements. This research proposes to analyse the target tracking performance for the above-stated problem.

3.2 Target tracking

This section briefly discusses the measurement model, state model, and GNN tracker for evaluating tracking performance in the RadComm spectrum sharing scenario. The radars work in distributed configuration and estimate the target kinematics using a local tracker. This section presents the tracking of nth radar. However, the subscript n has been removed for better reading and deriving the generalized mathematical model.

3.2.1 Measurement model

The measurement set received by the radar n at time k is

$$\mathbf{Z}(k) = \{\mathbf{z}_i(k)\}_{i=1}^{q_k} . \tag{3.3}$$

The measurement set obtained at k^{th} time instant contains q_k measurements, in which n_k measurements corresponds to mono-static radar, m_k measurements corresponds to IWCT, and e_k false alarms. i.e., $q_k = n_k + m_k + e_k$. In the given surveillance, the presence of $\{\mathbf{x}_l^t\}_{l=1}^L$ true targets, and $\{\mathbf{x}_m^c\}_{m=1}^M$ IWCTs result in $L + L \times M$ measurements at each radar. The measurement model is given by

$$\mathbf{z}_i(k) = h(\mathbf{x}(k)) + \mathbf{w}_i(k), \tag{3.4}$$

54

where $\mathbf{x}(\cdot)$ represents the state vector of the target at scan k, $h(\cdot)$ is a non-linear function to map the state space in Polar to the Cartesian state.

The measurements not only pertain to the target originated but also from the false alarms. These false alarms are independent and follow Poisson distribution (Bar-Shalom *et al.*, 2011), given by

$$\mathcal{P}(e) = \exp\left(-E\right)\frac{(E)^e}{e!}, \tag{3.5}$$

where E is the number of cells under consideration over a volume V. The spatial density of false alarm is given by

$$\lambda = \frac{E}{V}. \tag{3.6}$$

The probability of having q_k measurements in a given volume V is

$$p(q_k) = \begin{cases} (1 - p_D)\mathcal{P}(0); & q_k = 0, \\ (1 - p_D)\mathcal{P}(q_k) + p_D\mathcal{P}(q_k - 1); & q_k > 0, \end{cases} \tag{3.7}$$

where p_D is the target probability detection.

The measurements that originate at n^{th} mono-static radar, due to the presence of L targets, and M surrounding IWCTs, is represented as

$$\{\mathbf{z}_i(k)\}_{i=1}^{q_k} = \begin{cases} \begin{bmatrix} R_n^l + \mathcal{N}(0, \sigma_r^2) \\ \theta + \mathcal{N}(0, \sigma_\theta^2) \end{bmatrix}; & \begin{array}{c} l = 1, \cdots L; \\ \text{radar return} \end{array} \\ \begin{bmatrix} R_n^l + R_m^l + \mathcal{N}(0, \sigma_r^2) \\ \theta + \mathcal{N}(0, \sigma_\theta^2) \end{bmatrix}; & \begin{array}{c} l = 1, \cdots L, \\ m = 1. \cdots M; \\ \text{due to in-band Tx} \end{array} \\ e_k & ; \quad \text{false alarms} \end{cases} \tag{3.8}$$

Here, R_n^l is the Euclidean distance between radar location $\mathbf{x}_n^r$ and target location $\mathbf{x}_l^t$, and is given by

$$R_n^l = \sqrt{(x_n^r - x_l^t)^2 + (y_n^r - y_l^t)^2}. \tag{3.9}$$

Similarly, the R_m^l is the Euclidean distance between the target $\mathbf{x}_l^t$ and in-band wireless transmitter $\mathbf{x}_m^c$, is given by

$$R_m^l = \sqrt{(x_l^t - x_m^c)^2 + (y_l^t - y_m^c)^2}. \tag{3.10}$$

Here, θ is the same for radar and in-band returns because the direction of arrival of target returns are in the same direction. It is given by

$$\theta = \arctan\left(\frac{y_n^r - y_l^t}{x_n^r - x_l^t}\right). \tag{3.11}$$

The noise components in range and azimuth are mutually independent and follow the white Gaussian distribution with mean zero and standard deviation σ_r and σ_θ, respectively. The stacked vector of range and azimuth measurement noises is $\mathbf{w}(k)$ and its measurement noise covariance is given by

$$\mathbf{R}(k) = \mathbb{E}\{\mathbf{w}(k)\mathbf{w}(k)'\}. \tag{3.12}$$

3.2.2 State model

The state transition model follows additive white Gaussian noise (Bar-Shalom *et al.*, 2004) and is given by

$$\mathbf{x}(k+1) = \mathbf{F}(k)\mathbf{x}(k) + \mathbf{v}(k), \tag{3.13}$$

Here, $\mathbf{x}(k)$ is the four dimensional state vector constructed by stacking the position and velocity of the target as $[x(k), \dot{x}(k), y(k), \dot{y}(k)]'$, $\mathbf{v}(k)$ is a zero-mean white Gaussian process noise vector and its covariance matrix is

$$\mathbf{Q}(k) = \mathbb{E}[\mathbf{v}(k)\mathbf{v}(k)']. \tag{3.14}$$

The $\mathbf{F}(k)$ represents the state transition matrix; for the constant velocity (CV) model, the state transition is given by

$$\mathbf{F}(k) = \begin{bmatrix} 1 & t_s & 0 & 0 \\ 0 & 1 & 0 & 0 \\ 0 & 0 & 1 & t_s \\ 0 & 0 & 0 & 1 \end{bmatrix}, \tag{3.15}$$

where t_s is a sampling time.

Since the focus of this work is on evaluating the target tracking performance in the presence IWCTs, a simple CV model is considered to define the motion of a target.

3.2.3 Filtering

The EKF is used as a filtering algorithm. The filter involves three main steps, namely predictions, gain calculation, and updation. The predicted state and covariance are given by (Bar-Shalom *et al.*, 2004)

$$\hat{\mathbf{x}}(k+1|k) = \mathbf{F}\hat{\mathbf{x}}(k|k) \quad \text{and} \tag{3.16}$$

$$\mathbf{P}(k+1|k) = \mathbf{F}\mathbf{P}(k|k)\mathbf{F}' + \mathbf{Q}(k), \tag{3.17}$$

respectively. The measurement prediction is represented as

$$\hat{\mathbf{z}}(k+1) = \mathbf{H}\hat{\mathbf{x}}(k+1|k). \tag{3.18}$$

Here, $\mathbf{H}$ is a linearized form of measurement transition matrix and is given by

$$\mathbf{H} \approx \left[\begin{array}{cccc} \frac{\partial r}{\partial x} & \frac{\partial r}{\partial \dot{x}} & \frac{\partial r}{\partial y} & \frac{\partial r}{\partial \dot{y}} \\ \frac{\partial \theta}{\partial x} & \frac{\partial \theta}{\partial \dot{x}} & \frac{\partial \theta}{\partial y} & \frac{\partial \theta}{\partial \dot{y}} \end{array} \right]. \tag{3.19}$$

The innovation is given by

$$\gamma = \mathbf{z}(k+1) - \hat{\mathbf{z}}(k+1|k), \tag{3.20}$$

where $\hat{\mathbf{z}}(k+1|k)$ is determined by the data association module.

The Kalman gain $\mathbf{K}$ is computed as

$$\begin{aligned} \mathbf{K}(k+1) =& \mathbf{P}(k+1/k)\mathbf{H}(k+1)' \\ & [\mathbf{H}(k+1)\mathbf{P}(k+1/k)\mathbf{H}(k+1)' + \mathbf{R}]^{-1}, \end{aligned} \tag{3.21}$$

where $\mathbf{R}$ is the measurement covariance matrix.

The updated state and covariance are given by

$$\hat{\mathbf{x}}(k+1|k+1) = \hat{\mathbf{x}}(k+1|k) + \mathbf{K}(k+1)\gamma(k+1) \quad \text{and} \tag{3.22}$$

$$\mathbf{P}(k+1|k+1) = \mathbf{P}(k+1|k) - \mathbf{K}(k+1)\mathbf{H}(k+1)\mathbf{K}'(k+1) \tag{3.23}$$

respectively.

3.2.4 Data association

The data association makes the decision to associate the obtained measurements at k to the established tracks at $k-1$ and update the track at k. GNN is a 2D assignment that matches the q_k measurement list to the predicted T_{k-1} tracks list by formulating the global optimization problem. The optimization minimizes the overall cost ($\mathcal{C}$) of the measurement-to-track as

$$\mathcal{C} = \sum_{i=0}^{q_k} \sum_{t=0}^{T_{k-1}} a(i,t)c(i,t) \tag{3.24}$$

subjected to

$$\sum_{i=0}^{q_k} a(i,t)c(i,t) = 1, \quad t = 1, 2, \cdots T_{k-1}$$

$$\sum_{t=0}^{T_{k-1}} a(i,t)c(i,t) = 1, \quad i = 1, 2, \cdots q_k$$

The $a(i,t)$ is a binary assignment variable such that

$$a(i,t) = \begin{cases} 1; & \text{measurement } i \text{ associated with target } t \\ 0; & \text{otherwise} \end{cases} \tag{3.25}$$

Here, all the measurements are indexed in i, and all the tracks are indexed in t to form a 2D matrix. Whereas, $c(i,t)$ is the cost of associating the measurement i to track t; which is equal to the distance between predicted measurement $\mathbf{H}\hat{\mathbf{x}}(k+1|k)$ and measurement $\mathbf{z}_i(k+1)$. The above optimization is solved using the Munkres algorithm (Bourgeois and Lassalle, 1971).

3.2.5 Track management

Total available tracks are classified into tentative tracks and confirmed tracks. Tentative tracks are the ones that have fewer measurements associated, than the required number of measurements, over a specified time limit. In contrast, confirmed tracks are the tentative tracks that receive more associated measurements and are promoted to be confirmed ones. Also, if an inadequate number of measurements are associated with the tentative track within the specified time, the tentative tracks are deleted. For track maintenance, the logic-based rule (Jiang *et al.*, 2014) is used, given by

1. For track initialization: out of the last N_{init} measurement frames, if at least M_{init} measurements are associated together, then form a track and mark it tentative; otherwise, do nothing.

2. For a tentative track: out of the last N_{tent} measurement frames, if at least M_{tent} measurements are associated to the track, then promote it as confirmed; otherwise, delete the track.

3. For a confirmed track: out of the last N_{conf} measurement frames, if at least M_{conf} measurements are associated to the track, then do nothing; otherwise, delete it.

3.3 Track-to-track association and fusion

The presence of IWCTs produces more tracks at the radar receiver, even though a single target is present in the surveillance region. More than one radar present in the same surveillance region is to be considered to determine the actual target track. Once the tracks are received from all radars, track-to-track association and fusion of tracks are required to identify the true track precisely. Accordingly, this section presents the track-to-track association and track fusion concepts for the generalized scenario, where N number of radars are looking for a target in a surveillance region surrounded by M IWCTs.

3.3.1 Track-to-track association (T2TA)

The N radars have their own number of tracks in the form of target estimate $\hat{\mathbf{x}}_i^{\xi_i}$, with their errors are distributed as zero-mean Gaussian with covariance $\mathbf{P}_i^{\xi_i}$. The $i = 1, 2, \ldots, N$, represents radar number and $\xi_i = 0, 1, 2, \ldots, T_i$ represents number of tracks that the each radar generates. To find out the tracks corresponds to the same target, it is required to perform the likelihood ratio test, given by

$$\chi(\mathcal{H}^1_{\xi_1,\xi_2,\ldots,\xi_N} : \mathcal{H}^0_{\xi_1,\xi_2,\ldots,\xi_N}) = \frac{\Lambda(\mathcal{H}^1_{\xi_1,\xi_2,\ldots,\xi_N})}{\Lambda(\mathcal{H}^0_{\xi_1,\xi_2,\ldots,\xi_N})}, \tag{3.26}$$

where $\Lambda(\mathcal{H}^1_{\xi_1,\xi_2,\ldots,\xi_N})$ represents the likelihood hypothesis of tracks that have common origin, $\Lambda(\mathcal{H}^0_{\xi_1,\xi_2,\ldots,\xi_N})$ represents the likelihood hypothesis of tracks that have different origin.

Calculating the likelihood hypothesis of tracks that have a common origin is as follows

$$\Lambda(\mathcal{H}^1_{\xi_1,\xi_2,\ldots,\xi_N}) = p(\hat{\mathbf{x}}_N^{\xi_N}, \ldots, \hat{\mathbf{x}}_1^{\xi_1} | \mathcal{H}^1_{\xi_1,\xi_2,\ldots,\xi_N}). \tag{3.27}$$

The (3.27) is also be written, conditioned on the track estimate of the first radar, given by

$$\Lambda(\mathcal{H}^1_{\xi_1,\xi_2,\ldots,\xi_N}) = p(\hat{\mathbf{x}}_N^{\xi_N}, \ldots, \hat{\mathbf{x}}_2^{\xi_2} | \mathcal{H}^1, \hat{\mathbf{x}}_1^{\xi_1}) p(\hat{\mathbf{x}}_1^{\xi_1} | \mathcal{H}^1). \tag{3.28}$$

The $p(\hat{\mathbf{x}}_1^{\xi_1} | \mathcal{H}^1)$ is independent of $\mathcal{H}^1_{\xi_1,\xi_2,\ldots,\xi_N}$, hence it can be relaxed. Also, it is assumed to be a uniform distribution, which is a valid assumption in the case of a lack of information. i.e.,

$$p(\hat{\mathbf{x}}_1^{\xi_1} | \mathcal{H}^1_{\xi_1,\xi_2,\ldots,\xi_N}) = p(\hat{\mathbf{x}}_1^{\xi_1}) = \frac{1}{C}. \tag{3.29}$$

Substituting (3.29) into (3.28) results

$$\Lambda(\mathcal{H}^1_{\xi_1,\xi_2,\ldots,\xi_N}) = \frac{1}{C}p(\hat{\mathbf{x}}^{\xi_N}_N,\ldots,\hat{\mathbf{x}}^{\xi_2}_2|\mathcal{H}^1,\hat{\mathbf{x}}^{\xi_1}_1). \tag{3.30}$$

Consider the two radar (i,j) case that has two tracks (ξ_i,ξ_j) as common target origin. Under the Gaussian assumption, if the tracks $\hat{\mathbf{x}}^{\xi_i}_i$, $\hat{\mathbf{x}}^{\xi_j}_j$ at radar i, and radar j result from the same target, the likelihood function of the two tracks is given by (Bar-Shalom, 1981)

$$\Lambda(\mathcal{H}_{\xi_i,\xi_j}) = \frac{1}{C}\mathcal{N}(\hat{\mathbf{x}}^{\xi_i}_i - \hat{\mathbf{x}}^{\xi_j}_j;0,\mathbf{P}^{\xi_i}_i + \mathbf{P}^{\xi_j}_j - \mathbf{P}^{\xi_i,\xi_j}_{i,j} - (\mathbf{P}^{\xi_i,\xi_j}_{i,j})'), \tag{3.31}$$

where $\mathcal{N}(\mathbf{x};\bar{\mathbf{x}},\mathbf{P})$ represents Gaussian distribution of variable $\mathbf{x}$ with mean and covariance as $\bar{\mathbf{x}}$, $\mathbf{P}$, respectively.

Similar to (3.31), the generalized likelihood function of all the common tracks (zero error tracks) $\xi_1,\xi_2,\ldots,\xi_N$ for all N radars is defined as

$$\Lambda(\mathcal{H}^1_{\xi_1,\xi_2,\ldots,\xi_N}) = \frac{1}{C}\mathcal{N}(\hat{\mathbf{x}};0,P). \tag{3.32}$$

Here

$$\hat{\mathbf{x}} = \begin{bmatrix} \tilde{\mathbf{x}}_{21}, & \tilde{\mathbf{x}}_{31}, & \ldots, & \tilde{\mathbf{x}}_{N1} \end{bmatrix}', \tag{3.33}$$

where $\tilde{\mathbf{x}}_{ij}$ represents the difference of the estimates resulted from the same target at i^{th} and j^{th} radar, given by

$$\tilde{\mathbf{x}}_{ij} = \hat{\mathbf{x}}^{\xi_i}_i - \hat{\mathbf{x}}^{\xi_j}_j. \tag{3.34}$$

The diagonal elements of $\mathbf{P}$ are represented as

$$\begin{aligned} \mathbf{P}_{i-1,i-1} &= \mathbb{E}[\tilde{\mathbf{x}}_{i1}\tilde{\mathbf{x}}'_{i1}|\mathcal{H}^1_{\xi_1,\xi_2,\ldots,\xi_N}], \\ &= \mathbf{P}^{\xi_1}_1 + \mathbf{P}^{\xi_i}_i - \mathbf{P}^{\xi_1,\xi_i}_{1,i} - (\mathbf{P}^{\xi_1,\xi_i}_{1,i})' \quad i = 2,\ldots,N \end{aligned} \tag{3.35}$$

where $\tilde{\mathbf{x}}_{ij}$ is defined in (3.34).

Off-diagonal elements of $\mathbf{P}$ are given by

$$\begin{aligned} \mathbf{P}_{i-1,j-1} &= \mathbb{E}[\tilde{\mathbf{x}}_{i1}\tilde{\mathbf{x}}'_{j1}|\mathcal{H}^1_{\xi_1,\xi_2,\ldots,\xi_N}], \\ &= \mathbf{P}^{\xi_1}_1 - \mathbf{P}^{\xi_1,\xi_j}_{1,j} - (\mathbf{P}^{\xi_1,\xi_i}_{1,i})' + \mathbf{P}^{\xi_i,\xi_j}_{i,j}, \quad i,j = 2,\ldots,N \end{aligned} \tag{3.36}$$

Similar to (3.32), the likelihood hypothesis of tracks having different origins follows the same procedure as above, specified as

$$\begin{aligned} \Lambda(\mathcal{H}^0_{\xi_1,\xi_2,\ldots,\xi_N}) &= p(\hat{\mathbf{x}}^{\xi_N}_N,\ldots,\hat{\mathbf{x}}^{\xi_2}_2|\mathcal{H}^0,\hat{\mathbf{x}}^{\xi_1}_1)p(\hat{\mathbf{x}}^{\xi_1}_1|\mathcal{H}^0) \\ &= \prod_{i=2}^N p(\hat{\mathbf{x}}^{\xi_i}_i|\mathcal{H}^0,\hat{\mathbf{x}}^{\xi_1}_1)p(\hat{\mathbf{x}}^{\xi_1}_1|\mathcal{H}^0) \end{aligned} \tag{3.37}$$

Similar to (3.29), the $p(\hat{\mathbf{x}}_1^{\xi_1}|\mathcal{H}_{\xi_1,\xi_2,\dots,\xi_N}^0)$ is assumed to be diffuse prior, given by

$$p(\hat{\mathbf{x}}_1^{\xi_1}|\mathcal{H}_{\xi_1,\xi_2,\dots,\xi_N}^0) = p(\hat{\mathbf{x}}_1^{\xi_1}) = \frac{1}{C}, \tag{3.38}$$

whereas, $p(\hat{\mathbf{x}}_N^{\xi_N},\dots,\hat{\mathbf{x}}_2^{\xi_2}|\mathcal{H}^0,\hat{\mathbf{x}}_1^{\xi_1})$ is assumed to follow Poisson distribution in the state space, with a spatial density λ (Bar-Shalom *et al.*, 2011). Therefore, substituting (3.38) into (3.37) yields

$$\Lambda(\mathcal{H}_{\xi_1,\xi_2,\dots,\xi_N}^0) = \frac{1}{C}\lambda^{N-1}. \tag{3.39}$$

Finally, from (3.26), (3.32), (3.39), the likelihood ratio test is given by

$$\chi(\mathcal{H}_{\xi_1,\xi_2,\dots,\xi_N}^1 : \mathcal{H}_{\xi_1,\xi_2,\dots,\xi_N}^0) = \frac{\mathcal{N}(\hat{\mathbf{x}};0,\mathbf{P})}{\lambda^{N-1}}, \tag{3.40}$$

For T2TA, the track-to-track assignment algorithm of assigning the ξ_i tracks that result from N radars representing the same target is defined. For this, the binary assignment variable is defined as

$$\psi_{\xi_1,\xi_2,\dots,\xi_N} = \begin{cases} 1; & \text{tracks } \xi_1,\xi_2,\dots,\xi_N \text{ from same target} \\ 0; & \text{from different target} \end{cases} \tag{3.41}$$

The multidimensional (S-D) track-to-track assignment algorithm of finding the most likely hypothesis is the result of the constrained optimization problem given below

$$\min_{\psi_{\xi_1,\xi_2,\dots,\xi_N}} \sum_{\xi_1=0}^{T_1}\sum_{\xi_2=0}^{T_2}\cdots\sum_{\xi_N=0}^{T_N} c_{\xi_1,\xi_2,\dots,\xi_N}\psi_{\xi_1,\xi_2,\dots,\xi_N} \tag{3.42}$$

subject to

$$\sum_{\xi_2=0}^{T_2}\cdots\sum_{\xi_N=0}^{T_N}\psi_{\xi_1,\xi_2,\dots,\xi_N} = 1, \quad \xi_1 = 1,2,\dots,T_1$$

$$\sum_{\xi_1=0}^{T_1}\sum_{\xi_3=0}^{T_3}\cdots\sum_{\xi_N=0}^{T_N}\psi_{\xi_1,\xi_2,\xi_3,\dots,\xi_N} = 1, \quad \xi_2 = 1,2,\dots,T_2$$

$$\vdots$$

$$\sum_{\xi_1=0}^{T_1}\cdots\sum_{\xi_{N-1}=0}^{T_{N-1}}\psi_{\xi_1,\dots,\xi_{N-1},\xi_N} = 1, \quad \xi_N = 1,2,\dots,T_N \tag{3.43}$$

and

$$\psi_{\xi_1,\dots,\xi_N} \in \{0,1\},$$

$$\xi_1 = 0,1,\dots,T_1,$$

$$\vdots$$

$$\xi_N = 0,1,\dots,T_N \tag{3.44}$$

The cost function $c_{\xi_1,\xi_2,\ldots,\xi_N}$ in (3.42) is calculated as

$$c_{\xi_1,\xi_2,\ldots,\xi_N} = -\ln \chi(\mathcal{H}^1 : \mathcal{H}^0). \tag{3.45}$$

where $\chi(\mathcal{H}^1 : \mathcal{H}^0)$ is the likelihood ratio, given in (3.40).

3.3.2 Correlation free fusion

This subsection considers the covariance intersection (CI) method for track-to-track fusion (T2TF). As it is a memoryless algorithm, cross-covariance among the local tracks is not utilized. Two algorithms are considered in the CI method; one is the original CI algorithm, and the other is sampling CI (SCI). The SCI is considered; because of its computational feasibility in fusing the more number of tracks.

A Original covariance intersection (CI) algorithm

Suppose the T2TA algorithm reveals T_N independent tracks of N radars representing the same target, which needs to be fused, the approximate CI of those N non-Gaussian uncertainties is given by (Tian *et al.*, 2010)

$$\mathbf{P}_{CI}^{-1} = \omega_{T_1}\mathbf{P}_{T_1}^{-1} + \omega_{T_2}\mathbf{P}_{T_2}^{-1} + \ldots + \omega_{T_N}\mathbf{P}_{T_N}^{-1}, \quad 0 \leq \omega_{T_i} \leq 1 \text{ and } \sum_{T_i=1}^{N} \omega_{T_i} = 1. \tag{3.46}$$

The fused state estimate is represented as

$$\mathbf{P}_{CI}^{-1}\hat{\mathbf{x}}_{CI} = \omega_{T_1}\mathbf{P}_{T_1}^{-1}\hat{\mathbf{x}}_{T_1} + \omega_{T_2}\mathbf{P}_{T_2}^{-1}\hat{\mathbf{x}}_{T_2} + \ldots + \omega_{T_N}\mathbf{P}_{T_N}^{-1}\hat{\mathbf{x}}_{T_N}. \tag{3.47}$$

For the above (3.47), a closed form solution for lower dimensional matrix is presented in (Reinhardt *et al.*, 2012).

B Sampling covariance intersection (SCI) algorithm

The fused estimate, in the case of the SCI method of fusing the T_N independent tracks of N radars representing the same target, is given by (Tian *et al.*, 2010)

$$\mathbf{P}_0^{-1} = \sum_{T_i=1}^{N} \mathbf{P}_{T_i}^{-1}, \tag{3.48}$$

$$\hat{\mathbf{x}}_{SCI} = \mathbf{P}_0 \left(\sum_{T_i=1}^{N} \mathbf{P}_{T_i}^{-1}\hat{\mathbf{x}}_{T_i} \right). \tag{3.49}$$

To prevent the covariance becomes optimistic, the following procedure is used to adjust the size of the covariance matrix. The S number of random samples $\mathbf{x}_j = \mathcal{N}(0, \mathbf{P}_0), j = 1, \ldots, S$ are generated. Next, the r_{max} and r_{min} is found using

$$r_{\max} = \max_{j=1,2,\ldots,S} \frac{\mathbf{x}_j' \mathbf{P}_0^{-1} \mathbf{x}_j}{\max\limits_{T_i=1,2,\ldots,N} \hat{\mathbf{x}}_{T_i}' \mathbf{P}_i^{-1} \hat{\mathbf{x}}_{T_i}}, \tag{3.50}$$

$$r_{\min} = \min_{j=1,2,\ldots,S} \frac{\mathbf{x}_j' \mathbf{P}_0^{-1} \mathbf{x}_j}{\max\limits_{T_i=1,2,\ldots,N} \hat{\mathbf{x}}_{T_i}' \mathbf{P}_i^{-1} \hat{\mathbf{x}}_{T_i}}. \tag{3.51}$$

Finally, the fused covariance SCI is set as

$$\mathbf{P}_{SCI} = \frac{\mathbf{P}_0}{u r_{min} + (1-u) r_{max}}, \quad u \in [0, 1], \tag{3.52}$$

where u is used to adjust the performance of the SCI algorithm (Tian *et al.*, 2010).

3.4   Posterior Cramer-Rao Lower Bound (PCRLB)

In this section, to compare the simulation performance of the proposed framework, the Posterior Cramer-Rao Lower Bound (PCRLB) is considered. The PCRLB is the theoretical lower bound, which quantifies the estimation accuracy (Bar-Shalom *et al.*, 2011). Let $\hat{\mathbf{x}}_{k+1}$ be the estimate of the state vector $\mathbf{x}_{k+1}$ conditioned on measurement set $z_{1:k+1}$. The PCRLB (Tichavsky *et al.*, 1998) on the covariance $\mathbf{P}_{k+1}$ is the inverse of the Fisher information matrix (FIM) $\mathbf{J}_{k+1}$, given by

$$\mathbf{P}_{k+1} \triangleq \mathbb{E}\left[(\hat{\mathbf{x}}_{k+1} - \mathbf{x}_{k+1})(\hat{\mathbf{x}}_{k+1} - \mathbf{x}_{k+1})'\right] \geq \mathbf{J}_{k+1}^{-1}. \tag{3.53}$$

The FIM $\mathbf{J}_{k+1}$ is evaluated recursively by

$$\mathbf{J}_{k+1} = \mathbf{D}_k^{22} - \mathbf{D}_K^{21}(\mathbf{J}_k + \mathbf{D}_k^{11})^{-1}\mathbf{D}_k^{12}, \tag{3.54}$$

where

$$\mathbf{D}_k^{11} = \mathbf{F}_k' \mathbf{Q}_k^{-1} \mathbf{F}_k,$$

$$\mathbf{D}_k^{12} = \mathbf{D}_k^{21} = -\mathbf{F}_k' \mathbf{Q}_k^{-1},$$

$$\mathbf{D}_k^{22} = \mathbf{Q}_k^{-1} + \mathbf{J}_{z,k+1}. \tag{3.55}$$

Here, $\mathbf{J}_{z,k+1}$ corresponds to measurement contribution, given by (for brevity, subscript $k+1$ for $\mathbf{x}$ is omitted here):

$$\mathbf{J}_{z,k+1} = b(p_D, \lambda V, g) \left\{ [\nabla_{\mathbf{x}} h(\mathbf{x})]' \mathbf{R}_{k+1}^{-1} [\nabla_{\mathbf{x}} h(\mathbf{x})] \right\}, \tag{3.56}$$

where, $b(.)$ is the information reduction factor (IRF), accounting for the reduction of information due to false alarms and the measurements due to IWCTs in the available measurements. Which is a scalar quantity, depends on detection probability (p_D), false alarm density (λ), volume of the surveillance region (V), and gated volume (g). The expansion and the numerical evaluation of IRF is presented in (Hernandez *et al.*, 2006; Kirubarajan *et al.*, 2001; Meng *et al.*, 2009). The value of IRF $b(.)$ is approximately equal to p_D. The $\nabla_{\mathbf{x}} h(\mathbf{x})$ in (3.56) is the Jacobian matrix, given by

$$\nabla_{\mathbf{x}} h(\mathbf{x}) = \begin{pmatrix} \frac{(x_l^t - x_n^r)}{R_n^l} & 0 & \frac{(y_l^t - y_n^r)}{R_n^l} & 0 \\ \frac{-(y_l^t - y_n^r)}{(R_n^l)^2} & 0 & \frac{(x_l^t - x_n^r)}{(R_n^l)^2} & 0 \end{pmatrix},$$ (3.57)

where R_n^l is defined in (3.9).

Using matrix inversion Lemma, using (3.55), the FIM recursion (3.54) is deduced to

$$\mathbf{J}_{k+1} = \left[\mathbf{Q}_k + \mathbf{F}_k \mathbf{J}_k^{-1} \mathbf{F}_k' \right]^{-1} + \mathbf{J}_{z,k+1}.$$ (3.58)

The initial value of FIM is, $\mathbf{J}_0 = (\mathbf{P}_0)^{-1}$.

In this work, multiple radars (N) are used to identify the true target, and the information is fused to get a better estimate. So, to compare the estimation accuracy of the fused estimate, there is a need to calculate the fused FIM over the multiple radars. Therefore, the fused PCRLB follows (3.53) by replacing $\mathbf{J}$ with summation of all the FIMs from all the radars, given by

$$\mathbb{E}\left[(\hat{\mathbf{x}}_{k+1} - \mathbf{x}_{k+1})(\hat{\mathbf{x}}_{k+1} - \mathbf{x}_{k+1})' \right] \geq \left\{ \sum_{i=1}^{N} \mathbf{J}_{k+1}^i \right\}^{-1},$$ (3.59)

where $\mathbf{J}_{k+1}^{(.)}$ for each radar is given in (3.58). Further, in this work, the position root mean square error (PRMSE) is used as quantifying metric; the square root is applied over the positional terms of PCRLB given in (3.59). Also, in this chapter, PCRLB corresponds to the square root PCRLB of the positional terms unless specified.

3.5 Results and discussion

The results and discussion are presented in this section. A single radar case and multiple radar cases are considered to illustrate the ambiguity of target tracking in the presence of IWCTs and to mitigate its effect.

3.5.1 Single radar case

In this case, a single radar, single target, and multiple IWCTs are considered to exemplify the problem of target tracking.

A   Scenario generation

The simulation scenario considered is that the radar and IWCTs are assumed to be static in a given surveillance region of $12000 \times 12000 \text{m}^2$ with a maximum range at which radar can detect the targets is 12000m. First, the simulations are considered for the case of existence of a single radar present at the origin $[0,0]'$ and four in-band static transmitters; their locations are presented in TABLE 3.1 (near-geometry refers to nearby IWCTs to radar, and far-geometry refers to IWCTs are located far from radar). Only a single target is considered with constant velocity (CV) model; the initial state of the target is

$$\mathbf{x}(0) = [x, \dot{x}, y, \dot{y}]' = [1000, 30, 1000, 0]'. \tag{3.60}$$

The target protuberance in both position and velocity components is modeled as process noise, follows additive white Gaussian pdf, and is considered as

$$\mathbf{v} = \left[\mathcal{N}(0, 0.05^2), \mathcal{N}(0, 0.02^2), \mathcal{N}(0, 0.05^2), \mathcal{N}(0, 0.02^2) \right]'. \tag{3.61}$$

The values of process noise are chosen with an intent to focus the target tracking performance with the measurements resulted owing to IWCTs, not on model mismatches. The target starts at 1s and ends at 100s. The sampling time of the radar is 1s. On the other hand, the radar receives the range and azimuth measurements and are corrupted with the additive Gaussian noise; and the measurement noise vector is given by

$$\mathbf{w} = \left[\mathcal{N}(0, 10^2), \mathcal{N}(0, 0.03^2) \right]' \tag{3.62}$$

B   Tracker

The EKF framework is used in the tracker; the tunable parameters like process noise covariance and the measurement noise covariance in (3.17) and (3.21) are tuned to

$$\mathbf{Q} = \text{diag}([0.05^2 \ 0.02^2 \ 0.05^2 \ 0.02^2]) \tag{3.63}$$

$$\mathbf{R} = \text{diag}([10^2 \ 0.03^2]) \tag{3.64}$$

Table 3.1: In-band wireless communication transmitters location for single radar case.

In-band transmitter	near-geometry		far-geometry	
	x (m)	y (m)	x (m)	y (m)
1	300	1700	6000	3000
2	1500	1500	500	8000
3	2000	1500	5000	500
4	1700	1800	3000	5000
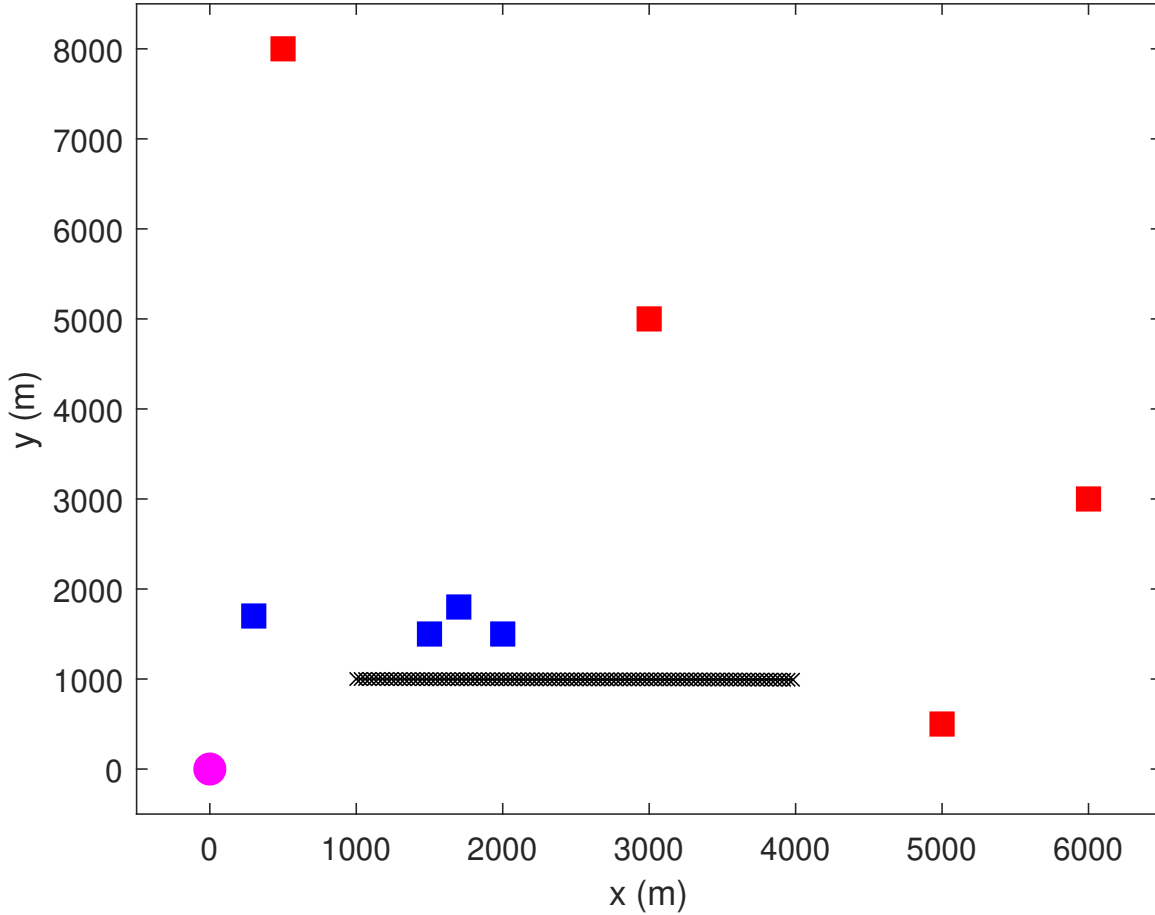
Figure 3.3: Scenario generation for a single radar case, where the circle indicates radar location, squares represent in-band transmitters (red color for far-geometry and blue color for the near-geometry scenario), and the black line replicates the target trajectory.

For track initialization, single point track initialization method (Musicki and Song, 2013) is used with maximum velocity, $V_{\max} = 30$m/s. A GNN association-based EKF,

with a CV model, is deployed in the tracking framework. A gating technique is used to validate the measurements, which follows a chi-square distribution $\chi_d^2(1-t_p)$, where d is the degree of freedom and t_p is the tail probability. Here, the logic-based track maintenance (He *et al.*, 2013) is opted to confirm or delete the tracks. Once the tracks are initialized, based on the number of measurements being assigned in the given frames, the tracks are either confirmed or deleted. The track confirmation is based on 7/10 logic, and track termination/deletion is based on 4/10 logic.
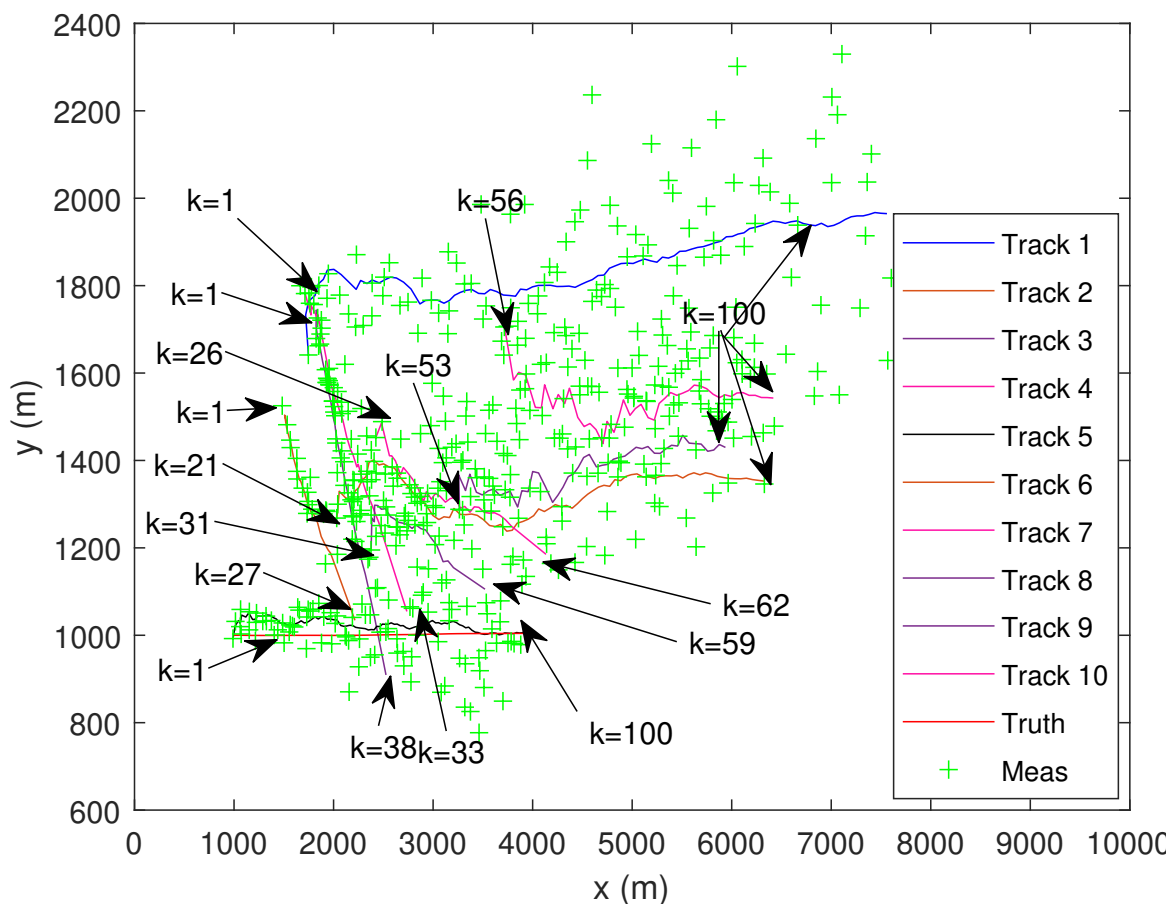
Figure 3.4: Tracking in state space for near-geometry scenario.

In a single radar case, near and far geometry scenarios are examined to evaluate the tracking performance. For the near-geometry scenario, the IWCTs are close to both the radar and target; the simulation scenario is shown in Figure 3.3. After the measurements are processed with the GNN tracker, it is observed from Figure 3.4 that ten tracks are reported by the tracker, in which two tracks are full-length tracks, and the rest are partial tracks. Since the target is moving in the given surveillance, the acquired measurements change over time and may not fit in the predefined models

like CV, constant acceleration (CA), and coordinated turn (CT). This wrong measurement to track association leads to track breakages and, in turn, results in track termination over time. It is observed that track-2, track-3, and track-4 are terminated at $k = 27$, $k = 38$, and $k = 33$ respectively. Whereas track-1 is the false track that occurred throughout the simulation. Interestingly, the track due to monostatic returns is preserved and is reported as a full track with the ID of track-5. The unassociated measurements corresponding to terminated tracks give birth to new tracks as track-6, track-7, track-8. The track-6 evolved at $k = 21$ and continued till $k = 100$, whereas track-7, track-8 are evolved at $k = 26$, $k = 31$ and continued till $k = 62$, $k = 59$ and then terminated. They gave birth to new tracks (track-9, track-10) that evolved at $k = 53$, $k = 56$ and are confirmed till the end. It is noticed that track-2 and track-6 belong to the same track. Also, track-3, track-8, and track-9 belong to the same track. Further, track-4, track-7, and track-10 belong to the same track and correspond to the same in-band transmitter. Sometimes, the overlapping of tracks is due to the last five predictions of the tracks before termination. Hence, the presence of IWCTs near both the radar and target results in more tracks with track breakages.

The simulation scenario for the far-geometry case, where IWCTs are located far from the target and radar, is depicted in Figure 3.3. In this scenario, it is observed from Figure 3.5 that the GNN tracker has reported five tracks. All the reported five tracks are of full length i.e., from $k = 1$ to $k = 100$. Among the five tracks, only track-5 is the true track; the rest corresponds to the measurements arising from the IWCTs. Compared to the near geometry case, the track reports and track breakages are less. Although, in both cases, IWCTs produce false tracks, making the tracker ambiguous to decide which track belongs to the true target. Further, the confirmed false tracks report that more targets are present in the given surveillance region. It is hard to distinguish the true track from all the available tracks. Hence, in this research, it is proposed to use the local tracks obtained from multiple radars and resolve the ambiguous tracks.

3.5.2 Multiple radar case

This subsection examines the case of distributed radars and in-band transmitters. Initially, two radars (R1, R2) and four IWCTs (C1, C2, C3, and C4) are considered
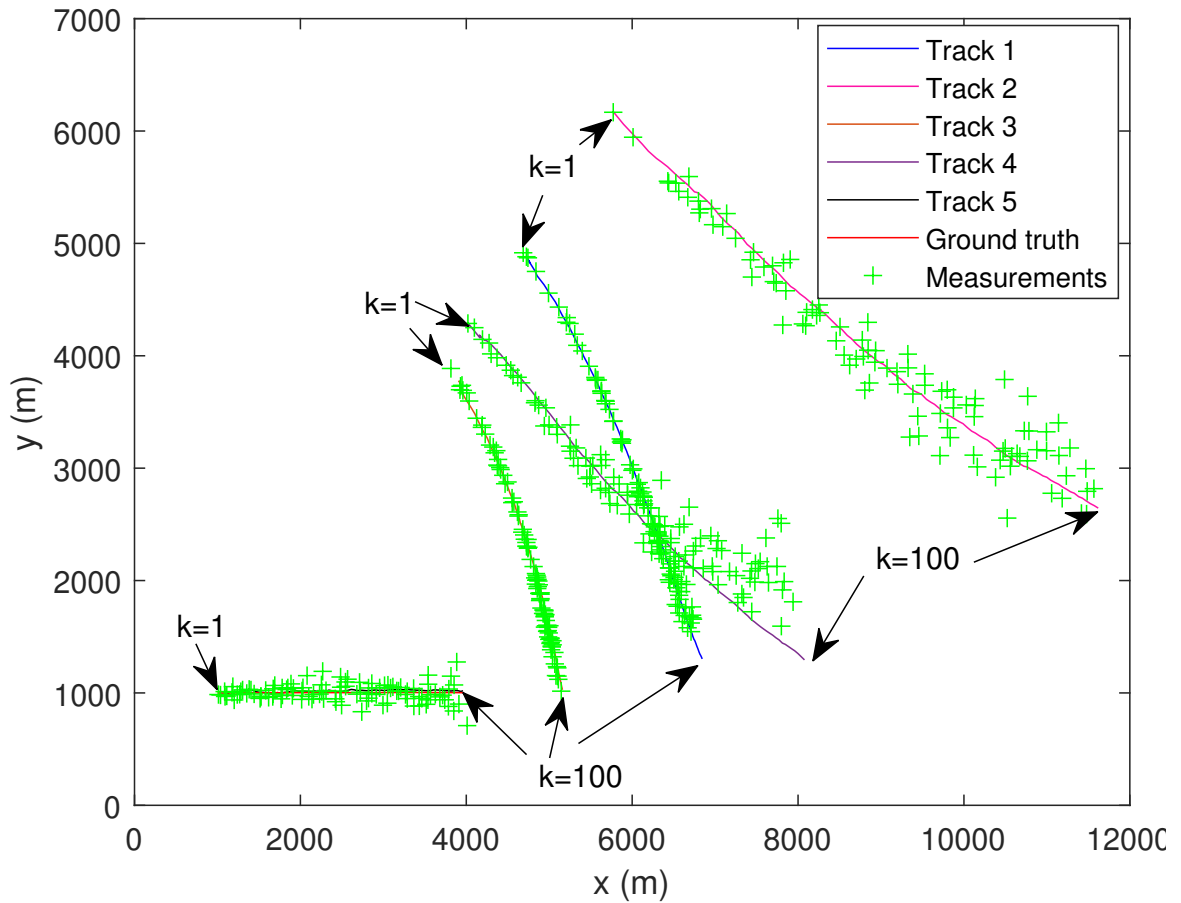
Figure 3.5: Tracking in state space for far-geometry scenario.

in the surveillance region. Next, this case is extended for four radars (R1, R2, R3, R4). It is assumed that both radars and IWCTs are static. In contrast, the target is dynamic and follows the CV model. The locations of both radars and in-band communication transmitters are tabulated in Table 3.2 and are depicted in Figure 3.6. Since the distributed tracking followed by fusion is deployed, each radar provides its local tracks. The track-to-track association is performed on the local tracks as presented in Section 3.3.1. In this process, the overall optimization provides the tuples of tracks. Among them, only one track is quantified by performing a chi-square distribution test. Once the true track associated with each radar is known, these quantified local tracks are fused at the fusion centre to yield a global estimate, using the various correlation-free fusion algorithms are presented in Section 3.3.2.

Figure 3.7 shows the obtained local tracks of R1 and R2 sensors in a clean environment (unity target detection probability and zero false alarm density). It is observed that even though there exists a single target in the surveillance, multiple tracks result

Table 3.2: The locations of Radars and In-band wireless communication transmitters for multiple radar case.

	Radar (R)		In-band transmitter (C)	
S.No.	x (m)	y (m)	x (m)	y (m)
1	5000	2000	500	500
2	500	2000	500	8000
3	700	9000	5000	500
4	6000	7000	6000	8000
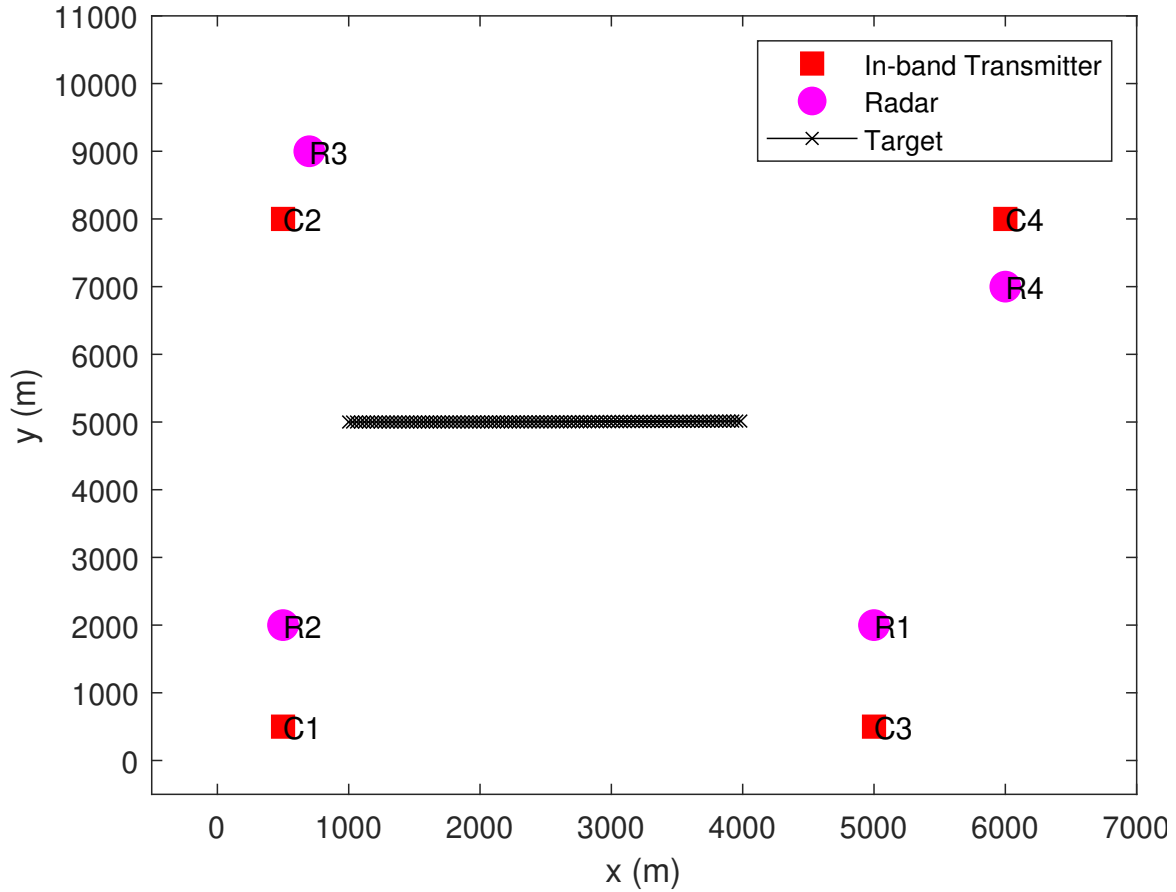
Figure 3.6: Scenario generation for multiple radar case.

at each sensor. Only two local tracks represent the actual target tracks pertaining to sensor-1 and sensor-2. The rest of the tracks fall apart within the surveillance due to the additional time delay introduced by the IWCTs. Further, if the IWCTs are co-located in the vicinity of the radar, then the false local track corresponding to IWCTs also appears near the true trajectory locations. In this case, due to the spatial deployment of IWCTs, it is observed that the local tracks are spatially separated. It

70

is worth noting that one local track from the track set of each radar represents the true target. In the case of low target detection probability, the above condition of one local track from the target set becomes unrealistic. In addition, with the T2TA, the overlapped tracks appeared as a tuple. Even with the increase in the number of radars, a single track from the track set represents the actual target track, and it is easily be quantified by using T2TA.
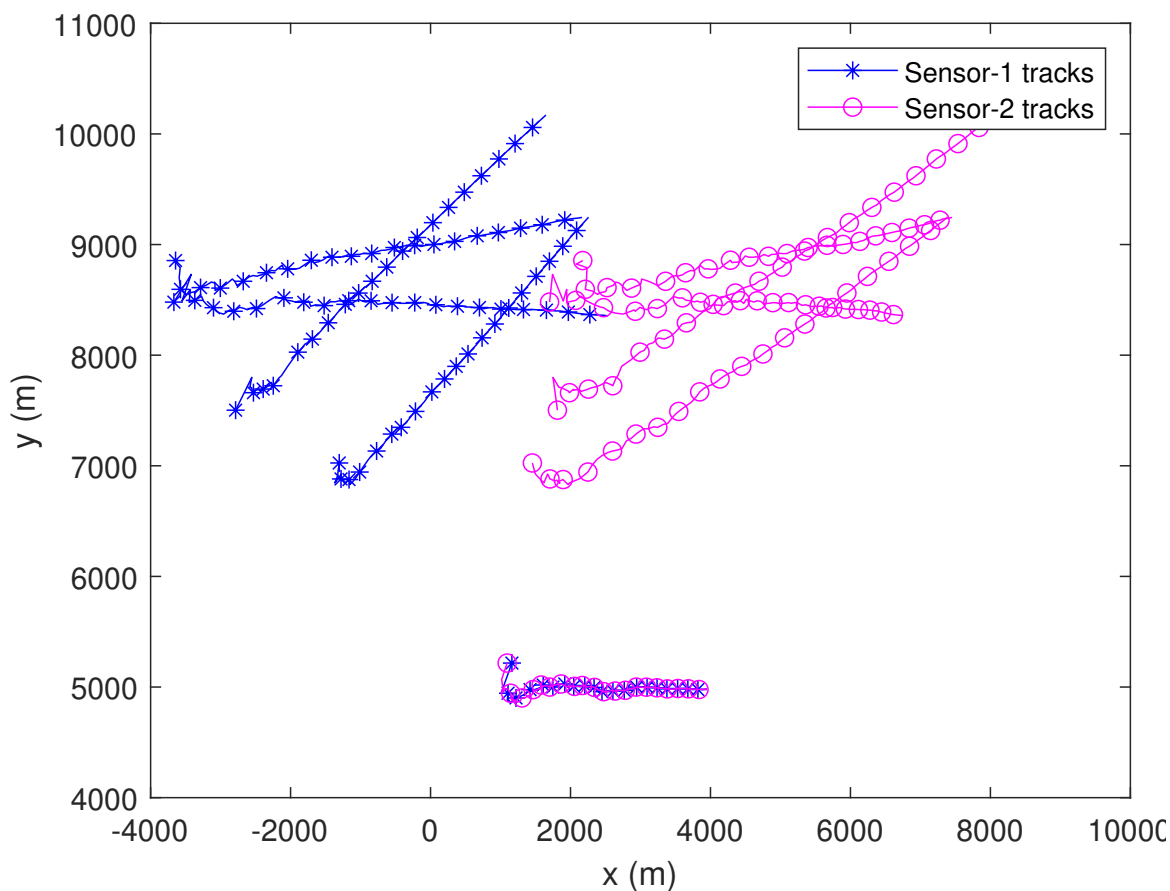
Figure 3.7: Illustration of local tracks pertain to R1 and R2 with unity p_D and zero false alarm density.

Figures 3.8-3.10 show the PRMSE and the corresponding achievable lower bound (PCRLB) of the fused tracks and the associated radar tracks for two radar case, by choosing different p_D and false alarm density. The ellipsoidal intersect (EI) (Sijs *et al.*, 2010) and CI fusion methods have been used for a two radars case to find the fused state estimates. The ellipsoidal method uses the mutual information-based mean and covariance, which are derived using two initial estimates, to calculate the final fused mean and covariance (Sijs *et al.*, 2010). On the other hand, CI uses trace

or determinant minimization to determine the fused covariance. This minimization becomes a nonlinear convex optimization problem. The solution is found using the well-known polynomial root-finding problem, which allows closed-form solutions to find the final fused covariance.
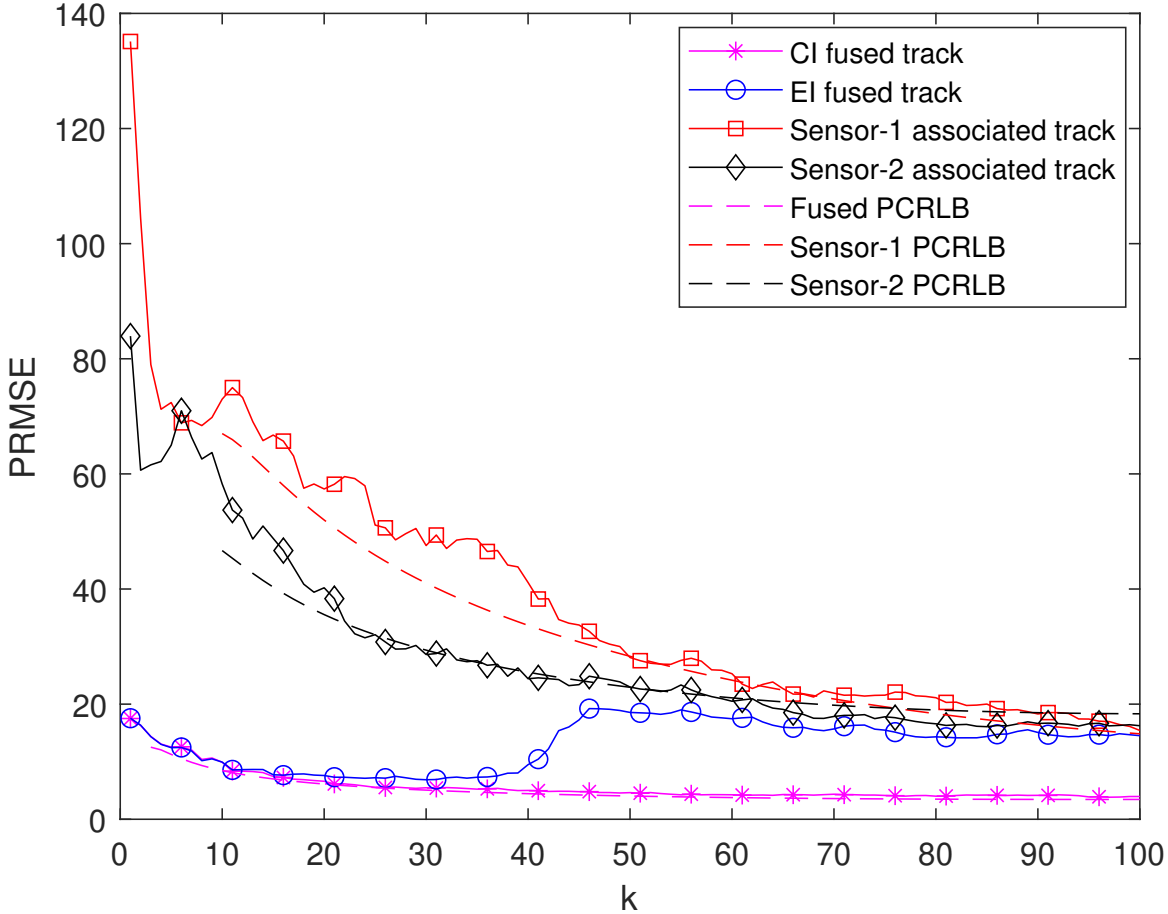
Figure 3.8: PRMSE of two radar case with unity p_D and zero false alarm density.

In particular, Figure 3.8 shows the PRMSE for clean environment. Since the tracker is initialized with a one-point initialization, with $V_{max} = 30$ and converted measurement, the PRMSE is very high at $k = 0$. During the time period of $k \in [1, 20]$, the filter settles its covariance, and it is visualized that the PRMSE is decreasing over time. After a certain time, $k = 40$, the filter is settled, and the settled PRMSE values are observed. Interestingly, the fused estimate with EI agrees with the CI method till $k = 40$, and its performance begins to degrade after a few scans. This is due to the unsettled covariance of any of the tracks. It is the main drawback of the ellipsoidal method. The fusion with the CI method provides improved performance compared

to the EI and has less fused PRMSE values.
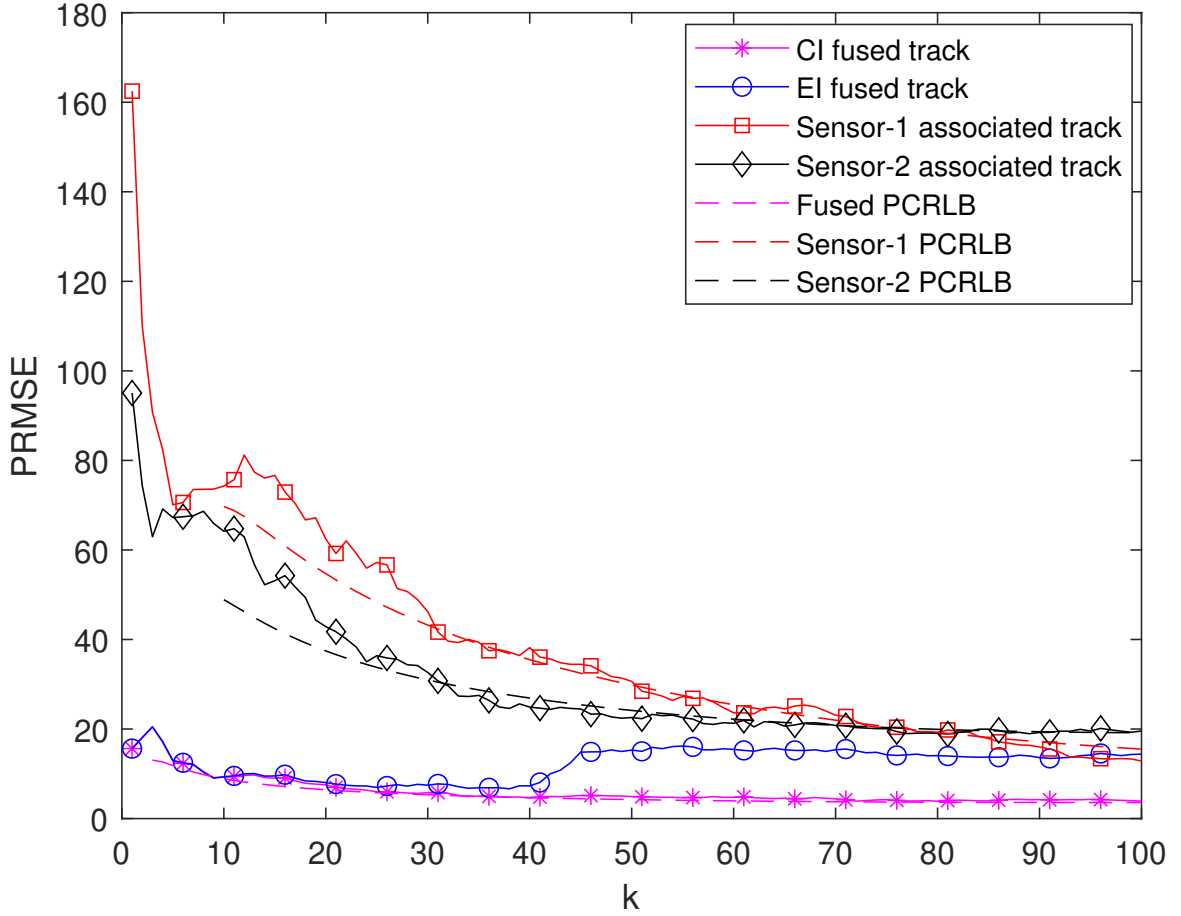
Figure 3.9: PRMSE of two radar case with p_D 0.9 and false alarm density as 1×10^{-7}.

Figures 3.9 and 3.10 show the PRMSE of the two radar case having false alarm density 1×10^{-7} with p_D as 0.9 and 0.8, respectively. It is observed from Figure 3.9 that the PRMSE of the associated tracks has a higher value in comparison with Figure 3.8. It is because the decrease in p_D increases the measurement ambiguity. Since the track termination rule follows 4/10, it indicates that a continuous track exists even though there is an absence of measurement for three consecutive scans. During the unavailability of measurement in a given scan, the tracker uses the predicted estimate as an updated estimate. The prediction state cannot withstand the error due to the process noise, which in turn raises the PRMSE values for these scans. In the presence of measurement origin uncertainty, the continuous track can be achieved with degraded accuracy by increasing the track termination rule. Even though PRMSE of the associated tracks has a noticeable degrade with the decrease in p_D, the fused esti-
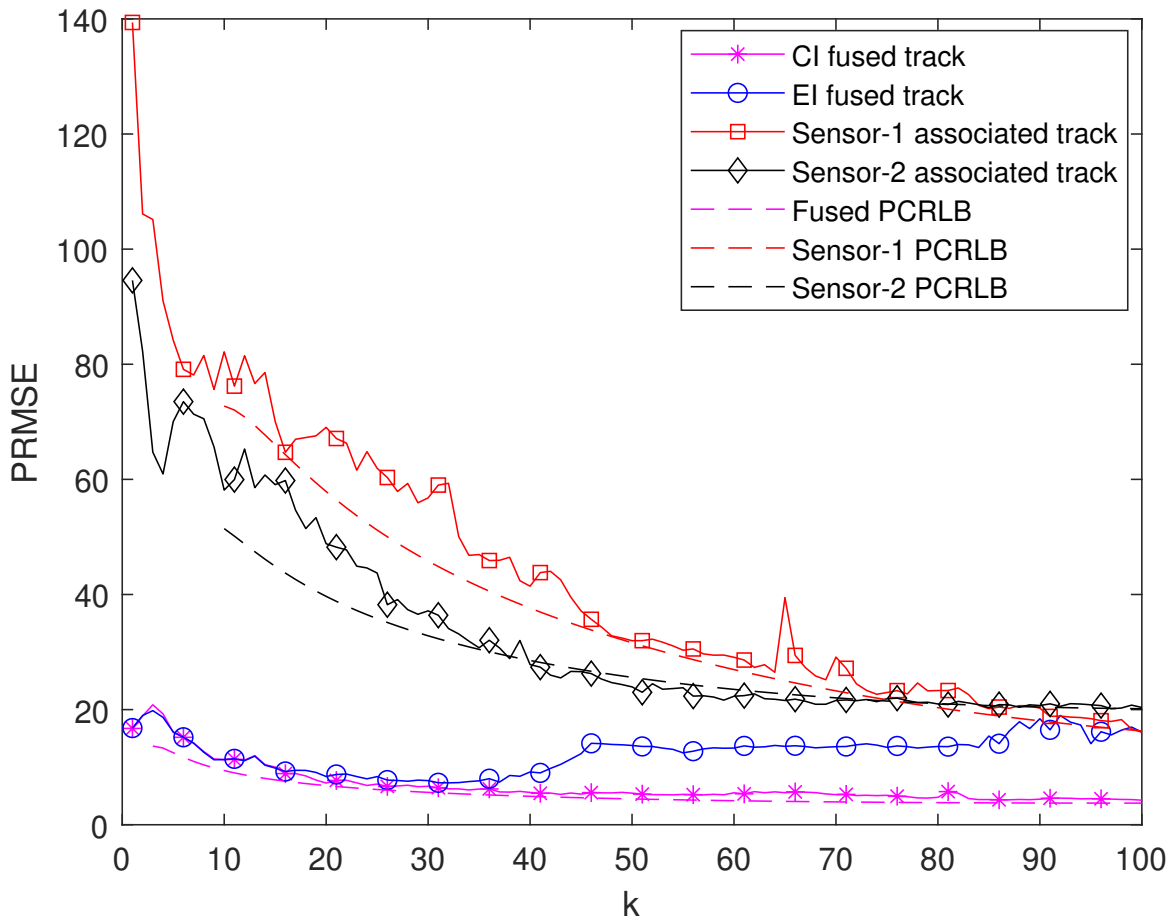
Figure 3.10: PRMSE of two radar case with p_D 0.8 and false alarm density as 1×10^{-7}.

mate has less performance degradation. Similar statements hold true for Figure 3.10. Further, from Figures 3.8-3.10, it is noted that the estimation PRMSE values are in agreement with the PCRLB values.

Generally, the fusion of individual local estimates leads to a better estimate. Assuming that four radars (R1, R2, R3, R4) are present in a surveillance region, the Figures 3.11-3.13 show the PRMSE of the four radar case for different values of p_D and p_{FA}. The PRMSE is also quantified with PCRLB. The locations of the radars are provided in Table 3.2 and are depicted in Figure 3.6. In contrast to two radar case, the SCI method is deployed here to fuse the associated tracks; as the EI is limited to two sources, the CI is computationally expensive for more sources. In contrast to CI, the SCI first fuses the local track estimates with an assumption that they are independent. After that, the covariance size of the fused track estimate is modified through a sampling process. The fuser weight parameter plays a critical role in estimating the mean in SCI. For a given unity fuser weight, the fuser is pessimistic. Whereas, for a
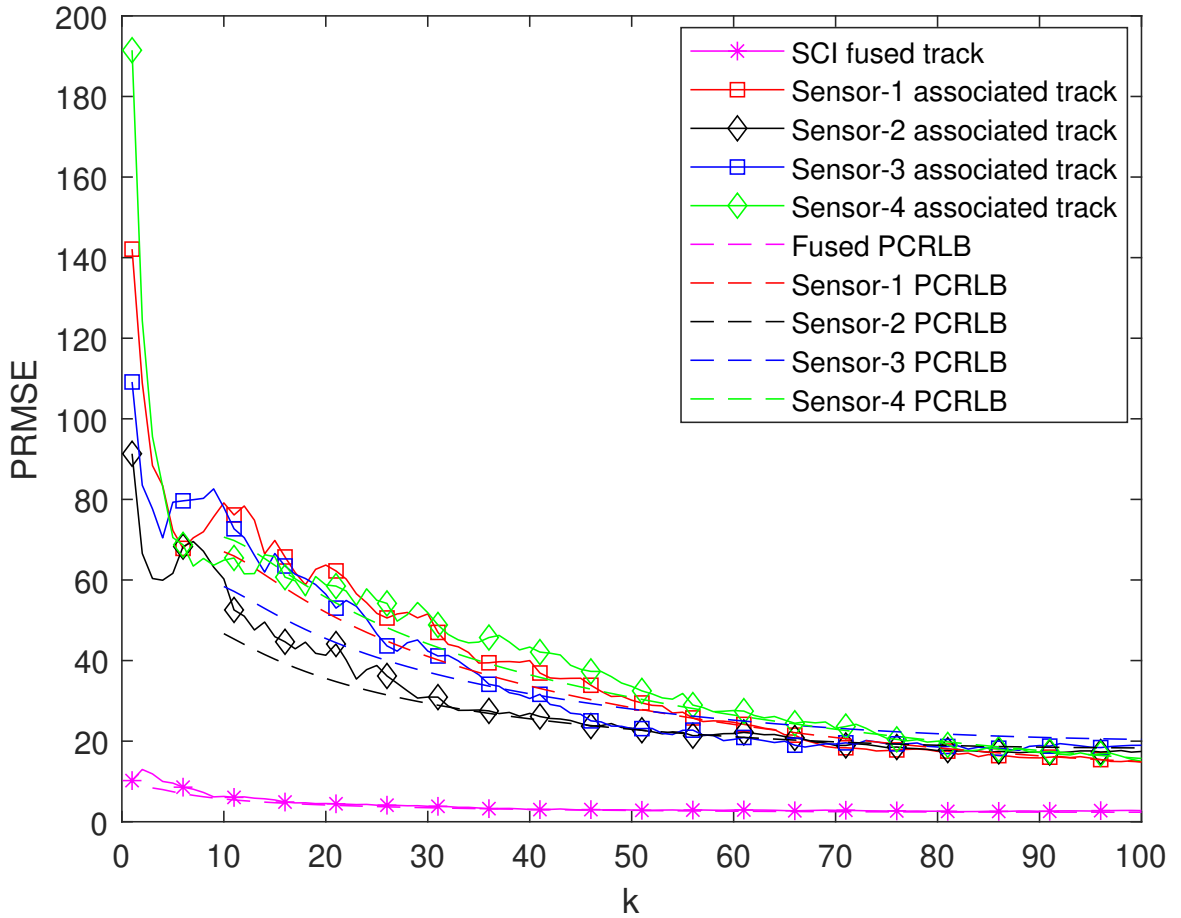
Figure 3.11: PRMSE of four radar case with unity p_D and zero false alarm density.

zero fuser weight, the fuser is optimistic. The fuser weight of 0.5 provides the best consistency (Tian *et al.*, 2010). Henceforth, in this simulation, the fuser weight value is set to 0.5.

It is observed from Figures 3.11-3.13 that, since a single point initialization is used (Mallick and La Scala, 2008), the PRMSE for initial time stamps is higher. Once the covariance of the filter is settled, the PRMSE decreases with the increase in time. Further, the PRMSE values of Figure 3.12 and 3.13 are higher when compared to the clean environment, shown in Figure 3.11. The decrease in p_D increases the measurement ambiguity at the radar, which in turn increases the PRMSE. Besides, it is worth noting from Figures 3.11-3.13 that, the four radar fusion estimate provides improved PRMSE compared to the two radar case of Figures 3.8-3.10. Also, from Figures 3.8-3.13, it is noted that, the increase in the number of radars considered for fusion further improves the estimation PRMSE values and meets with the fused PCRLBs.
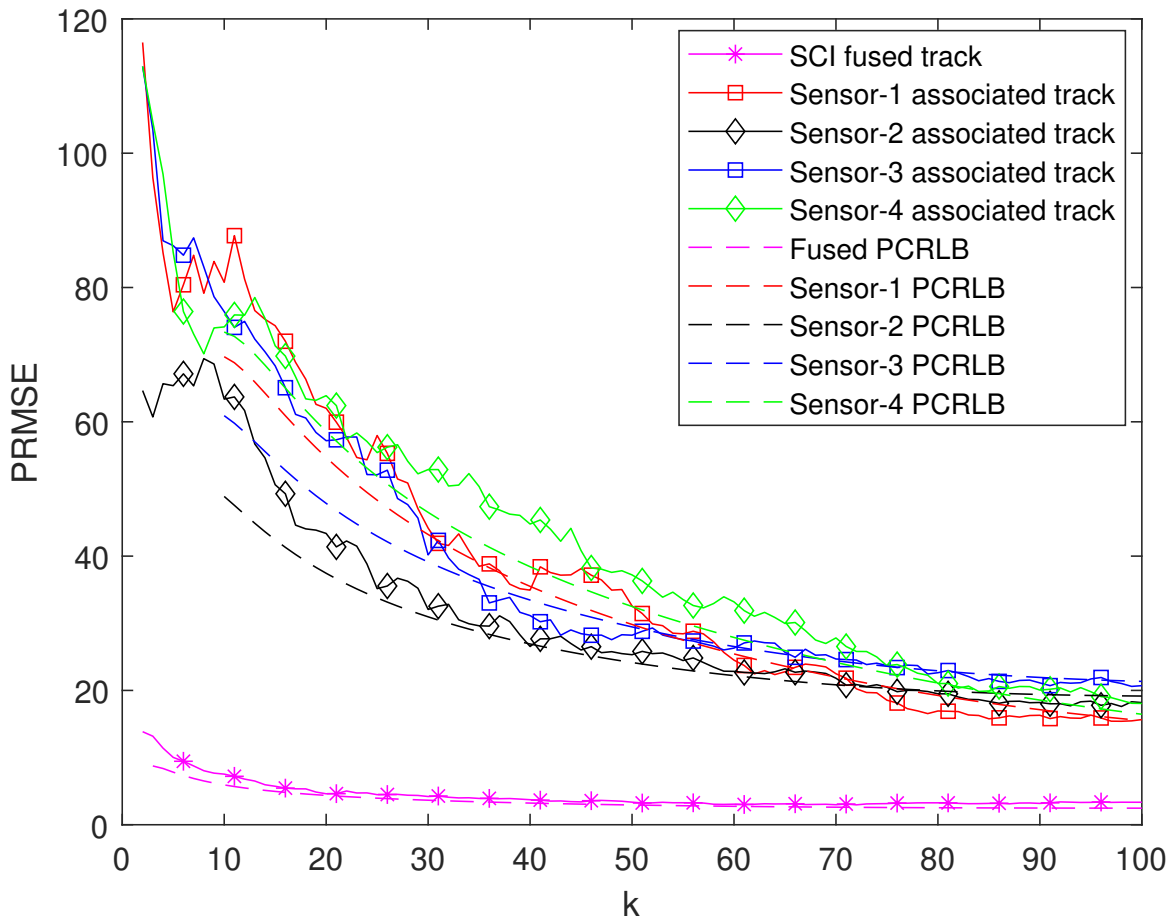
Figure 3.12: PRMSE of four radar case with p_D 0.9 and false alarm density as 1×10^{-7}.

To clearly show the efficacy of fusing the information from multiple radars, Figure 3.14 shows the PRMSE of the four radar case and two radar case for different values of p_D. Further, to clearly distinguish the difference in PRMSE, Figure 3.14 is plotted with X-axis on a linear scale and Y-axis on a logarithmic scale. It is worth noting that the PRMSE of the four radar fusion estimates is always less when compared to two radar fusion for various values of p_D. For example, for $p_D = 0.9$, the four radar case PRMSE is lower than the two radar case and holds true for other values of p_D. The four radar case fusion provides a two-fold performance compared to two radar case fusion. Therefore, the deployment of more radars not only benefits the elimination of false tracks but also provides improved target tracking performance. Further, fusing the information from more sensors improves the estimation accuracy, with PRMSE values much closer to PCRLBs.
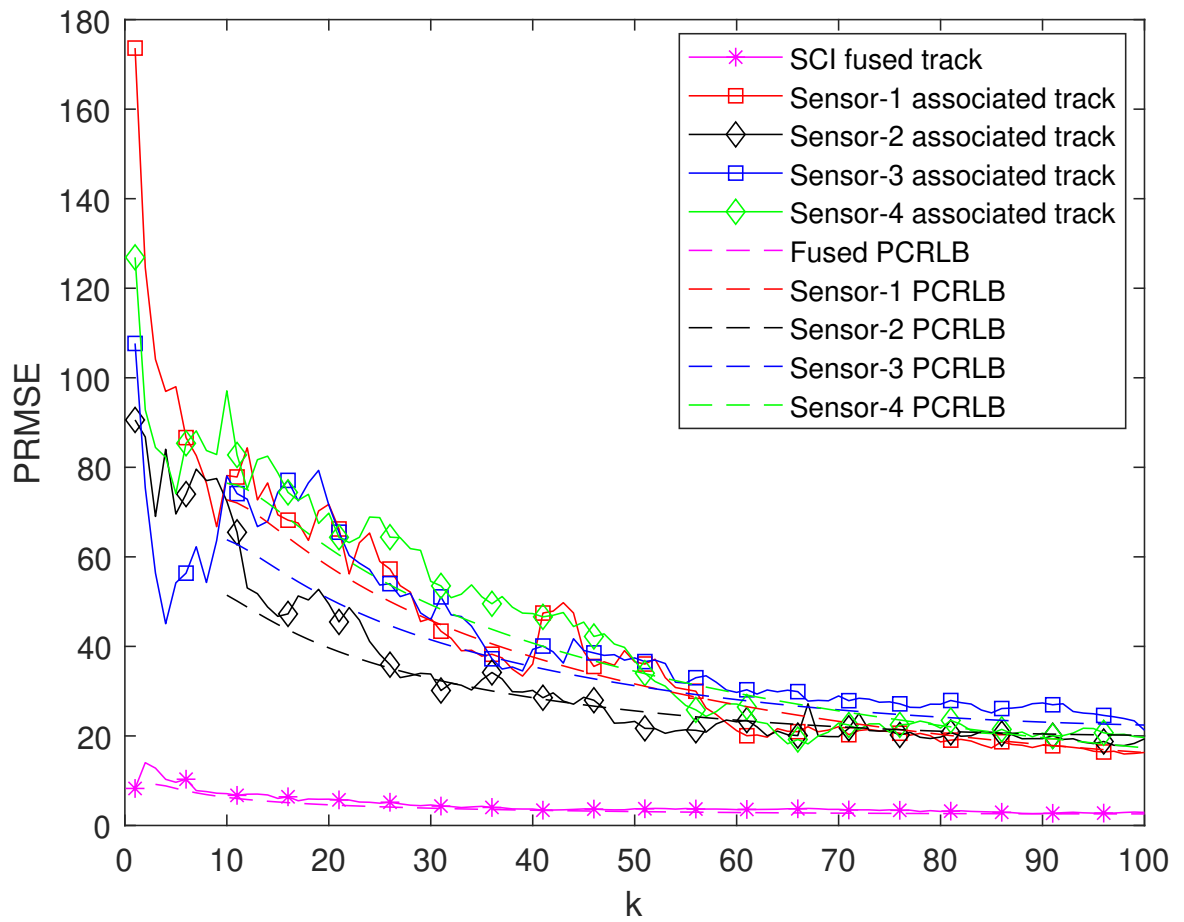
Figure 3.13: PRMSE of four radar case with p_D 0.8 and false alarm density as 1×10^{-7}.
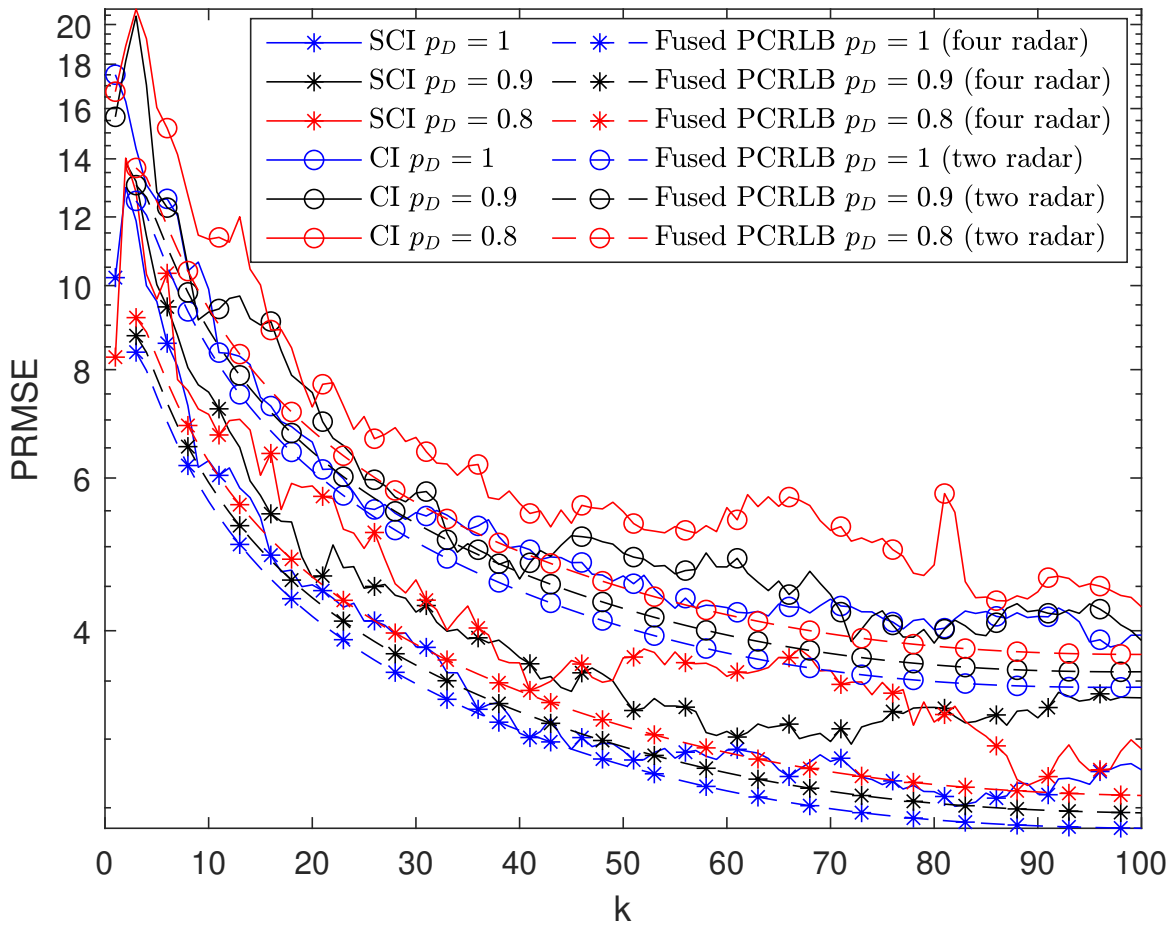
Figure 3.14: Comparison of PRMSE for four radar and two radar case with varying p_D.

Chapter 4

Information Theory Based Performance Analysis of Spectrum Sharing Radar

This chapter presents the performance analysis of the radar and communication system (RadComm) spectrum sharing scenario. The analysis is carried out by considering the spectrum sharing radar (SSR), capable of detecting the radar targets and simultaneously acting as a communication receiver. To evaluate performance, mutual information (MI), spectral efficiency (SE) and capacity (C) metrics are used. The MI and capacity results show that using the successive interference cancellation (SIC) scheme in a mixed-use band yields performance comparable to traditional radar and communication system. In terms of SE, the SSR with SIC scheme outperforms traditional radar and communication system.

4.1   Problem formulation

The spectrum sharing radar (SSR) capable of detecting the radar targets and simultaneously acting as a communication receiver is considered, as shown in Figure 4.1. It is assumed that total available bandwidth (B_{SSR}) of the SSR split among radar only sub-band with bandwidth (B_r) and mixed-use bandwidth (B_{mix}). Here, mixed-use refers to both radar and communication purposes. The SSR is capable of extracting the target information from the radar-only sub-band. Meanwhile, the mixed-use band is for both target information and communication data. Since this study analyses the performance from the radar perspective, Figure 4.2a illustrates the radar target channel model of SSR from the information-theoretic viewpoint. The radar transmitted
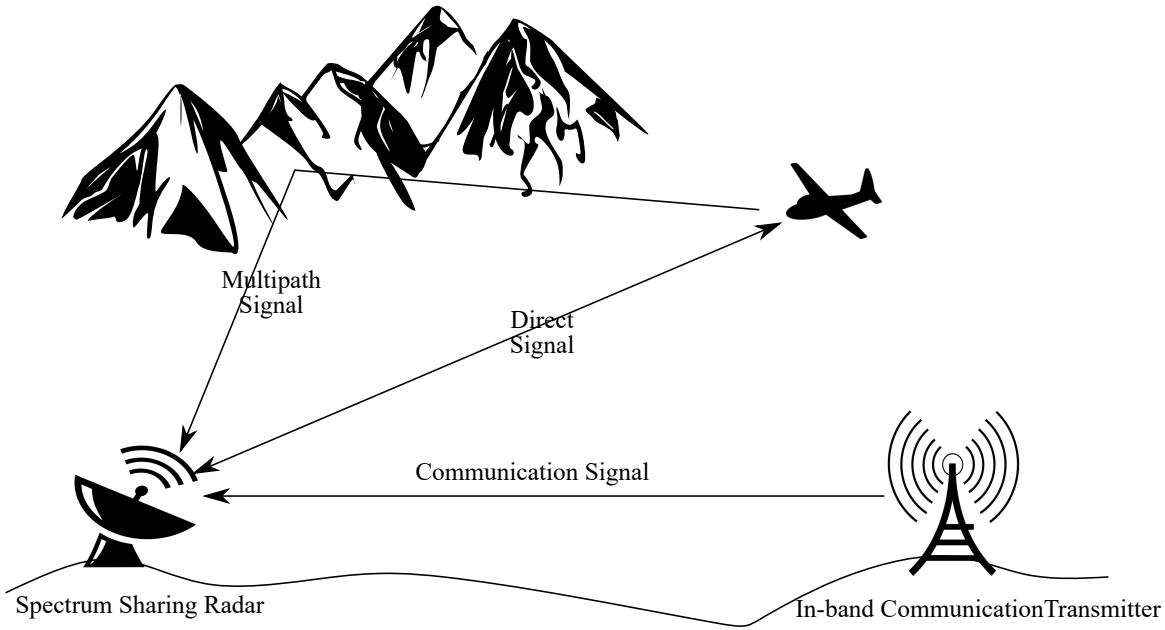
Figure 4.1: System model of a Spectrum sharing radar.

waveform $x(t)$ impinges on the target and gets scattered by it. The scattered signal with additive noise is received at the SSR receiver and further processed to extract the target information from radar-only and mixed-use bands. The target-to-receiver channel equivalent mathematical model is shown in Figure 4.2b, where $x(t)$ is the radar transmitted waveform, with duration T having the energy E_x. The $g(t)$ is the target scattering characteristics model/ impulse response; $h(t)$ is the resulting target scattered signal. The $w(t)$ is the zero-mean white Gaussian noise having the power spectral density P_{ww}, which is independent of $x(t)$ and $g(t)$. The $w(t)$ is represented with an intent that the overall SSR system bandwidth ($B_{SSR} = B_r + B_{mix}$) is influenced by the same noise. The ϵ quantifies the loss of target information in the received signal owing to in-band communication interference for the mixed band system operation. The received signal/ measurement model at the radar receiver from the radar only sub-band is given by (Bell, 1993; Bliss, 2014)

$$
\begin{aligned}
z_r(t; B_r) &= f(h(t), x(t), g(t)) + w(t) \\
&= \sqrt{P_r} s_r(t - \tau) + w(t).
\end{aligned}
\tag{4.1}
$$

Here, $f(\cdot)$ represents the non-linear function and t represents the time, P_r is radar received power due to target return. Whereas the received signal/ measurement model

80

from the mixed-use sub-band is represented as (Bell, 1993; Bliss, 2014)

$$z_r(t; B_{mix}) = f(h(t), x(t), \epsilon, g(t)) + w(t)$$
$$= \sqrt{P_r}s_r(t - \tau) + \sqrt{P_c}s_c(t) + w(t), \qquad (4.2)$$

where P_c is radar received power, owing to in-band wireless communication transmitter (IWCT), ϵ is a Bernoulli random variable, which quantifies the effect of the target information reduction in mixed-use sub-band. The ϵ is equal to zero, when there is no target information is extracted in mixed-use-band, ϵ takes the value to unity when the target information is extracted.

For the mixed-use sub-band, two cases have been assumed: with successive interference cancellation (SIC) and without SIC. It is assumed that when the SIC method is used, the received signal at the radar receiver will get suppressed with predicted communication symbols. Hence, it cancels the in-band interference effect in mixed-use band (Patel and Holtzman, 1994; Bliss, 2014). Therefore, the received signal with SIC in mixed band from radar perspective is given by

$$z_{r_{SIC}}(t; B_{mix}) = f(h(t), x(t), \epsilon, g(t)) + w(t)$$
$$= \sqrt{P_r}s_r(t - \tau) + \sqrt{P_c}\left(s_c(t) - s_{c_{pre}}(t)\right) + w(t)$$
$$= \sqrt{P_r}s_r(t - \tau) + w_{int+n}(t), \qquad (4.3)$$

where $w_{int+n}(t) = w_{residual}(t) + w(t)$. Here, "$int$" refers to in-band interference, "n" refers to noise. Whereas, mixed-use band without SIC will not predict and suppress the in-band communication symbols, results in strong in-band interference effect, which nullifies target information in that particular sub-band. Therefore, the received signal without SIC in mixed band is same as (4.3) with $w_{int+n}(t) = \sqrt{P_c}s_c(t) + w(t)$. Similar equation holds true from communication perspective in mixed-used band by interchanging the radar and communication signals in (4.3).

The received signals $z_r(t; B_r)$, $z_r(t; B_{mix})$ given in (4.1) and (4.2) are processed to extract the target information. Let $I_{B_r}(t)$ and $I_{B_{mix}}(t)$ be the extracted target information from radar only sub-band and mixed-use sub-band, respectively. It is assumed that these are additive and there is no overlap exist in the information received. So, the overall target information $I_{SSR}(t)$ from both the sub-bands is the summation of $I_{B_{mix}}(t)$ and $I_{B_r}(t)$.
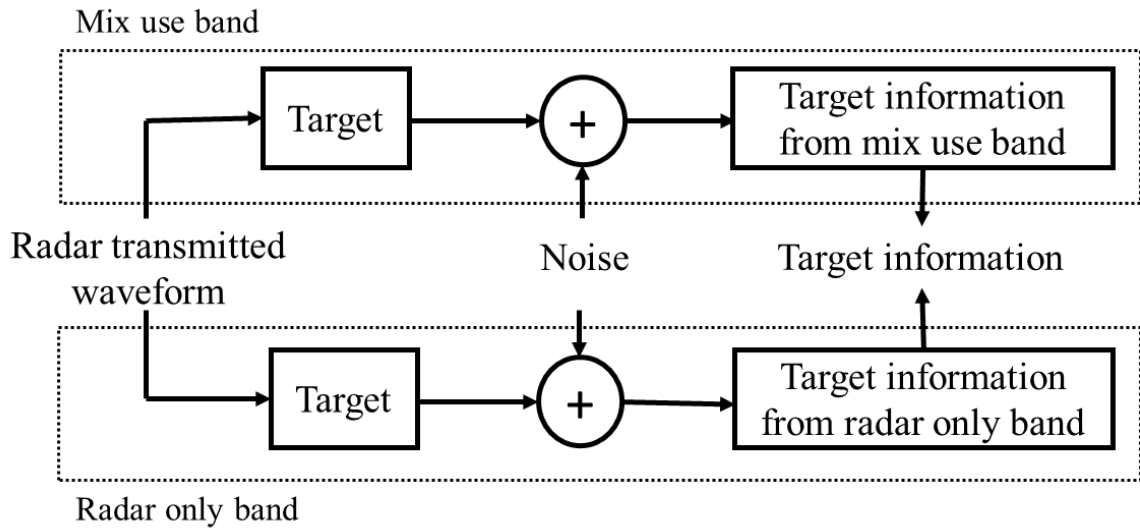
(a) Block diagram
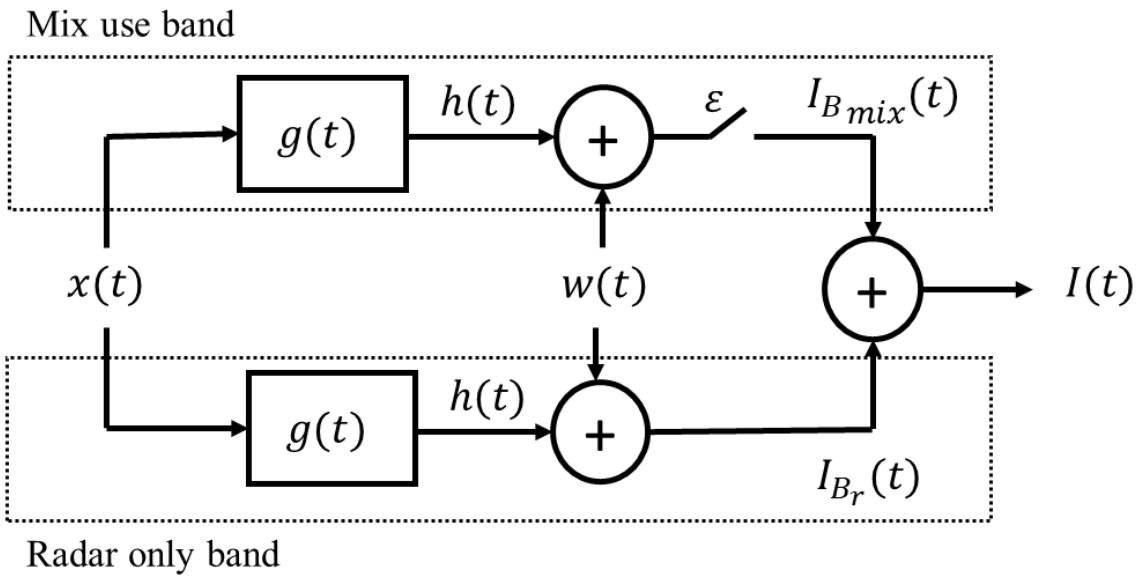
(b) Mathematical representation

Figure 4.2: Spectrum sharing radar target-to-receiver channel model.

To make the target-to-receiver channel model more realistic, it is also assumed that there exists multipath between the target-to-receiver channel, as shown in Figure 4.1. The mathematical representation of the multipath model of SSR in radar only band is shown in Figure 4.3. A similar figure holds true for the mixed-use band, and ϵ exists. N number of paths between the target-to-receiver are depicted in Figure 4.3. These multipaths are effected by noise $w(t) = f(w_1(t), \ldots, w_n(t))$. Here, $w_1(t), w_2(t), \ldots w_n(t)$ are the individual path noise components represented for mathematical convenience and are jointly contributing to a single noise component $w(t)$. Further, for simplicity, it is assumed that all the multipaths have a unity channel gain. By imposing subscript i to the (4.1), (4.2), results in received signal of ith path. The overall received signal at the radar receiver due to multipath from the radar only and mixed-use sub-band, is given by

$$
z_r(t; B_r) = \sum_{i=1}^{N} z_{r_i}(t; B_r),
$$
$$
z_r(t; B_{mix}) = \sum_{i=1}^{N} z_{r_i}(t; B_{mix}). \tag{4.4}
$$

Here, it is worth noting that $z_{r_i}(t; B_r)$, $z_{r_i}(t; B_{mix})$ are equivalent to (4.1) and (4.2) for single path.

For the RadComm spectrum sharing scenario considered, there is a strong need to quantify the target information available at the radar for a given transmitted waveform. Besides, SSR is also capable of acting as a communication receiver. Here, there is a strong requirement to estimate the information rate at the SSR. Similarly, it is essential to quantify how efficiently the SSR utilizes the spectrum. Given this, the performance analysis of SSR is carried out using three metrics, namely, mutual information (MI), spectral efficiency (SE), and capacity (C). MI is considered for target-to-receiver channel for a given transmitted waveform to quantify the target information that is available at the radar. The SE is adopted in this study to quantify how efficiently the spectrum is being utilized with the SSR. Finally, the capacity (C) metric is introduced to quantify the communication information rate at SSR.

The following, Sections 4.2 and 4.3, present the performance analysis of the SSR in a clean and multipath environment.
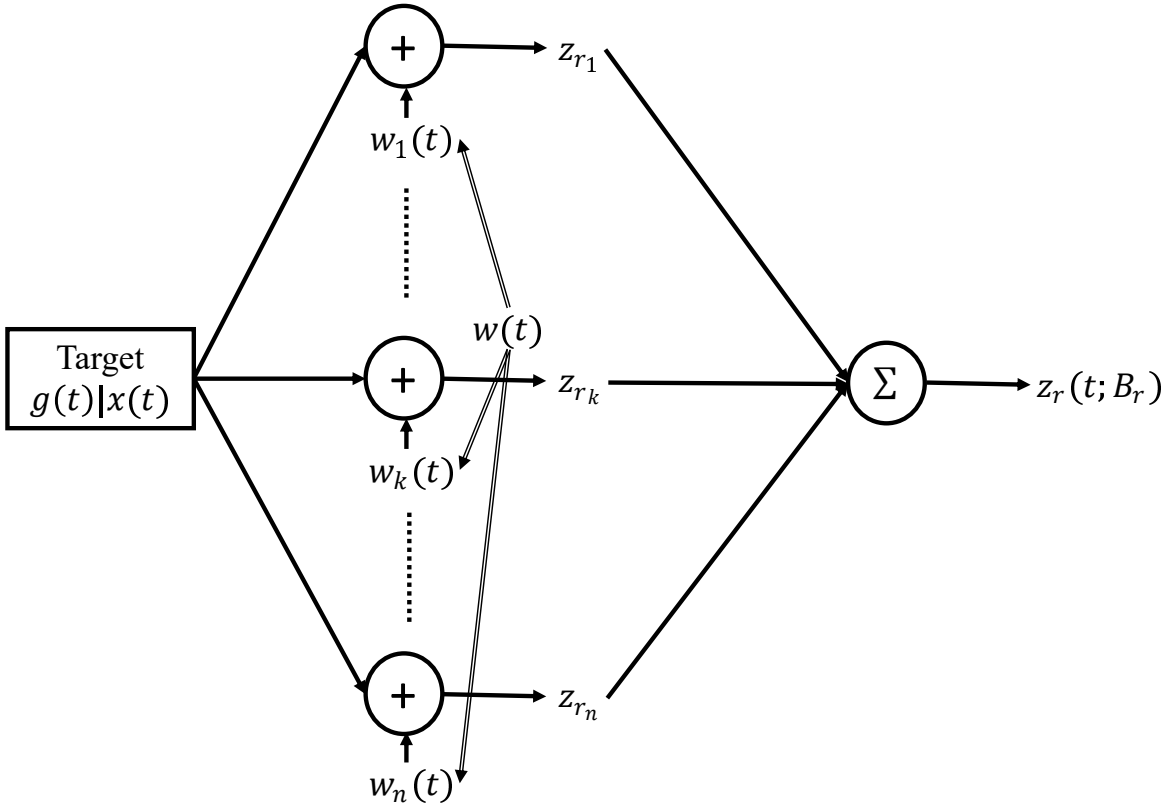
Figure 4.3: Multipath target-to-receiver channel model of spectrum sharing radar in radar only band.

4.2 Performance analysis in a clean environment

In this section, the performance analysis of SSR in a clean environment is presented using MI, SE, and C metrics.

4.2.1 Mutual Information (MI)

The total MI between the the the target characteristics $g(t)$ and the received signal at the radar receiver $z_r(t)$ over a bandwidth B_{SSR} is the summation of the MI in radar only band $I_{B_r}(t)$ and the MI in mixed-use band $I_{B_{mix}}(t)$. Here $B_{SSR}=B_r + B_{mix}$.

A   MI in radar-only band

Let $x(t)$ is the radar transmitted waveform with the energy E_x and period T. The MI ($I_{B_r}(z_r(t); g(t) \mid x(t))$) between the target-to-receiver in the presence of additive Gaussian noise (with $P_{ww}(f)$ as a one sided power spectral density) is maximized by $x(t)$ with magnitude squared spectrum (Bell, 1993)

$$|X(f)|^2 = \max\left[0, A - r(f)\right], \qquad (4.5)$$

where

$$r(f) = \frac{P_{ww}(f)T}{2\sigma_G^2(f)}, \tag{4.6}$$

$\sigma_G^2(f)$ is spectral variance of $g(t)$, and A is the solution of the equation

$$E_x = \int_{B_r} \max\left[0, A - r(f)\right] \, df, \tag{4.7}$$

with $r(f)$ defined in (4.6).

The resulting maximum MI $I_{B_r}^{max}(z_r(t); g(t) \mid x(t))$ over the radar only band interval $B_r = [f_c, f_c + B_r]$ is given by (Bell, 1993; Woodward, 2014; Cover and Thomas, 2012)

$$
\begin{aligned}
I_{B_r}^{max}(z_r(t); g(t) \mid x(t)) &= T \int_{B_r} \ln\left[1 + \frac{2|X(f)|^2\sigma_G^2(f)}{P_{ww}(f)T}\right] df \\
&= T \int_{B_r} \max\left[0, \ln A - \ln r(f)\right] \, df \\
&= TB_r \ln A - T \int_{B_r} \ln r(f) \, df \text{ (nats)}. \tag{4.8}
\end{aligned}
$$

Here, $\frac{2|X(f)|^2\sigma_G^2(f)}{P_{ww}(f)T}$ represents the signal to noise ratio (SNR) in radar only sub-band, represented as

$$\text{SNR}_{B_r} = \frac{|X(f)|^2\sigma_G^2(f)/T}{P_{ww}(f)/2} \tag{4.9}$$

B MI in mixed-use band

The MI in the mixed-use sub-band follows the similar procedure of radar-only band, except that, one needs to take the expectation over the variable ϵ, which incorporates the effect of in-band communication system interference. Therefore, the MI $I_{B_{mix}}^{max}(z_r(t); g(t) \mid x(t))$ over the mixed-use band interval $B_{mix} = [f_c, f_c + B_{mix}]$ is given by

$$
\begin{aligned}
I_{B_{mix}}^{max}(z_r(t); g(t) \mid x(t)) &= \mathbb{E}_{\epsilon}\left[I_{B_{mix}}^{max}(z_r(t); g(t) \mid x(t), \epsilon)\right] \\
&= 0 \times p(\epsilon = 0)I_{B_{mix}}^{max}(z_r(t); g(t) \mid x(t), \epsilon = 0) \\
&\quad + 1 \times p(\epsilon = 1)I_{B_r}^{max}(z_r(t); g(t) \mid x(t), \epsilon = 1) \\
&= p(\epsilon = 1)I_{B_r}^{max}(z_r(t); g(t) \mid x(t)). \tag{4.10}
\end{aligned}
$$

Here, $p(\epsilon = 1)$ represents the mean value of ϵ, takes the values between zero to one. It can be interpreted as an information reduction factor in the mixed-use band compared

to the radar-only sub-band.

Similar to (4.8), the general MI in mixed-use sub-band is given by

$$I_{B_{mix}}^{max}\left(z_r(t); g(t) \mid x(t)\right) \propto \ln\left(1 + \text{SINR}_{B_{mix}}\right) \tag{4.11}$$

Interpreting (4.10), (4.11), utilizing expressions (4.8) and (4.9), the mean ϵ can be defined as the ratio of signal to interference plus noise ratio (SINR) in mixed-use sub-band ($\text{SINR}_{B_{mix}}$) to the SNR in radar-only sub-band (SNR_{B_r}). However, in contrast to SNR_{B_r}, the $\text{SINR}_{B_{mix}}$ takes two forms. One without using the SIC scheme and the other is using the SIC scheme in mixed-use band (Tian et $al.$, 2019b). Similar to (4.9), the $\text{SINR}_{B_{mix}}$ without using SIC scheme is given by

$$\text{SINR}_{B_{mix}}^{\text{without SIC}} = \frac{|X(f)|^2 \sigma_G^2(f)/T}{P_{ww}(f)/2 + |S_c(f)|^2}, \tag{4.12}$$

where $|S_c(f)|^2$ $\left(P_c = \int_{B_{mix}} |S_c(f)|^2 df\right)$ denotes the in-band wireless communication transmitter power component. In contrast to (4.9), the additional term $|S_c(f)|^2$ in the denominator of (4.12) denotes the direct interference component.

Using the SIC scheme in mixed-use band subtract the received signal with predicted communication component (as represented in (4.3)). Hence, the resultant $\text{SINR}_{B_{mix}}$ using SIC scheme in mixed-use band is given by

$$\text{SINR}_{B_{mix}}^{\text{with SIC}} = \frac{|X(f)|^2 \sigma_G^2(f)/T}{P_{ww}(f)/2 + |S_c^{res}(f)|^2}, \tag{4.13}$$

where $|S_c^{res}(f)|^2 = |S_c(f) - S_{c_{pre}}(f)|^2$ represents the residual communication power component.

Using (4.12) and (4.9), the ratio of $\text{SINR}_{B_{mix}}^{\text{without SIC}}$ to SNR_{B_r} is assumed as $\bar{\epsilon}_1$, given by

$$\bar{\epsilon}_1 = \frac{P_{ww}(f)}{P_{ww}(f) + 2|S_c(f)|^2}. \tag{4.14}$$

Here, the denominator of $\bar{\epsilon}_1$ has the direct interference component of high value compared to noise, it is approximately equal to zero. It is in fact true that for a fixed value of noise power P_{ww}, (4.14) becomes $\bar{\epsilon}_1 = \frac{\text{constant}}{\text{constant+high value}} \approx 0$. Which indicates the minimum information retrieval in mixed-use band when SIC scheme is not adopted. Also, the ratio of $\text{SINR}_{B_{mix}}^{\text{with SIC}}$ to SNR_{B_r} is assumed as $\bar{\epsilon}_2$, given by

$$\bar{\epsilon}_2 = \frac{P_{ww}(f)}{P_{ww}(f) + 2|S_c^{res}(f)|^2}, \tag{4.15}$$

which is approximately equal to one because the denominator will only have residual interference component of less value compared to noise. Therefore, without loss of generality, using (4.10), (4.14), and (4.15) the MI in the mixed-use band is given by

$$
I_{B_{mix}}^{max}(z_r(t); g(t) \mid x(t)) \tag{4.16}
$$
$$
= \begin{cases} \bar{\epsilon}_1 & \left(TB_{mix} \ln A - T \int_{B_{mix}} \ln r(f) \, df \right) \\ & \qquad \qquad \text{without SIC scheme} \\ \bar{\epsilon}_2 & \left(TB_{mix} \ln A - T \int_{B_{mix}} \ln r(f) \, df \right) \\ & \qquad \qquad \text{with SIC scheme} \end{cases}
$$

Finally, the MI of the SSR is the sum of individual MI's in their respective sub-bands, is given by

$$
I_{B_{\mathrm{SSR}}}^{max}(z_r(t); g(t) \mid x(t)) = I_{B_r}^{max}(z_r(t); g(t) \mid x(t)) + I_{B_{mix}}^{max}(z_r(t); g(t) \mid x(t)). \tag{4.17}
$$

Here $I_{B_r}^{max}$ and $I_{B_{mix}}^{max}$ are defined in (4.8) and (4.16), respectively.

To show the comparison of the SSR with the traditional radar, MI of the traditional radar having BW (B_T) (Bell, 1993) is given by

$$
I_{B_T}^{max}(z_r(t); g(t) \mid x(t)) = T \int_{B_T} \max\left[0, \ln A - \ln r(f)\right] \, df \, (\text{nats}), \tag{4.18}
$$

where $r(f)$ and A have the similar form of (4.6) and (4.7), by replacing B_r with B_T.

4.2.2 Spectral Efficiency (SE)

In this subsection, the SE performance metric for SSR is presented. The SE is defined as a ratio of maximum MI between target-to-receiver of the SSR over the available bandwidth (Deng *et al.*, 2013; Chiriyath *et al.*, 2017). Therefore, the SE of the SSR is given by

$$
\mathrm{SE}_{SSR} = \frac{I_{B_{\mathrm{SSR}}}^{\max}}{B_{\mathrm{SSR}}}, \tag{4.19}
$$

where $I_{B_{\mathrm{SSR}}}^{\max}$ is given in (4.17) and B_{SSR} is the bandwidth (BW) used by SSR, defined as $B_{\mathrm{SSR}} = B_r + B_{mix}$.

To show the advantage of SSR over the traditional radar in-terms of SE, the SE of the traditional radar is also defined and is given by

$$
\mathrm{SE}_T = \frac{I_{B_T}^{\max}}{B_T + B_{mix}}, \tag{4.20}
$$

where $I_{B_T}^{\max}$ is given in (4.18). The additional BW B_{mix} to the B_T is considered in the denominator instead of taking the $2B_T$. Because, in traditional radar and communication system operation, where the spectrum sharing is not considered, a BW of B_r is used for radar purpose alone, and an extra BW of B_c is used for communication operation. Here, in SSR, the B_{mix} is the portion of BW which contains the communication information. Therefore, the net effective BW is $B_T + B_{mix}$ with the condition that $B_r = B_T$, and $B_c = B_{mix}$.

It is to be noted that the (4.19) shows the SE of SSR from the radar perspective. However, apart from radar target information, the SSR also receives the communication information in mixed-use band. Therefore, the SE of SSR from communication system perspective also needs to be quantified. It is known that the SE of communication system is the ratio of Capacity (C) to the BW used (Cover and Thomas, 2012), the SSR does not use any additional BW (zero B_c) for communication information retrieval, results into a infinite SE.

4.2.3 Capacity (C) in mixed-use band

In this subsection, the channel capacity calculation for SSR is presented. As, the mixed-use band of SSR consist of communication information apart from radar related information, therefore the capacity metric needs to be evaluated in this band. In general, the bandlimited Gaussian channel capacity with a BW $\mathcal{B}$, noise power spectral density of $P_{ww}/2$ watts/Hz, and power P_c watts is defined as (Cover and Thomas, 2012)

$$C = \mathcal{B} \ln \left(1 + \frac{P_c}{P_{ww}\mathcal{B}} \right) \tag{4.21}$$

In SSR, B_{mix} is the amount of BW which carries the communication information. Hence, the capacity of traditional communication system with a BW B_{mix} is taken for comparison purpose, it follows (4.21) by replacing $\mathcal{B}$ with B_{mix}.

Similar to (4.16), the capacity of SSR in mixed-use band is given by

$$C_{B_{mix}} = \begin{cases} \bar{\epsilon}_1 \quad B_{mix} \ln \left(1 + \frac{P_c}{P_{ww}B_{mix}} \right) \\ \qquad\qquad \text{without SIC scheme} \\ \bar{\epsilon}_2 \quad B_{mix} \ln \left(1 + \frac{P_c}{P_{ww}B_{mix}} \right) \\ \qquad\qquad \text{with SIC scheme} \end{cases} .$$

$$\tag{4.22}$$

Here, $\bar{\epsilon}_1$ and $\bar{\epsilon}_2$ are different from MI calculations of the radar case that are presented in section 4.2.1 B. As the communication perspective is considered here, the radar component is treated as an interference. Therefore, similar to (4.14) and (4.15), the corresponding $\bar{\epsilon}_1$ and $\bar{\epsilon}_2$ is given by

$$\bar{\epsilon}_1 = \frac{P_{ww}}{P_{ww} + 2P_r}, \qquad \bar{\epsilon}_2 = \frac{P_{ww}}{P_{ww} + 2P_r^{res}}. \tag{4.23}$$

Here, $P_r = |X(f)|^2 \sigma_G^2(f)/T$ radar power component, $P_r^{res} = P_r - P_{r_{pre}}$ represents the residual radar power component using SIC scheme in the mixed-use band. In addition, the $\bar{\epsilon}_1$ is approximately equal to zero, as the denominator component has the higher interference (radar power) value compared to the noise power. Which provides reduction in the capacity in mixed-use band, when SIC scheme is not deployed. In contrast, $\bar{\epsilon}_2$ is approximately equal to one, because the denominator component consist of insignificant interference residual component compared to noise power.

4.3 Performance analysis in a multipath environment

In this section, the performance analysis of SSR is presented by considering the multipath. For mathematical simplicity, assume only two paths i.e., $i = 1, 2$. Then the reduced channel model has paths with $w_1(t)$, $w_2(t)$ as noise components. Noise components $w_1(t)$, $w_2(t)$ are jointly Gaussian with zero mean and covariance $K_w = \begin{bmatrix} \sigma_w^2 & \rho\sigma_w^2 \\ \rho\sigma_w^2 & \sigma_w^2 \end{bmatrix}$. Where $\sigma_w^2 = \frac{P_{ww}(f)}{2}$, ρ is the correlation coefficient.

4.3.1 MI in a multipath environment

In this subsection, the multipath is considered in the derivation of MI of the SSR.

A MI in radar-only band

For the radar transmitted waveform $x(t)$, the MI between the target that has response characteristics $g(t)$ and the receiver with the reduced multipath model that has $w_1(t)$, $w_2(t)$ as jointly Gaussian in radar only band is given by (Cover and Thomas, 2012)

$$I_{B_r}(z_r(t); g(t) \mid x(t)) = \frac{1}{2} \ln \left[1 + \frac{2P}{\sigma_{ww}^2(1 + \rho)} \right], \tag{4.24}$$

where P is the power component which represents the target information, is given by $P = \frac{|X(f)|^2 \sigma_G^2(f)}{T}$. After substituting P and σ_{ww}^2 in (4.24), the resulting MI is given by

$$I_{B_r}\left(z_r(t); g(t) \mid x(t)\right) = \frac{1}{2} \ln \left[1 + \frac{4|X(f)|^2 \sigma_G^2(f)}{P_{ww}(f)T(1+\rho)}\right]. \tag{4.25}$$

Using (4.25), the resulting MI $I_{B_r}(z_r(t); g(t) \mid x(t))$, over the radar only band interval $B_r = [f_c, f_c + B_r]$, with multipath effect, is given by

$$I_{B_r}\left(z_r(t); g(t) \mid x(t)\right) = T \int_{B_r} \ln \left[1 + \frac{4|X(f)|^2 \sigma_G^2(f)}{P_{ww}(f)T(1+\rho)}\right] df \,(\text{nats}). \tag{4.26}$$

Similar to (4.8), the maximum MI of $I_{B_r}(z_r(t); g(t) \mid x(t))$ in multipath case, with the constraint on transmitted waveform energy E_x, is given by

$$I_{B_r}^{max}(z_r(t); g(t) \mid x(t)) = TB_r \ln D - T \int_{B_r} \ln \left[r(f)\left(\frac{1+\rho}{2}\right)\right] df \,(\text{nats}). \tag{4.27}$$

The detailed proof of obtaining the maximum $I_{B_r}(z_r(t); g(t) \mid x(t))$ is provided in Appendix A.2.

For different values of correlation coefficient $\rho = 0, 1, -1$, the resulting MI is given by

$$I_{B_r}^{max}\left(z_r(t); g(t) \mid x(t)\right) = \begin{cases} TB_r \ln D - T \int_{B_r} \ln \left[\frac{r(f)}{2}\right] & \text{for } \rho = 0 \\ TB_r \ln D - T \int_{B_r} \ln r(f) & \text{for } \rho = 1 \\ \infty & \text{for } \rho = -1 \end{cases}. \tag{4.28}$$

Here, for $\rho = -1$, the MI $= \infty$ does not mean that one gets the infinite amount of information. Instead, it means that the true/ overall target information has been received. It is true that for $\rho = -1$ case, the noise components $w_1(t)$ and $w_2(t)$ cancel out each other. At the receiver, one has only the true information of the target.

B   MI in mixed-use band

MI in a mixed-use band with multipath holds a similar procedure of MI in a clean environment. The only difference is, instead of using MI of the radar-only band in a clean environment, MI of the radar-only band with multipath defined in (4.27) is used here. The resulting MI similar to (4.16) is given by

$$I_{B_{mix}}^{max}\left(z_r(t); g(t) \mid x(t)\right) \tag{4.29}$$

$$= \begin{cases} \bar{\epsilon}_1 \quad \left(TB_{mix} \ln D - T \int_{B_{mix}} \ln \left[r(f)\left(\frac{1+\rho}{2}\right)\right] df\right) \\ \qquad\qquad\qquad \text{without SIC scheme} \\ \bar{\epsilon}_2 \quad \left(TB_{mix} \ln D - T \int_{B_{mix}} \ln \left[r(f)\left(\frac{1+\rho}{2}\right)\right] df\right) \\ \qquad\qquad\qquad \text{with SIC scheme} \end{cases}$$

Finally, the MI of the SSR with multipath effect is given by

$$I_{B_{\text{SSR}}}^{max}\left(z_r(t); g(t) \mid x(t)\right) = I_{B_r}^{max}(z_r(t); g(t) \mid x(t)) + I_{B_{mix}}^{max}(z_r(t); g(t) \mid x(t)). \quad (4.30)$$

Here $I_{B_r}^{max}$ and $I_{B_{mix}}^{max}$ are defined in (4.27) and (4.29) respectively.

Similar to (4.18), the MI of the traditional radar with multipath is given by

$$I_{B_T}^{max}\left(z_r(t); g(t) \mid x(t)\right) = TB_T \ln D - T \int_{B_T} \ln\left[r(f)\left(\frac{1+\rho}{2}\right)\right] df \text{ (nats)}, \quad (4.31)$$

where D, $r(f)$ is defined in (A.20) and (4.6) respectively.

4.3.2 SE in a multipath environment

The SE of the SSR and traditional radar with multipath is same as (4.19) and (4.20), respectively. The main difference is that $I_{B_{\text{SSR}}}^{\max}$, $I_{B_T}^{\max}$ defined in (4.30), (4.31) is used here, instead of (4.17), (4.18). i.e.,

$$\text{SE}_{SSR} = \frac{I_{B_{\text{SSR}}}^{\max}}{B_{\text{SSR}}} \quad \text{and} \quad \text{SE}_T = \frac{I_{B_T}^{\max}}{B_T + B_{mix}}, \quad (4.32)$$

where $I_{B_{\text{SSR}}}^{\max}$, $I_{B_T}^{\max}$ are defined in (4.30), (4.31).

4.3.3 Capacity (C) in a multipath environment

In this subsection, the channel capacity of SSR in mixed-use band is calculated by considering the multipath effect between the in-band communication transmitter to SSR receiver. The bandlimited Gaussian channel capacity with a BW B_{mix}, effected with $w_1(t)$, $w_2(t)$ jointly Gaussian noise components with zero mean and covariance $K_w = \begin{bmatrix} \sigma_w^2 & \rho\sigma_w^2 \\ \rho\sigma_w^2 & \sigma_w^2 \end{bmatrix}$, $\sigma_w^2 = \frac{P_{ww}}{2}$, correlation coefficient ρ, and power P_c watts is given as Cover and Thomas (2012)

$$C = B_{mix} \ln\left(1 + \frac{2P_c}{P_{ww}B_{mix}(1+\rho)}\right). \quad (4.33)$$

Using (4.33), similar to (4.22), the capacity of SSR in multipath environment is given by

$$C_{B_{mix}} = \begin{cases} \bar{\epsilon}_1 & B_{mix} \ln\left(1 + \frac{2P_c}{P_{ww}B_{mix}(1+\rho)}\right) \\ & \text{without SIC scheme} \\ \bar{\epsilon}_2 & B_{mix} \ln\left(1 + \frac{P_c}{P_{ww}B_{mix}(1+\rho)}\right) \\ & \text{with SIC scheme} \end{cases}.$$

$$(4.34)$$

4.4　Results and discussion

In this section, the numerical results are presented based on the analysis presented in Section 4.2 and 4.3. In this framework, it is assumed that the SSR is operating at 3000MHz with BW of 10MHz. Also, it has the effective antenna area A_e of 2m², and line of sight towards the target at 10km range. The radar transmitter power varies from 50W to 1000W, and pulse duration varies from 0.1ms to 100ms. Here, the target scattering impulse response $g(t)$ has a Gaussian characteristics with spectral variance of $\sigma_G^2(f) = B\exp\{-\delta f^2\}$. Here, B and δ are constant, characterize the magnitude and the rate of decrease of $\sigma_G^2(f)$ (Bell, 1993). The SSR uses 50% of available BW for radar only operation and the rest for mixed-use purpose, unless specified. The additive noise $w(t)$ is white Gaussian having one-sided power spectral density $P_{ww}(f) = N_0 = kT_s$, with Boltzmann constant $k = 1.381 \times 10^{-23}$J/K and system noise temperature $T_s = 300$K. The communication system power varies from 5 W to 1000 W. From (4.14), (4.15), and (4.23), followed by the analysis there deduces the values of $\bar{\epsilon}_1$, $\bar{\epsilon}_2$ information reduction factors without using the SIC scheme and with using the SIC scheme Tian *et al.* (2019*b*), respectively in mixed-use band. Further, it is apparent that the $\bar{\epsilon}_1 \approx 0$ and $\bar{\epsilon}_2 \approx 1$. The same can also be verified for the values considered herein for the noise power, communication power and radar power. For the sake of analysis, $\bar{\epsilon}_1$ and $\bar{\epsilon}_2$ are considered as 0.1 and 0.9 respectively.

4.4.1　Clean environment - using equal BW sharing

The MI of the traditional radar and SSR are plotted in Figure 4.4, as a function of radar average power and pulse duration using (4.17) and (4.18). The power is varied from 50–1000W with a step size of 100W. Similarly, the pulse duration is varied from 0.1 ms to 100 ms with a step size of tenfold. In this analysis, 50% of total BW is allocated for the radar-only band and the rest for the mixed-use band. The MI is observed to increase with the increase in radar transmitted power and radar pulse duration. For a pulse duration of 100ms, it is observed that MI outperforms the other smaller pulse duration values. Similarly, it is observed that, for a given pulse duration, as the average power increase, the MI increases. This is because the higher the power impinges on the target, the more the information received. Further, it is evident from

the results that MI of the traditional radar is always higher than the SSR due to the flexibility of using total available BW for radar-only purpose. Furthermore, in SSR, the influence of using the SIC scheme in the mixed-use band is also depicted in the same Figure 4.4. It is also observed that the MI of SSR, with the SIC, is almost equal to that of the traditional radar because the SIC scheme in the mixed-use band cancels the in-band interference and ensures the maximum information retrieval in that band. Whereas in the absence of the SIC scheme, the target information retrieval becomes less and results in degraded MI of SSR, as shown in the Figure 4.4. This is because of the loss of the target information from the mixed-use band, for an SSR radar, when the SIC scheme is not adopted.
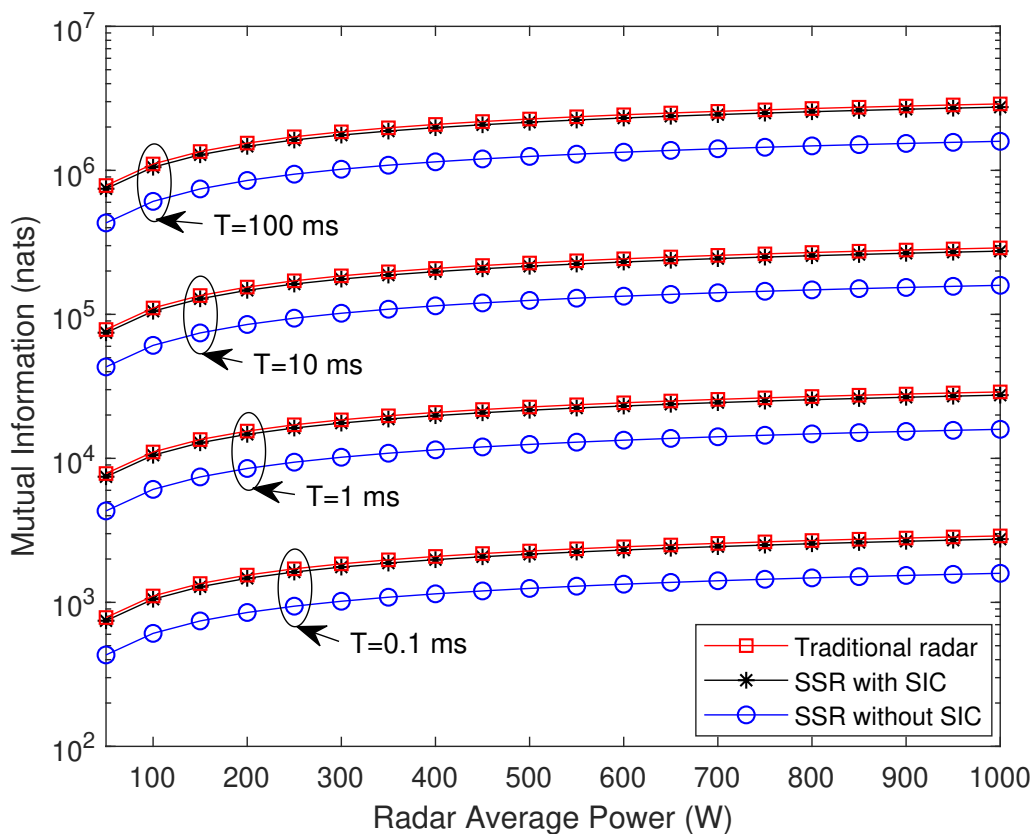
Figure 4.4: MI of SSR as a function of radar power and pulse duration assuming $B_{mix} = 50\%$ of B_{SSR}.

Figure 4.5 shows the SE of the traditional radar and SSR as a function of radar average power and pulse duration with $B_{mix} = 50\%$ of B_{SSR}. The analysis is based on (4.19) and (4.20). It can be observed from Figure 4.5 that the SE is proportional to

the radar transmitted power and radar pulse duration for a given BW. Even though the traditional radar MI is higher than the SSR (refer to Figure 4.4), in the case of SE, the SSR with SIC stands higher than that of traditional radar. This is because the traditional radar accounts for an additional BW of B_{mix} than the SSR for the same amount of information that needs to be obtained. Further, it is observed that the SE of the SSR without SIC is less compared to other schemes, owing to its poor information retrieval in a mixed-use band.
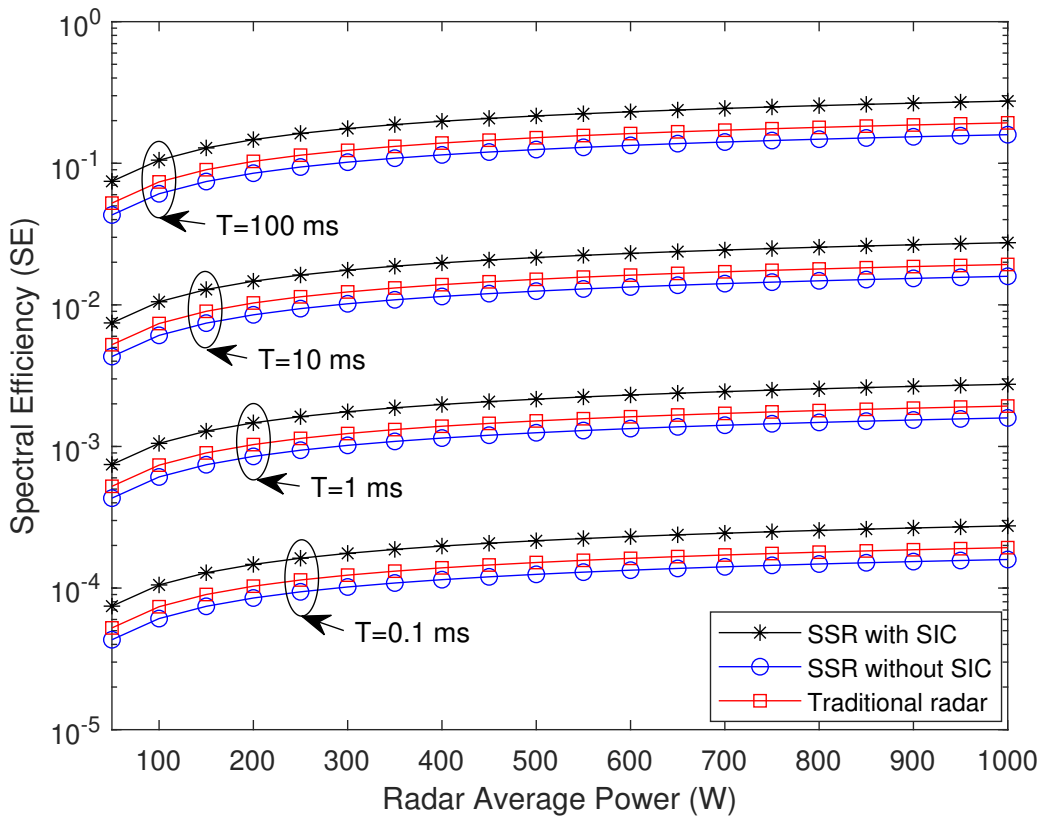
Figure 4.5: SE of SSR as a function of radar power and pulse duration assuming $B_{mix} = 50\%$ of B_{SSR}.

4.4.2 Clean environment - using unequal BW sharing

Figure 4.6 shows the MI of the traditional radar (always the BW is 100%) and SSR with unequal allocated BW (ex. radar band 30% and mixed band 70%). In this analysis, rather than varying the pulse duration, it is fixed to 1 ms, and the figures are plotted using (4.17) and (4.18). Three different BW allocations are considered, namely low mixed band BW (radar band 70% and mixed band 30%), equal BW
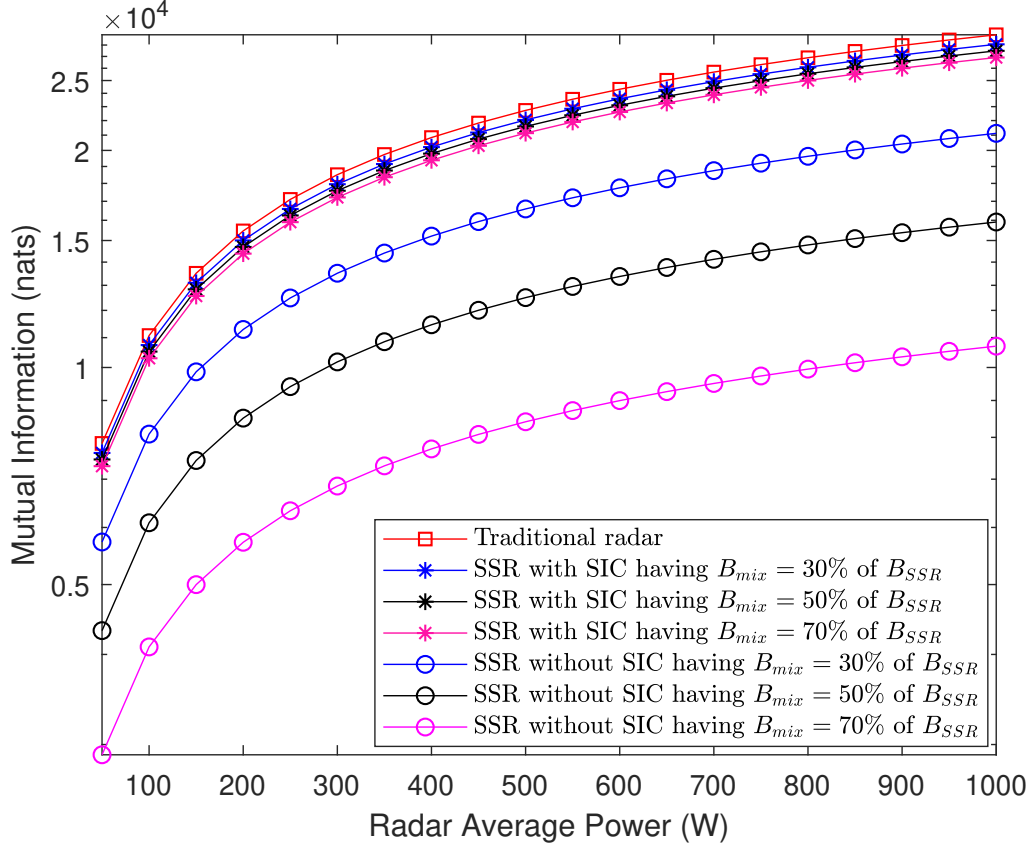
Figure 4.6: MI of SSR as a function of radar power and B_{mix} with a fixed pulse duration of 1ms.

(radar band 50% and mixed band 50%), and high mixed band BW (radar band 30% and mixed band 70%). From Figure 4.6, it is observed that MI of traditional radar outperforms when compared to other cases due to the availability of total BW, and there is no in-band interference exists. Whereas, MI of SSR with the SIC scheme is higher than the MI of SSR without SIC scheme in all the unequal BW sharing cases since the use of SIC scheme in mixed band retrieves more information. As the B_{mix} increases, the MI decreases and vice-versa. In support of this statement, it is clearly observed from Figure 4.6, that the SSR with/without SIC having B_{mix} of 70% attains lesser MI, compared to other cases. It is also worth noting that SSR with SIC also varies dominantly by changing the B_{mix}. But, this is not properly being visualized in the figures due to the $log - y$ scale. The rate of decrease of MI of SSR, with respect to B_{mix}, is less comparable in the case of SSR with the SIC scheme. At the same time, a comparable decrease is found in the case of SSR without the SIC scheme. It is a fact that using larger B_{mix} and not using the SIC scheme in the mixed-use band

leads to more information loss.
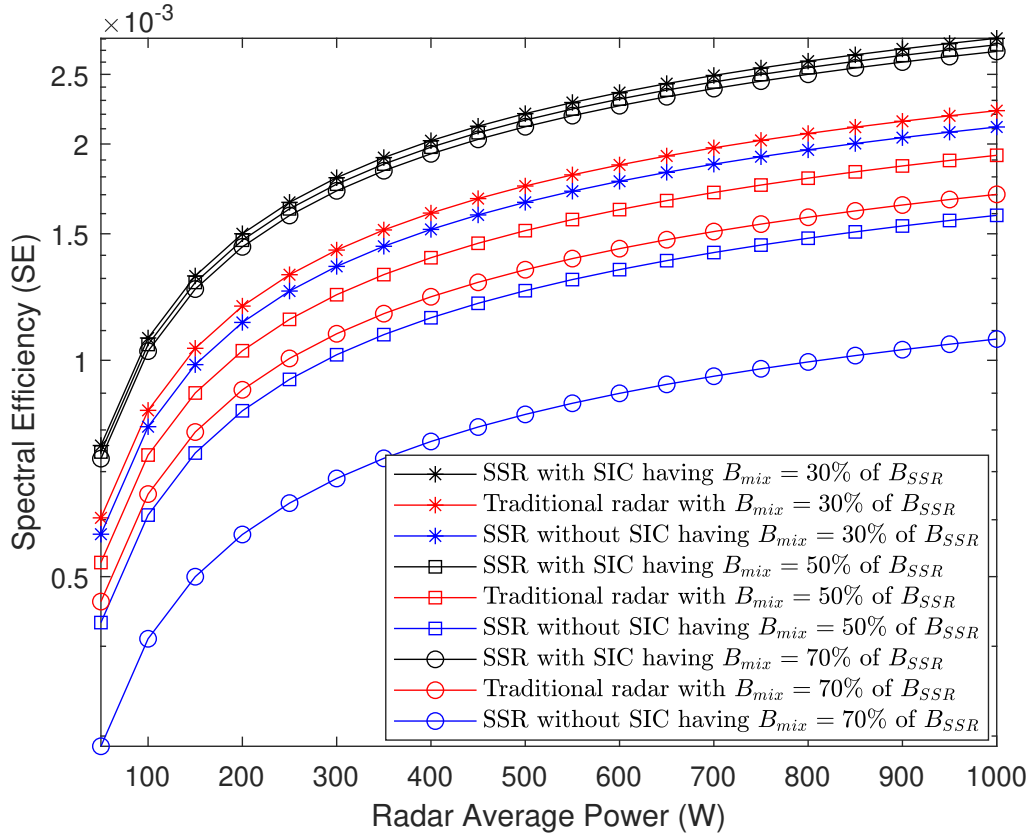
Figure 4.7: SE of SSR as a function of radar power and B_{mix} with fixed pulse duration of 1ms.

Similar to MI of Figure 4.6, the SE analysis is also carried out for traditional radar and SSR, as a function of average radar power, and B_{mix}, with a fixed pulse duration of 1 ms. Figure 4.7 shows the SE with unequal BW allocation, and is obtained based on (4.19) and (4.20). For the $B_{mix} = 30\%$, 50%, 70% of B_{SSR}, the denominator of (4.20) becomes $1.3B_T$, $1.5B_T$, and $1.7B_T$ respectively. It is observed that the SE of SSR, with the SIC scheme, is higher than the traditional radar case and SSR without the SIC case. In all the three proportions of mixed-use BW allocation (for $B_{mix} = 30\%$, 50%, 70% of B_{SSR}), the order of the SE follows SE with SIC > SE of traditional radar > SE without SIC. The SE without SIC scheme falls below the other two cases (SE with SIC and traditional radar) in their corresponding proportion of allocated mixed-use BW. Further, it is noted that the allocation of more amount of BW ($B_{mix} = 70\%$ of B_{SSR}) to the mixed-use band leads to the less SE of SSR

without SIC case. Because the allocation of a high portion of total available BW for the mixed-use band and not being able to use the SIC scheme will result in considerable information loss, which inturn reflects on SE.

4.4.3 Impact of multipath in SSR

In the above Subsections, 4.4.1 and 4.4.2, the case of a clean environment is considered, and a detailed discussion is given on the impact of radar power, pulse duration, and allocation of unequal BW in SSR. The results obtained (Figures 4.4 to 4.7) in those sections hold true for multipath case. Hence, the Figures are avoided and summarize the results about multipath cases. In summary, the MI and SE increase with average radar power and pulse duration in multipath cases. Similarly, MI of traditional radar is higher than the SSR configuration, and SE of SSR is higher than the traditional radar. These results are not plotted again for the multipath case to eliminate the redundancy. Instead, the comparison results of clean environment and multipath environment are provided.

Figure 4.8 depicts the comparison of MI in a clean and multipath environment for both traditional and SSR, based on (4.17), (4.18), (4.30), and (4.31). Here, the $B_{mix} = 50\%$ of B_{SSR}, and a fixed pulse duration of 1ms is considered. The impact of the correlation coefficient ρ is analysed. It is observed that the MI of traditional radar and SSR with $\rho = 0$ is dominating compared to $\rho = 1$. This domination of SSR is theoretically true. Because, for $\rho = 0$, the jointly Gaussian noise components $w_1(t)$, $w_2(t)$ of two paths act as independent paths. Hence, the multipath target-to-receiver channel act like two looks Gaussian channel (Cover and Thomas, 2012). Therefore, the receiver has additional target information from multiple paths. Next, the MI of traditional and SSR in a multipath environment for $\rho = 1$ is equal to that of a clean environment. For $\rho = 1$, the multipath target-to-receiver channel acts like a single look Gaussian channel, same as the clean environment target-to-receiver channel model.

Figure 4.9 shows the comparison of SE of SSR and traditional radar in both clean and multipath environment having $B_{mix} = 50\%$ of B_{SSR} and a fixed pulse duration of 1ms. The results are obtained using (4.19), (4.20), (4.32). Similar to Figure 4.8, it is observed that SE of traditional and SSR for $\rho = 0$ is higher compared to $\rho = 1$.
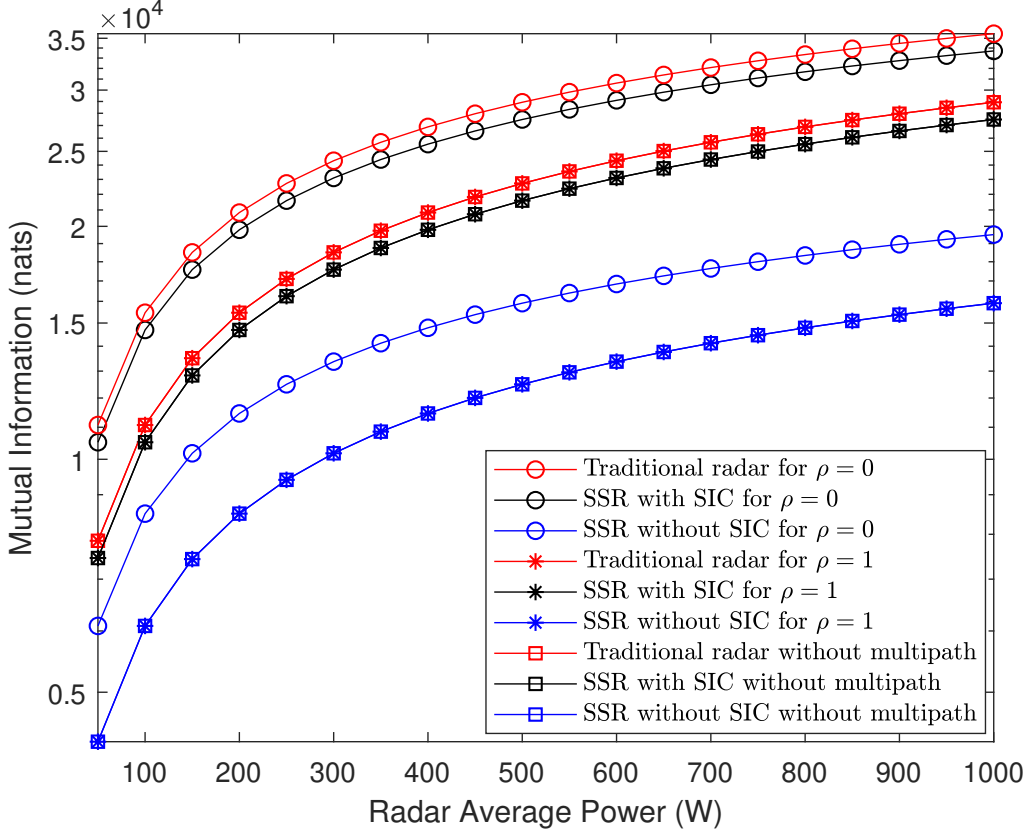
Figure 4.8: Comparison of MI of SSR for clean and multipath environment
($B_{mix} = 50\%$ of B_{SSR} and $T = 1$ms).

Similarly, the SE for $\rho = 1$ case is equal to the SE of clean environment. Since the SE is directly proportional to MI, the change in MI directly reflects in SE.

Figure 4.10 shows the performance analysis of SSR from communication point of view by considering the capacity as a metric for performance evaluation. It shows the comparison between the capacity of SSR and the capacity of traditional communication system in both clean and multipath environment having $B_{mix} = 50\%$ of B_{SSR}. The results are obtained using (4.22) and (4.34). Similar to Figure 4.8, 4.9, it is observed that the capacity of traditional communication system and SSR mode of operation for $\rho = 0$ is higher compared to $\rho = 1$. Because, for $\rho = 0$, both the paths become independent and contribute to the capacity constructively. Similarly, the capacity for $\rho = 1$ case is equal to the capacity of clean environment. Unlike MI and SE, the capacity of SSR with SIC and without SIC are considerably separated due to suppression of the interference by the SIC scheme. It is because the communication system capacity is only available in the mixed-use band. However, for the MI and SE
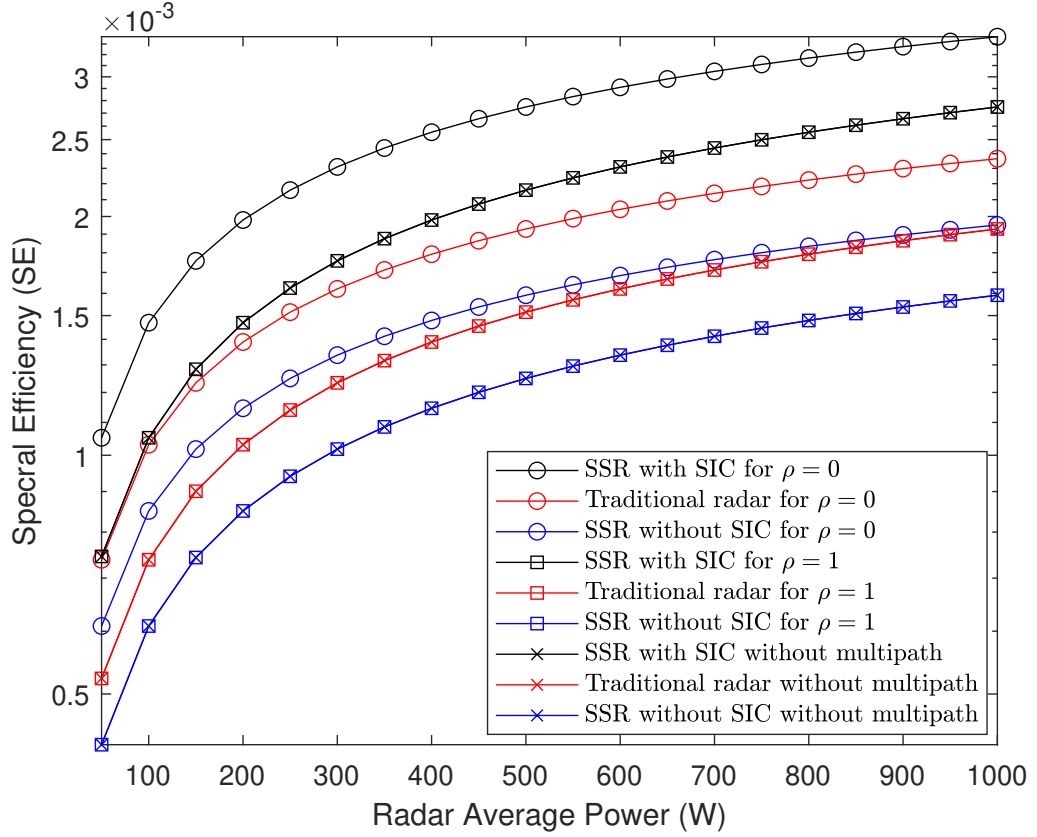
Figure 4.9: Comparison of SE of SSR for clean and multipath environment ($B_{mix} = 50\%$ of B_{SSR} and $T = 1$ms).

metrics, both radar only band and mixed-use band contribute the target information.

Figure 4.11 shows the comparison of MI, SE, and capacity (C) of SSR with traditional systems by varying the mean ϵ. This figure also shows the impact of residual and direct interference components on the performance metrics MI, C, and SE. The Figure 4.11 is based on the generalized MI of SSR represented in (4.10) and its similar forms for SE and C. Let mean $\epsilon \approx 0$ is the SSR without SIC region or $\bar{\epsilon}_1$ region or direct interference region. Let mean $\epsilon \approx 1$ is the SSR with SIC region or $\bar{\epsilon}_2$ region or residual interference region. The region between these two direct and residual interference regions can be interpreted as a transition region. From (4.14), (4.15), and (4.23), the $\bar{\epsilon}_1$, $\bar{\epsilon}_2$ are related to direct and residual interference components, varying these quantities or observing the performance of SSR in the corresponding regions automatically quantifies the effect of direct and residual interference. It is observed that, the performance of the SSR without SIC region falls short when compared to traditional systems. However, it align with the traditional system with SIC region
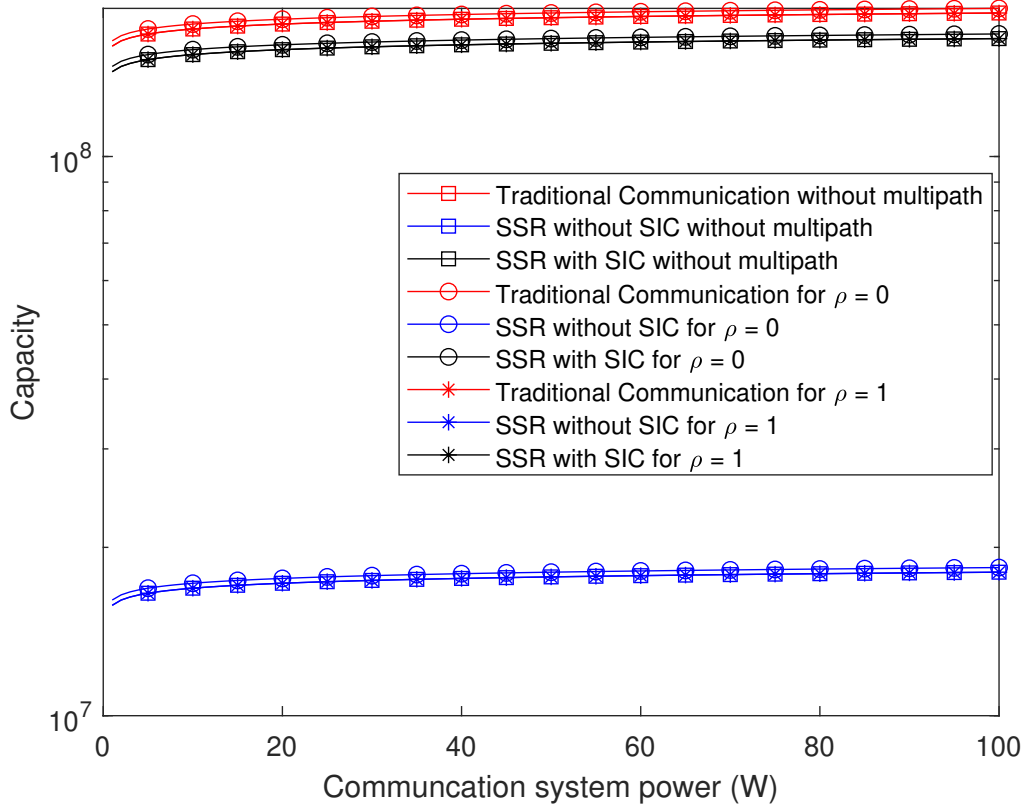
Figure 4.10: Comparison of capacity of SSR for clean and multipath environment $(B_{mix} = 50\% \text{ of } B_{SSR})$

for MI and C metrics. It is because, the SSR without SIC region is the region where the direct interference will be present (referencing to (4.14) and (4.23)), which in turn deteriorates the information retrieval. Whereas in $\bar{\epsilon}_2$ region, the SSR uses the SIC scheme, results into the residual interference (referencing to (4.15) and (4.23)), which allows the better information reception. Further, the SSR provides improved performance for SE metric. The SE of SSR in without SIC region is similar to the SE of traditional system and SE of SSR with SIC scheme is superior compared with traditional systems.
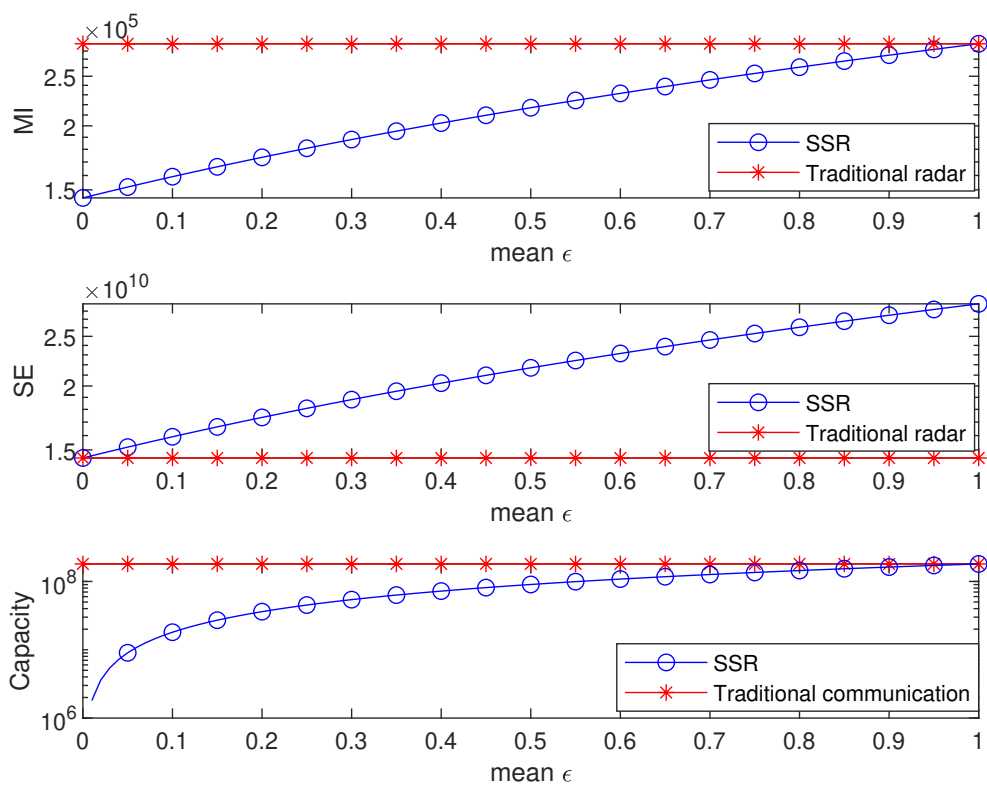
Figure 4.11: Comparison of MI, SE, and capacity (C) of SSR with varying mean ϵ

Chapter 5

Target Estimation Performance Improvement in Cooperative Radar and Communication System Spectrum Sharing

Considering the cooperative radar and communication system (RadComm) spectrum sharing systems (which use the target reflected signals due to communication transmitters), this Chapter presents the target estimation performance in terms of Cramer-Rao Lower Bound (CRLB) as a performance metric. To show the efficacy of the cooperative nature of RadComm spectrum sharing, the target estimation performance is also evaluated for the case of non-cooperative RadComm spectrum sharing and stand-alone radar system operation case. Results show that the cooperative RadComm spectrum sharing provides an improved performance compared to non-cooperative and stand-alone operations.

5.1 Cooperative RadComm spectrum sharing system model

The system model of cooperative RadComm spectrum sharing is shown in Figure 5.1, where a mono-static radar is detecting the targets present in its surveillance is considered. The radar target surveillance region also has coverage with spectrum sharing communication system transmitter is illustrated. For simplicity, a single communication transmitter and a single target are considered. Along with the target reflections from the radar transmission, the radar also receives the direct and the target reflected

signals, owing to the in-band communication transmitter. The cooperation between the radar and communication system allows them to share the transmit signal information and location, which helps the radar receiver decode the communication signals and extract the target information contributed by both radar and communication systems.

Target

Monostatic Radar

Comm Tx

Radar return predction

Radar return processing

Decode Comm sig and reomove
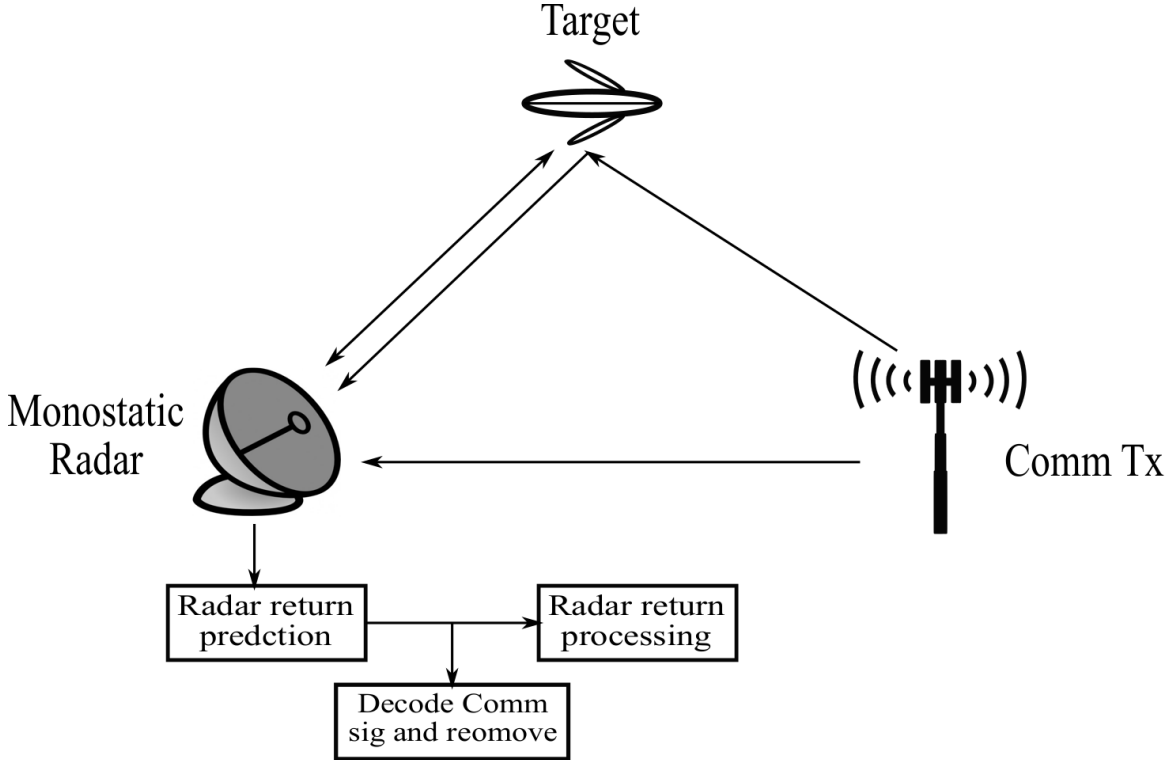
Figure 5.1: Cooperative radar and communication system model.

Let, $S_{T_R}(k)$, $S_{T_C}(k)$ are the transmitted signals by the radar and communication system at time instant kT_s, given by

$$S_{T_R}[k] = a_R s_R(kT_s), \tag{5.1}$$

$$S_{T_C}[k] = a_C s_C(kT_s), \tag{5.2}$$

where $a_{(.)}$ is the amplitude, and is equal to the square root of energy of the corresponding signal $\left(\text{i.e., } a_{(.)} = \sqrt{E_{(.)}}\right)$, $k = 1, 2, \ldots K$ is the sampling index and T_s is the sampling time.

5.1.1 Received Signal Model

Due to the presence of spectrum sharing communication transmitter, the received signal at the radar receiver, at time instant kT_s, is given by

$$S_{R_R}[k] = \sigma_{t,R} a_R s_R(kT_s - \tau_{t,R}) + \sigma_{t,C} a_C s_C(kT_s - \tau_{t,C})$$
$$+ a_C s_C(kT_s - \tau_C) + w[k]. \qquad (5.3)$$

The first two terms in (5.3) represent the target returns due to radar and communication transmitter, whereas the last terms correspond to direct signal from a communication transmitter. The $\tau_{t,R}$, $\tau_{t,C}$, and τ_C represent the corresponding time delays. The $\sigma_{t,R}$, $\sigma_{t,C}$ are the target reflection coefficients, contributed by radar and communication transmitters. The $w[k]$ indicates the noise component and is assumed as zero-mean Gaussian, with covariance $\mathbf{Q}_w$.

The overall received signal vector at the radar receiver is

$$\mathbf{S}_{R_R} = (S_{R_R}[1], S_{R_R}[2], \dots, S_{R_R}[K])'$$
$$= U_{t,R}\mathbf{s}_{t,R} + U_{t,C}\mathbf{s}_{t,C} + U_C\mathbf{s}_C + \mathbf{w}, \qquad (5.4)$$

where

$$U_{t,R} = \sigma_{t,R} a_R, \quad U_{t,C} = \sigma_{t,C} a_C, \quad U_c = a_C,$$
$$\mathbf{s}_{t,R} = [s_R(T_s - \tau_{t,R}), s_R(2T_s - \tau_{t,R}), \dots, s_R(KT_s - \tau_{t,R})]',$$
$$\mathbf{s}_{t,C} = [s_C(T_s - \tau_{t,C}), s_C(2T_s - \tau_{t,C}), \dots, s_C(KT_s - \tau_{t,C})]',$$
$$\mathbf{s}_C = [s_C(T_s - \tau_C), s_C(2T_s - \tau_C), \dots, s_C(KT_s - \tau_C)]',$$
$$\mathbf{w} = [w[1], w[2], \dots, w[K]]'.$$

5.2 Target estimation performance in terms of CRLB

This section presents the CRLB derivation for cooperative, non-cooperative Rad-Comm spectrum sharing and stand-alone radar system operation.

5.2.1 Cooperative case

The target state assumed is two dimensional, having a state vector $\mathbf{x} = [x \ y]'$ and the task of the radar is to estimate its position. The cooperation between the communication and radar system allows the communication system to share the complete

statistics of the communication signal (i.e., $\mathbf{s}_C = [s_C[T_s], s_C[2T_s], \ldots, s_C[KT_s]]')$ with the radar. This helps the radar to utilise the target reflected signals, owing to the communication transmitter to detect target statistics, which improves the target estimation performance. The likelihood function based on the received signal (5.4), with the assumption that the communication signals are decoded, is given by

$$p(\mathbf{S}_{R_R}|\mathbf{x}, \mathbf{s}_C) = \frac{1}{\pi^K \det(\mathbf{Q}_w)} \exp\{-\mathbf{Z}^H \mathbf{Q}_w^{-1} \mathbf{Z}\}, \tag{5.5}$$

where

$$\mathbf{Z} = \mathbf{S}_{R_R} - U_{t,R} \mathbf{s}_{t,R} - U_{t,C} \mathbf{s}_{t,C} - U_C \mathbf{s}_C \tag{5.6}$$

The corresponding log-likelihood function of (5.5) is

$$\ln\{p(\mathbf{S}_{R_R}|\mathbf{x}, \mathbf{s}_C)\} \propto -\mathbf{Z}^H \mathbf{Q}_w^{-1} \mathbf{Z} \tag{5.7}$$

Therefore, the maximum likelihood (ML) estimate of the target state $\mathbf{x}$ is obtained using

$$\hat{\mathbf{x}} = \arg \max_{\mathbf{x}} \ln \{p(\mathbf{S}_{R_R}|\mathbf{x}, \mathbf{s}_C)\} \tag{5.8}$$

To compute the CRLB, an intermediate vector $\boldsymbol{\Theta}$ is defined as

$$\boldsymbol{\Theta} = [\tau_{t,R}, \ \tau_{t,C}, \theta_{t,R}, \theta_{t,C}], \tag{5.9}$$

where $(\tau_{t,R}, \ \theta_{t,R})$, and $(\tau_{t,C}, \ \theta_{t,C})$ is the target range, angle information corresponds to radar and communication system, given by

$$\tau_{t,R} \propto \sqrt{(x - x_R)^2 + (y - y_R)^2} = r_R, \tag{5.10}$$

$$\tau_{t,C} \propto \sqrt{(x - x_R)^2 + (y - y_R)^2} + \sqrt{(x - x_C)^2 + (y - y_C)^2} = r_R + r_C, \tag{5.11}$$

$$\theta_{t,R} = \theta_{t,C} = \arctan\left(\frac{y - y_R}{x - x_R}\right). \tag{5.12}$$

Here, $(x_R, \ y_R)$, $(x_C, \ y_C)$ are radar and communication system transmitter locations, respectively, and are assumed to be known.

The Fisher information matrix (FIM) for the target estimate of $\mathbf{x}$ is

$$\mathbf{FIM} = (\nabla_{\mathbf{x}} \boldsymbol{\Theta})' \mathbf{J}(\boldsymbol{\Theta})(\nabla_{\mathbf{x}} \boldsymbol{\Theta}), \tag{5.13}$$

where,

$$\nabla_{\mathbf{x}}\mathbf{\Theta} = \begin{pmatrix} \frac{\partial \tau_{t,R}}{\partial x} & \frac{\partial \tau_{t,R}}{\partial y} & \frac{\partial \tau_{t,C}}{\partial x} & \frac{\partial \tau_{t,C}}{\partial y} \\ \frac{\partial \theta_{t,R}}{\partial x} & \frac{\partial \theta_{t,R}}{\partial y} & \frac{\partial \theta_{t,C}}{\partial x} & \frac{\partial \theta_{t,C}}{\partial y} \end{pmatrix} = \begin{pmatrix} \mathbf{C} & \mathbf{D} \end{pmatrix} \tag{5.14}$$

and

$$\mathbf{J}(\mathbf{\Theta}) = \Re\left(\frac{\partial (U_{t,R}\mathbf{s}_{t,R} + U_{t,C}\mathbf{s}_{t,C})'}{\partial \mathbf{\Theta}} \mathbf{Q}_w^{-1} \frac{\partial (U_{t,R}\mathbf{s}_{t,R} + U_{t,C}\mathbf{s}_{t,C})}{\partial \mathbf{\Theta}}\right), \tag{5.15}$$

where $\Re\{\cdot\}$ represents real operator.

From, (5.10), (5.11), (5.12), and (5.14), the $\mathbf{C}$ and $\mathbf{D}$ are calculated as

$$\mathbf{C} = \begin{pmatrix} \frac{x-x_R}{r_R} & \frac{y-y_R}{r_R} \\ \frac{-(y-y_R)}{r_R^2} & \frac{x-x_R}{r_R^2} \end{pmatrix} \tag{5.16}$$

$$\mathbf{D} = \begin{pmatrix} \frac{x-x_R}{r_R} + \frac{x-x_C}{r_C} & \frac{y-y_R}{r_R} + \frac{y-y_C}{r_C} \\ \frac{-(y-y_R)}{r_R^2} & \frac{x-x_R}{r_R^2} \end{pmatrix} \tag{5.17}$$

Using (5.15) and (5.14), (5.13) is written as

$$\mathbf{FIM} = \mathbf{C}'\mathbf{J}_{t,R}\mathbf{Q}_w^{-1}\mathbf{J}_{t,R}'\mathbf{C} + \mathbf{D}'\mathbf{J}_{t,C}\mathbf{Q}_w^{-1}\mathbf{J}_{t,R}'\mathbf{C}$$
$$+ \mathbf{C}'\mathbf{J}_{t,R}\mathbf{Q}_w^{-1}\mathbf{J}_{t,C}'\mathbf{D} + \mathbf{D}'\mathbf{J}_{t,C}\mathbf{Q}_w^{-1}\mathbf{J}_{t,C}'\mathbf{D}. \tag{5.18}$$

Here,

$$\mathbf{J}_{t,R} = \frac{\partial (U_{t,R}\mathbf{s}_{t,R})}{\partial \tau_{t,R}} \propto \sigma_{t,R}\sqrt{E_R} \tag{5.19}$$

$$\mathbf{J}_{t,C} = \frac{\partial (U_{t,C}\mathbf{s}_{t,C})}{\partial \tau_{t,C}} \propto \sigma_{t,C}\sqrt{E_C} \tag{5.20}$$

In $\mathbf{J}_{t,R}$, $\mathbf{J}_{t,C}$, only amplitude components are considered, with the assumption that the focus is not on waveform design; therefore, without loss of generality, signal components are assumed to be one.

Finally, from (5.18), the CRLB for the case of cooperative RadComm spectrum sharing is given by (Bar-Shalom *et al.*, 2004)

$$\text{CRLB} = \mathbf{FIM}^{-1}. \tag{5.21}$$

5.2.2 Non-cooperative case

From (5.4), the received signal at the radar receiver is given by

$$\mathbf{S}_{R_R} = U_{t,R}\mathbf{s}_{t,R} + U_{t,C}\mathbf{s}_{t,C} + U_C\mathbf{s}_C + \mathbf{w}. \tag{5.22}$$

Owing to the non-cooperative nature of RadComm spectrum sharing, the radar system receiver cannot interpret and make use of target reflected signals from the communication transmitter and assumes it as an additional noise component and processes further. Therefore, (5.22) is modified to

$$\mathbf{S}_{R_R} = U_{t,R}\mathbf{s}_{t,R} + \mathbf{w}_C + \mathbf{w}. \tag{5.23}$$

Here, it is assumed that $\mathbf{w}_C$ is also a zero-mean Gaussian with covariance $\mathbf{Q}_C$. The assumption of Gaussianity is made based on the principle of Central limit theorem (Abramowitz and Stegun, 1948).

Similar to (5.5), the likelihood function for this case is

$$p(\mathbf{S}_{R_R}|\mathbf{x}) = \frac{1}{\pi^K \det(\mathbf{Q}_C + \mathbf{Q}_w)} \exp\{-\mathbf{Z}^H(\mathbf{Q}_C + \mathbf{Q}_w)^{-1}\mathbf{Z}\}, \tag{5.24}$$

where

$$\mathbf{Z} = \mathbf{S}_{R_R} - U_{t,R}\mathbf{s}_{t,R} \tag{5.25}$$

The corresponding log likelihood function is

$$\ln\{p(\mathbf{S}_{R_R}|\mathbf{x})\} \propto -\mathbf{Z}^H(\mathbf{Q}_C + \mathbf{Q}_w)^{-1}\mathbf{Z} \tag{5.26}$$

The corresponding target estimate follows

$$\hat{\mathbf{x}} = \arg \max_{\mathbf{x}} \ln\{p(\mathbf{S}_{R_R}|\mathbf{x})\} \tag{5.27}$$

The FIM follows the similar form of (5.13), with changes in $\mathbf{\Theta}$, $\nabla_{\mathbf{x}}\mathbf{\Theta}$, $\mathbf{J}(\mathbf{\Theta})$, given by (since the contributions from the communication system have not been exploited due to its non-cooperative nature, the terms contributed by the communication transmitter are removed in comparison with the cooperative case)

$$\mathbf{\Theta} = [\tau_{t,R}, \ \theta_{t,R}], \tag{5.28}$$

$$\nabla_{\mathbf{x}}\boldsymbol{\Theta} = \begin{pmatrix} \frac{\partial \tau_{t,R}}{\partial x} & \frac{\partial \tau_{t,R}}{\partial y} \\ \frac{\partial \theta_{t,R}}{\partial x} & \frac{\partial \theta_{t,R}}{\partial y} \end{pmatrix} = \mathbf{C}, \tag{5.29}$$

and

$$\mathbf{J}(\boldsymbol{\Theta}) = \Re\left\{ \frac{\partial (U_{t,R}\mathbf{s}_{t,R})'}{\partial \boldsymbol{\Theta}} (\mathbf{Q}_C + \mathbf{Q}_w)^{-1} \frac{\partial (U_{t,R}\mathbf{s}_{t,R})}{\partial \boldsymbol{\Theta}} \right\}, \tag{5.30}$$

Using (5.30) and (5.29), similar to (5.18), the FIM follows

$$\mathbf{FIM} = \mathbf{C}'\mathbf{J}_{t,R}(\mathbf{Q}_C + \mathbf{Q}_w)^{-1}\mathbf{J}'_{t,R}\mathbf{C}. \tag{5.31}$$

Here,

$$\mathbf{J}_{t,R} = \frac{\partial (U_{t,R}\mathbf{s}_{t,R})}{\partial \tau_{t,R}}. \tag{5.32}$$

Finally, the CRLB for the case of non-cooperative RadComm spectrum sharing is given by (Bar-Shalom *et al.*, 2004)

$$\mathrm{CRLB} = \mathbf{FIM}^{-1}, \tag{5.33}$$

where **FIM** is given in (5.31).

5.2.3 Stand-alone case

In this case, it is assumed that radar does not share any spectrum with the communication system and operates in a stand-alone fashion. Similar to (5.4) and (5.23), the received signal model for this case is given by

$$\mathbf{S}_{R_R} = U_{t,R}\mathbf{s}_{t,R} + \mathbf{w}. \tag{5.34}$$

The corresponding target estimate follows the similar form of (5.27), with a modified log-likelihood function, given by

$$\ln\{p(\mathbf{S}_{R_R}|\mathbf{x})\} \propto -\mathbf{Z}^H\mathbf{Q}_w^{-1}\mathbf{Z}, \tag{5.35}$$

where **Z** is defined in (5.25).

Similar to (5.21) and (5.33), the CRLB for the case of stand alone radar system operation is given by

$$\mathrm{CRLB} = (\mathbf{C}'\mathbf{J}_{t,R}\mathbf{Q}_w^{-1}\mathbf{J}'_{t,R}\mathbf{C})^{-1}, \tag{5.36}$$

where $\mathbf{C}$ is defined in (5.29), $\mathbf{J}_{t,R}$ is given in (5.32), $\mathbf{Q}_w$ is the covariance of the noise component.

For the case of the target in motion, the CRLB at a particular instant is equal to the inverse of the summation of all the FIMs up to that instant, defined as (Bar-Shalom *et al.*, 2004)

$$\text{CRLB}[KT_s] = \left(\sum_{k=1}^{K} \mathbf{FIM}_k \right)^{-1}. \tag{5.37}$$

To compare the target estimation performance of all the three cases, the square root CRLB (SRCRLB) is used, given by

$$\text{SRCRLB} = \sqrt{\text{Tr(CRLB)}}, \tag{5.38}$$

where $\text{Tr}(\cdot)$ represents the trace of a matrix, CRLB for the three cases is given in (5.21), (5.33), and (5.36).

5.3 Results and discussion

A monostatic radar is considered to detect a target over a surveillance region of $7000 \times 7000\text{m}^2$, with a maximum detectable range of 7000m. Also, a spectrum-sharing communication transmitter is present in the surveillance region. Both the radar and communication system are assumed to be static and located at $(500, 700)\text{m}$ and $(2000, 2000)\text{m}$, respectively. A single target is assumed in the surveillance region, with the initial position at $(1100, 1700)\text{m}$ and travels with a velocity of 100m/s in both x and y directions. The simulation scenario is shown in Figure 5.2. Assume that the total energy of E is split between the radar and communication system with a parameter α as $E_R = \alpha E$, $E_C = (1 - \alpha)E$. Also, the target radar cross-section (RCS) looked by the radar and communication system varies with parameter β as $\sigma_{t,R} = \beta\sigma^2$, $\sigma_{t,C} = (1 - \beta)\sigma^2$. The $\alpha \in [0,1]$ and $\beta \in [0,1]$. The α and β values quantify the target estimation performance with respect to transmit energy and target reflection coefficient, respectively. The RCS of the target is assumed to be 2m^2. The covariances Q_w and Q_C are assumed to be equal. The range and azimuth are corrupted with white Gaussian noise, with standard deviation 10m and 10^{-3}rad, respectively. For the assumptions made, based on (5.21), (5.33), (5.36), (5.37), and (5.38), the Figures 5.3 and 5.4 compare the static target estimation performance for

all three cases, with varying α and β. Whereas Figure 5.5 shows the dynamic target estimation performance in terms of square root CRLB. For static target assumption, (5.21), (5.33), (5.36) is used and SRCRLB is calculated using (5.38). For the target in motion, (5.37) is considered before proceeding to (5.38) of SRCRLB evaluation.
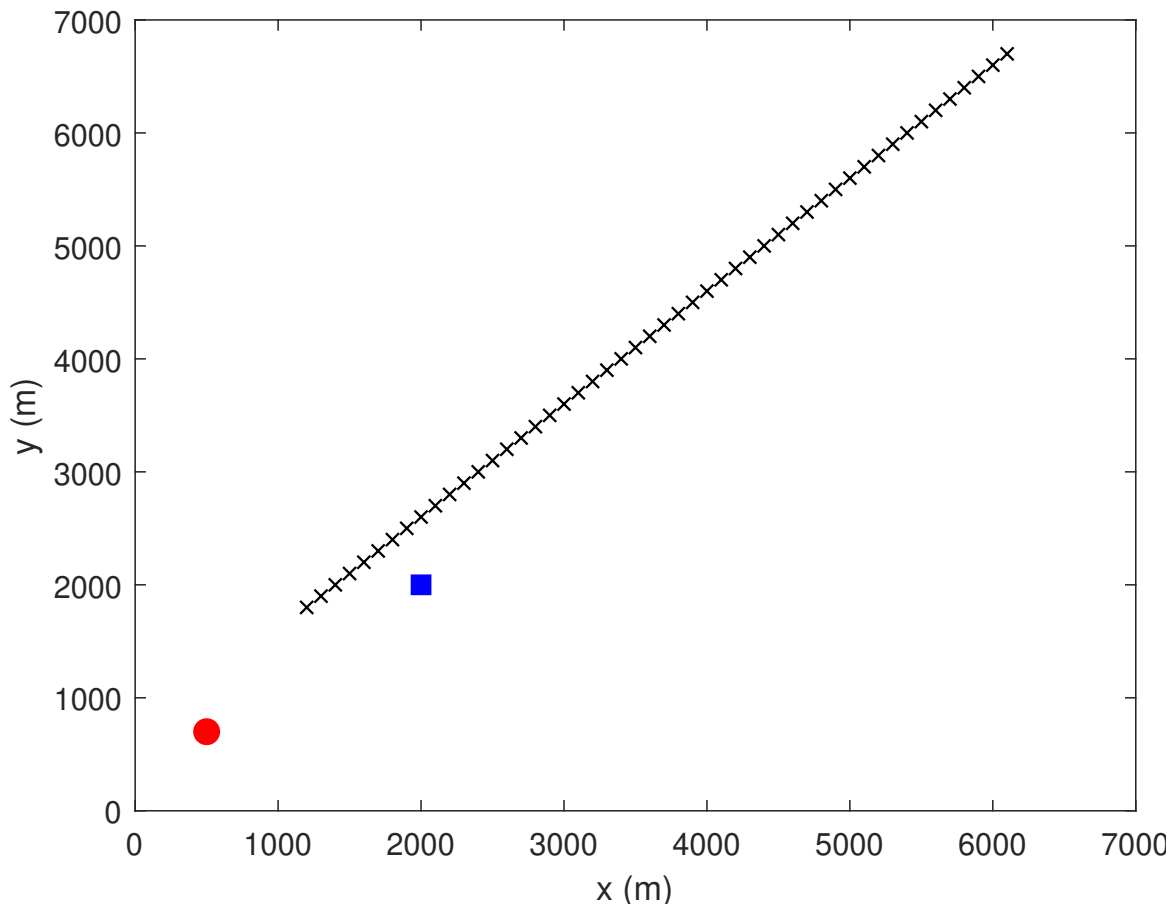
Figure 5.2: Scenario generation (The red circle indicates the radar transmitter, the blue square represents the communication system transmitter, and the black plus symbols mimic the target path).

It is observed from Figure 5.3 by varying the α; the SRCRLB is improved in all three cases. It is because increasing α increases the radar transmitter power, which in turn improves the target return information, which leads to a decrease in the SRCRLB. The cooperative radar configuration provides nearly twofold improvement compared to that of non-cooperative configuration. At the same time, the standalone configuration outperforms the non-cooperative configuration for all the values of α. This is because of the presence of unintended information in the non-cooperative mode. Interestingly, the cooperative and standalone provide the same performance

at $\alpha = 1$ because the cooperative RadComm system operates at its maximum radar transmitting power.
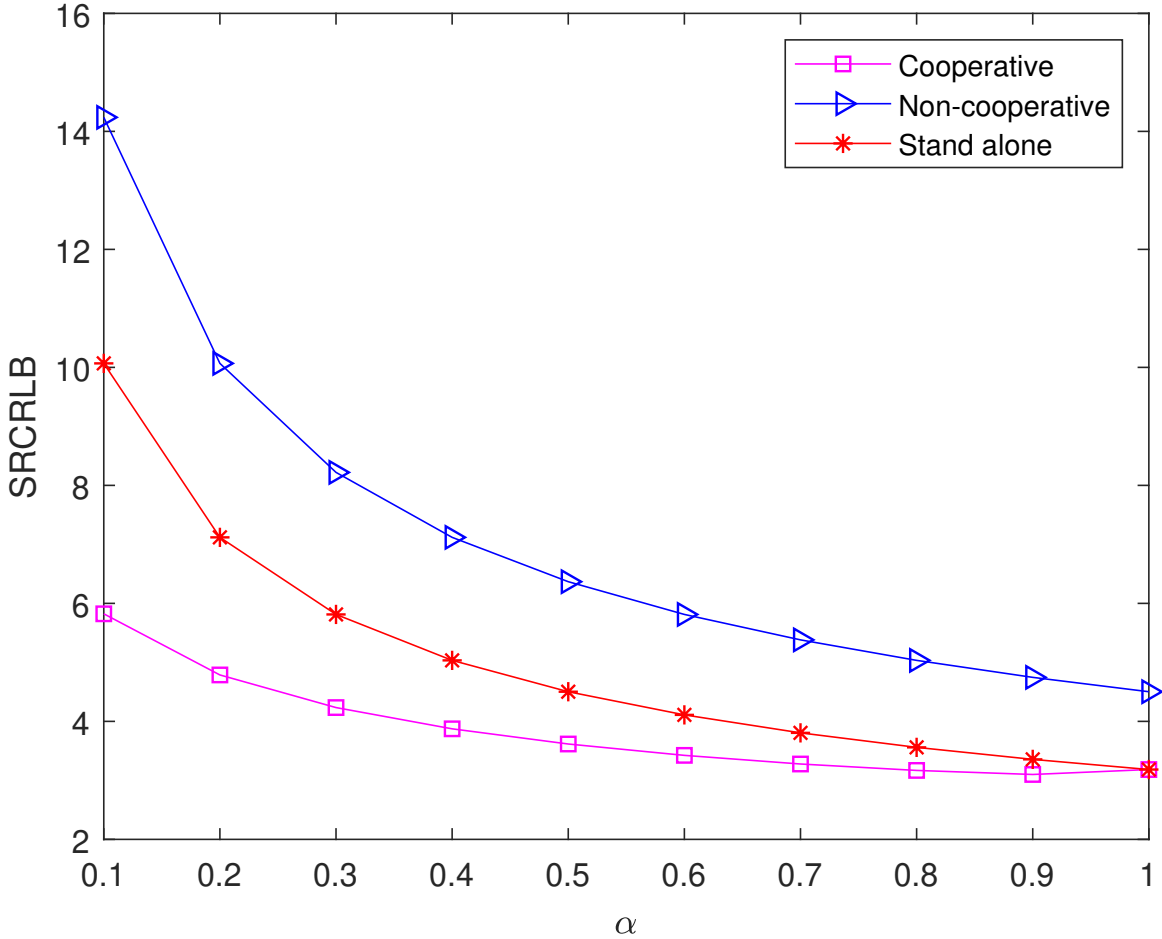
Figure 5.3: The static target estimation performance with varying α.

From Figure 5.4, it is observed that as β varies from 0 to 1, the SRCRLB is improved in all three cases. The increase in β increases the RCS of target return seen by radar, which improves the target estimation performance. The cooperative case provides more than twofold improvement, compared to that of the non-cooperative case, until $\beta = 0.5$, and thereafter the values are constant and comparable. Whereas the standalone radar operation outperforms the non-cooperative case, for all the values of β, this is because of the unused information present in the non-cooperative mode. The cooperative and standalone case provides the same performance after $\beta = 0.5$, with no parameter influence.

Figure 5.5 shows the target estimation performance improvements that the cooperation between the radar and the communication system is bringing in RadComm
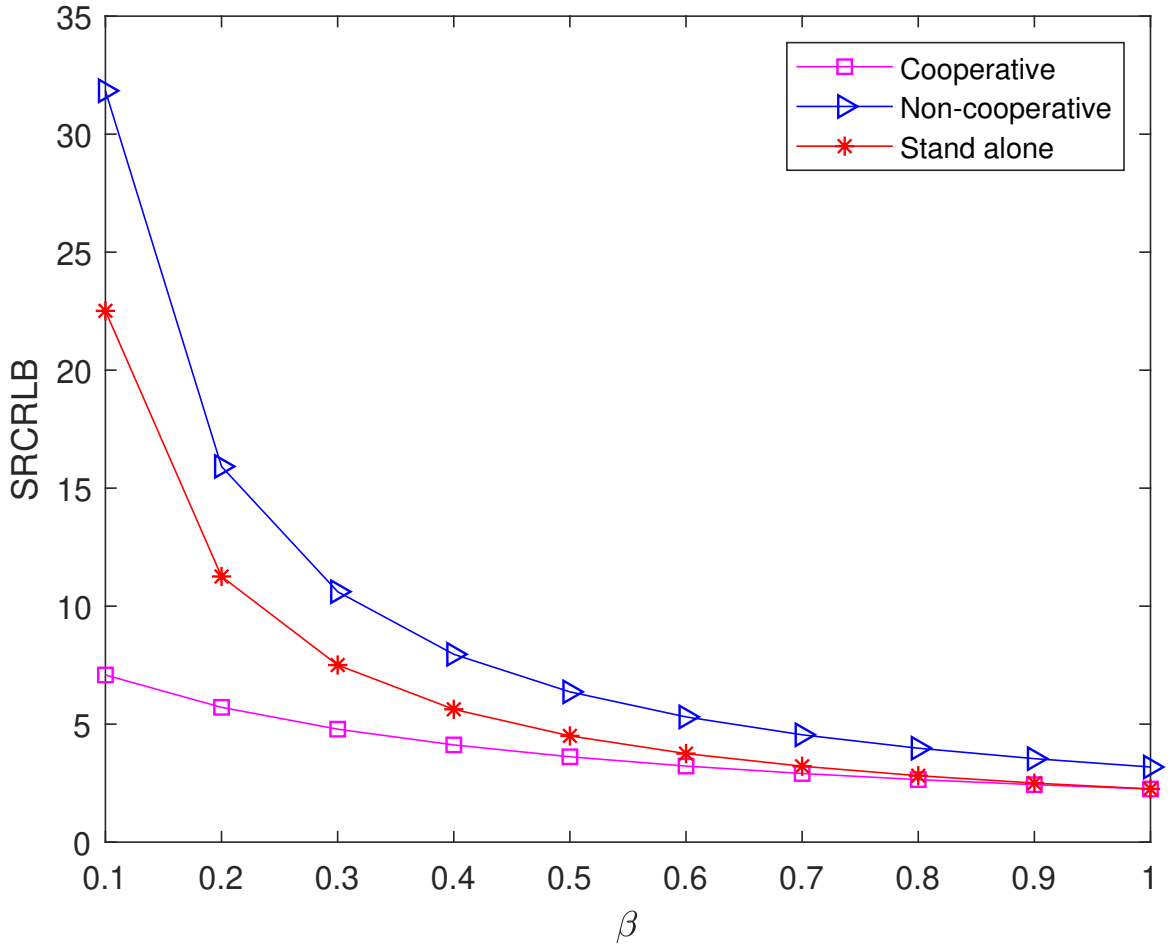
Figure 5.4: The static target estimation performance with varying β.

spectrum sharing scenario in terms of CRLB. The cooperation between the radar and the communication system allows the radar to use target reflected signals results from the communication transmitter and improve the target estimation performance. The target state is assumed to be dynamic, starts at 1 s and ends at 50 s. The sampling time of the radar assumed is 1 s. Since the FIM accumulates over time, the estimation accuracy increases in all the classes. These results agree with that of target tracking principles, where the filter is designed with the assumption of the Markov process. Moreover, it is worth noting that the cooperative case provides better results compared to the other two cases.

From all the Figures 5.3-5.5, it is observed that the cooperative case of RadComm spectrum sharing has a better performance when compared to non-cooperative and stand-alone cases. Due to the cooperative nature of the RadComm system, the target information received by the radar is improved owing to its own target returns and the returns due to the presence of the surrounding communication transmitter. Also,
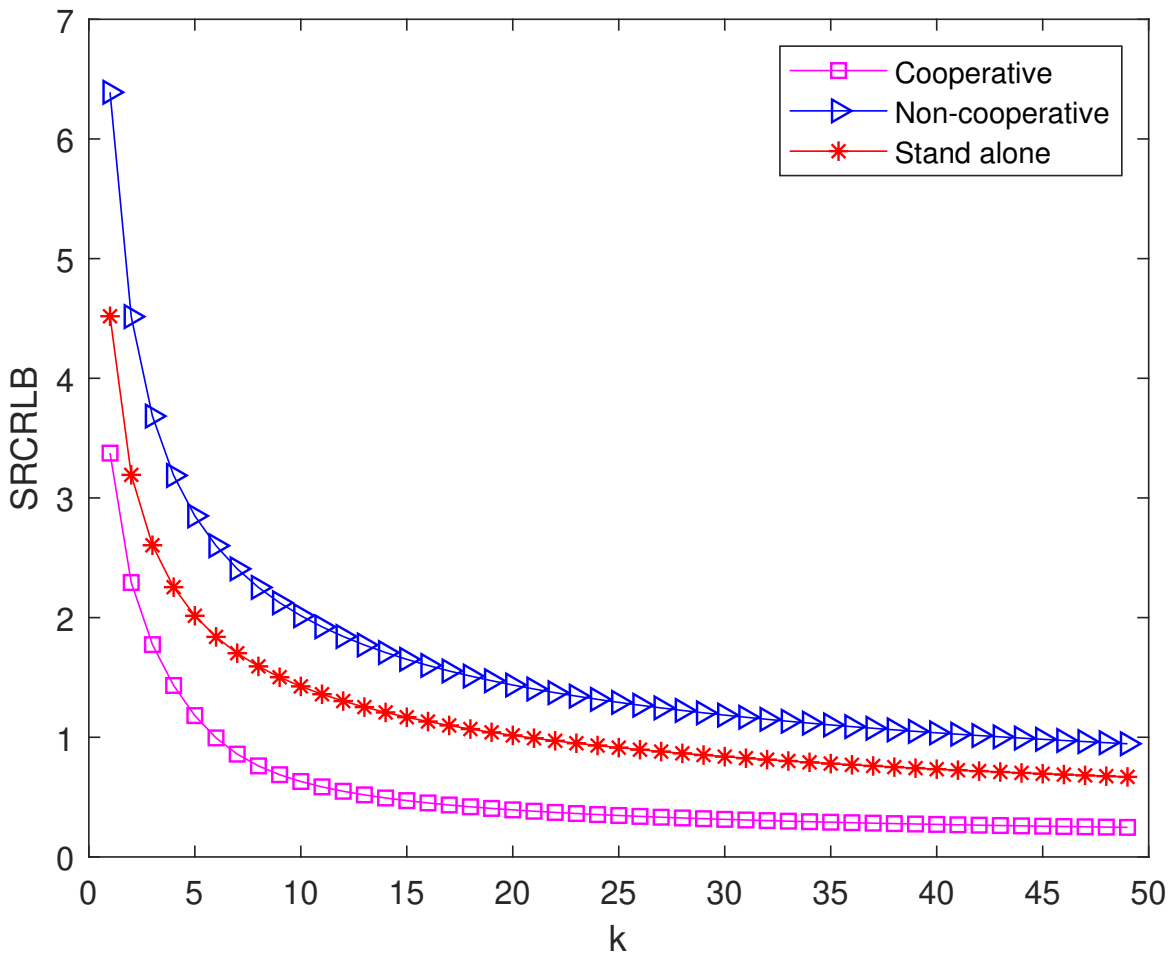
Figure 5.5: The dynamic target estimation performance.

it is observed that the target performance of the stand-alone case is higher than the non-cooperative case. It is true that, due to the presence of spectrum sharing communication transmitter, lack of cooperation and without adoption of any mitigation techniques makes, the radar is unable to use the target information results from the communication transmitter and treats it as additional noise.

Chapter 6

Conclusions and Future Directions

This Chapter presents the concluding remarks to the work described in this thesis. Also, it presents future research directions related to this work.

6.1   Concluding remarks

In this thesis, new detection structures are presented to detect radar targets in the presence of an in-band cyclostationay digital modulated wireless communication interference. The performances of the proposed detection rules have been thoroughly analysed by considering the target-reflected radar signals as deterministic, with random phase and with completely random amplitude and phase. Compared to the traditional sub-optimum detectors, performance results suggest that the proposed Neyman-Pearson (NP) based optimal detection structures achieve better performance in terms of probability of detection and probability of false alarm in all three cases. Also, a modified CFAR receiver structure is presented and compared with the modified NP based detector (optimal) and with standard detection (sub-optimal) methods. The results show that the modified structures provide better performance. As spectrum-sharing becomes more prevalent due to spectrum congestion, the proposed detection rules and receiver structures can be incorporated into existing systems rather than investing massive amounts in changing the complete hardware.

Further, this thesis presents a new measurement model for the radar and communication system (RadComm) spectrum sharing scenario and evaluates the target tracking performance. The new measurement model incorporates the radar returns and returns due to in-band wireless communication transmitters (IWCTs). Due to

the presence of IWCTs, a huge number of measurements are available in a given scan. For the obtained measurement set, the measurement to track association is carried out using GNN, whereas, for the filtering performance, EKF is considered in the tracker. The GNN-EKF based tracker is used to evaluate the tracking performance with metrics like false tracks, track breakages, and PRMSE. To provide the theoretical lower bound on the estimation accuracy, the PCRLB is considered for the proposed framework. Single radar and multiple radar cases are considered in the simulation scenario. Two different geometry frameworks are considered in a single radar case, where IWCTs are located near and far from the target and radar. The simulation results demonstrate that, in the presence of IWCTs, a huge number of tracks and track breakages are reported for the near geometry case. On the other hand, a few tracks are reported in the far geometry case. However, both cases have reported false tracks, which creates a delusion that more targets are present in the given surveillance. Multiple radar case is employed to eliminate the false tracks and determine the true target track. All the tracks reported by the multiple radars are first associated to find the true target track from each radar. Once the true target track of each radar is identified, T2TF is performed to determine an improved estimate of the true target track. In a RadComm spectrum sharing, for the multiple radar case, simulation results reveal that by performing T2TA and T2TF, the true target track is estimated with enhanced accuracy. It is evident from the results that the RMSE of the target estimates agrees with PCRLBs.

In addition, in this research work, spectrum sharing radar (SSR) is considered, assuming that a portion of the bandwidth is allocated for radar-only purposes and the rest for mixed-use of radar and communication purposes. The performance of the SSR has been analyzed in terms of mutual information (MI), spectral efficiency (SE), and capacity (C) metrics. These metrics are derived mathematically in a clean environment (no multipath) by considering SSR in the mixed-use band with and without a successive interference cancellation (SIC) scheme. Allocating a higher BW to the mixed-use band and employing the SIC scheme result in MI comparable to traditional radar. Similarly, for higher BW allocation to mixed-band, the SE of SSR outperforms conventional radar. The capacity of SSR in mixed-used and using SIC scheme reflects in comparable performance of traditional communication system. Later, the

multipath environment is considered between the target and receiver channels and mathematically modified the MI, SE, and C metrics to account for it. The influence of the correlation coefficient ρ has also been investigated. The numerical results of the SSR in a clean and multipath environment are plotted in terms of MI, SE, and C and compared with the traditional radar and communication system. Results reveal that the MI and C of the SSR using the SIC scheme in the mixed-use band is comparable to that of traditional radar and communication system, respectively. However, the SE of the SSR with the SIC scheme is improved. Further, results reveal that the performance metrics of SSR with correlation factor zero dominates the unity correlation factor in multipath environment. Furthermore, the results show that not using the SIC scheme in a mixed-use band degrades SSR performance compared to traditional systems. These findings and analyses serve as a guideline for SSR designers.

Moreover, a new cooperative RadComm spectrum sharing system model is considered to improve target estimation performance. The spectrum sharing radar received signal consists of target reflections due to both radar and communication transmitter being taken into account. The cooperation between the radar and the communication system allows the radar to use target reflected signals results from the communication transmitter and improve the target estimation performance. The target estimation performance is quantified with CRLB. Further, the impact of transmit signal energy and target reflection coefficient on the target estimation performance has been studied. The results reveal that the cooperative RadComm spectrum sharing provides an enhanced target estimation performance than the non-cooperative case of RadComm spectrum sharing and stand-alone radar system operation case.

The following section provides a summary of future research directions that may be carried out based on this study.

6.2   Future work

This thesis has limited the discussions to the theoretical performance analysis of the proposed detection structures for detecting radar targets in a RadComm environment. In the future, one can focus on the practical implementation of the proposed structures. This research assumed that the equalization/whitening filter parameters are

known. Thus, more work remains in the development of equalization/whitening filters for RadComm systems (Zilz and Bell, 2019). Further, this work can be extended to develop optimized detection rules by considering spectrum-sharing waveforms into account (Chiriyath *et al.*, 2019). Furthermore, this work can be extended by Swerling based radar cross section (RCS) reflection models and including the propagation effects etc..

This research identifies the true track of the target by considering the multiple radars. Further, it eliminates the information from IWCTs in a RadComm spectrum sharing scenario. Future studies can develop more sophisticated target tracking algorithms, where a single radar alone can identify the true targets in the RadComm spectrum sharing scenario. This work can also be extended by incorporating the information/ measurements received from surrounding IWCTs and improving the target estimation performance.

The performance analysis of spectrum sharing radar (SSR) work has optimized MI, SE and C performance metrics individually. This can be extended for the joint optimization of all performance metrics. In addition, one can work on multiple target scenarios of SSR, with targets having different target waveform response characteristics, introducing electronic countermeasures. Also, this work can be extended for the optimization of bandwidth, transmit powers and other quantities for trading the performance of radar and communication system.

The performance improvements in cooperative RadComm spectrum sharing work assume that the communication system shares the information that allows the radar to use target reflected signals, owing to communication transmitters. In the future, the work can be extended to achieve improved estimation performance, even in the case of non-cooperative RadComm spectrum sharing. Further, this work can be extended by incorporating the propagation effects between the target to receiver channel.

Appendix A

A.1

Define

$$f_{H_1}(q) = \mathbb{E}_\phi \left\{ f_{H_1}(q/\phi) \right\}, \tag{A.1}$$

$$f_{H_0}(q) = \mathbb{E}_\phi \left\{ f_{H_0}(q/\phi) \right\} \tag{A.2}$$

as the probability density functions of the test statistics q under the hypotheses H_1 and H_0, respectively, where $\mathbb{E}(.)$ is the expectation operator and ϕ is the uniform random variable over a period 0 to 2π.

With

$$g = \frac{1}{2} \int_T \frac{r(t)}{a(t)} \exp\left(-j\frac{2\pi Mt}{T}\right) dt = x + jy, \tag{A.3}$$

we have

$$q = |g| = \sqrt{x^2 + y^2} \tag{A.4}$$

We seek the densities of x and y to find the density of g defined in (A.3), which in turn results in the density of q defined in (A.4).

From (A.3), we have

$$
\begin{aligned}
\mathbb{E}\left(x/\phi, H_1\right) &= \frac{1}{2} \int_T Re\left\{\mathbb{E}\left(\frac{r(t)}{a(t)}\right) \exp\left(-j\frac{2\pi Mt}{T}\right)\right\} dt \\
&= \frac{1}{2} \int_T Re\left\{\frac{s(t)}{a(t)} \exp\left(-j\frac{2\pi Mt}{T}\right)\right\} dt \\
&= \frac{A}{2} \int_T \frac{\cos(\phi)}{a(t)} dt \\
&= \frac{A\upsilon}{2} \cos(\phi) \tag{A.5}
\end{aligned}
$$

where the complex envelop form of $s(t)$ defined in (2.57) is used and υ is given by

$$\upsilon = \int_T \frac{1}{a(t)} dt \tag{A.6}$$

Similarly, we have

$$\mathbb{E}\left(y/\phi, H_1\right) = \frac{A\upsilon}{2}\sin(\phi) \tag{A.7}$$

Also,

$$\mathbb{E}\left(x/\phi, H_0\right) = \mathbb{E}\left(y/\phi, H_0\right) = 0 \tag{A.8}$$

with the assumption that the interference statistic $s_I(t)$ has zero mean.

Also, we have

$$
\begin{aligned}
\sigma_a^2 &= \mathrm{Var}\left(x/\phi, H_1\right) \\
&= \frac{\langle s_{I_0}\rangle}{2}\int_T \frac{\cos^2\left(\frac{2\pi M t}{T}\right)}{a(t)}\,dt \\
&= \frac{\langle s_{I_0}\rangle}{2}\int_T \frac{\sin^2\left(\frac{2\pi M t}{T}\right)}{a(t)}\,dt \\
&= \mathrm{Var}\left(y/\phi, H_1\right)
\end{aligned} \tag{A.9}
$$

where Var(.) is the variance.

With the constraint that x, y are independent, we have

$$\mathrm{Cov}\left(f(x), g(x)\right) \triangleq \mathbb{E}\left\{\left[f(x) - \mathbb{E}(f(x))\right]\left[g(x) - \mathbb{E}(g(x))\right]\right\} \tag{A.10}$$

$$f_{H_1}(x, y) = \frac{1}{2\pi\sigma_a^2}\exp\left\{\frac{-\left[(x - \bar{x})^2 + (y - \bar{y})^2\right]}{2\sigma_a^2}\right\} \tag{A.11}$$

where $\bar{x}$ and $\bar{y}$ are the means of x and y defined in (A.5), (A.7), respectively, and σ_a^2 given in (A.9).

Similarly, under hypothesis H_0, we have

$$f_{H_0}(x, y) = \frac{1}{2\pi\sigma_a^2}\exp\left\{\frac{-(x^2 + y^2)}{2\sigma_a^2}\right\} \tag{A.12}$$

From (A.4), we have $q = |g|$ and, for some arbitrary phase angle β, we can write

$$g = x + jy = q\cos(\beta) + j\,q\sin(\beta) \tag{A.13}$$

From the transformation of random variable (DeGroot and Schervish, 2012; Mendenhall *et al.*, 2012; Rohatgi and Saleh, 2015), we can write

$$
\begin{aligned}
f_{H_1}(q, \beta/\phi) &= q f_{H_1}(x, y) \\
&= \frac{q}{2\pi\sigma_a^2}\exp\left\{-\frac{q^2 + (\bar{x}^2 + \bar{y}^2) - 2q(\bar{x}\cos(\beta) + \bar{y}\sin(\beta))}{2\sigma_a^2}\right\}
\end{aligned} \tag{A.14}
$$

To get $f_{H_1}(q)$ from (A.14), it needs to be integrated first over β and then over ϕ. For $\bar{x}$ and $\bar{y}$ given in (A.5) and (A.7), respectively, using (A.14) becomes

$$f_{H_1}(q/\phi) = \frac{q}{\sigma_a^2} \exp\left\{-\frac{q^2 + A^2 v^2/4}{2\sigma_a^2}\right\} I_0\left(\frac{Avq}{2\sigma_a^2}\right) \tag{A.15}$$

where $I_0(.)$ is the modified Bessel function of the first kind of order 0 (Abramowitz and Stegun, 1948).

Define

$$\zeta_a = \frac{Av}{2} \tag{A.16}$$

Finally, using (A.16) in (A.15), one can obtain $f_{H_1}(q)$, $f_{H_0}(q)$, as given in (2.68), (2.69), respectively.

A.2

To maximize the $I_{B_r}\left(z_r(t); g(t) \mid x(t)\right)$ with respect to transmit waveform energy constraint $\int_{B_r} |X(f)|^2 df = E_x$, form an objective function using the Lagrange multiplier theorem (Bertsekas, 2014) as

$$\Psi\left(|X(f)|^2\right) = T \int_{B_r} \ln\left[1 + \frac{4|X(f)|^2 \sigma_G^2(f)}{P_{ww}(f)T(1+\rho)}\right] df - \lambda\left(\int_{B_r} |X(f)|^2 df - E_x\right) \tag{A.17}$$

The equivalent/ reduced objective function which needs to be maximized with respect to $|X(f)|^2$ is

$$\psi\left(|X(f)|^2\right) = T \ln\left[1 + \frac{4|X(f)|^2 \sigma_G^2(f)}{P_{ww}(f)T(1+\rho)}\right] - \lambda|X(f)|^2 \tag{A.18}$$

For maximization, the partial differentiation of (A.18) with respect to $|X(f)|^2$ is taken and equated it to zero. It results,

$$|X(f)|^2 = D - \left(\frac{P_{ww}(f)T}{2\sigma_G^2(f)}\right)\left(\frac{1+\rho}{2}\right), \tag{A.19}$$

where $D = \frac{T}{\lambda}$ is some constant.

Using the energy constraint of $|X(f)|^2$ and (A.19), the value of D is given by

$$D = \frac{1}{B_r}\left[E_x + \int_{B_r}\left(\frac{P_{ww}(f)T}{2\sigma_G^2(f)}\right)\left(\frac{1+\rho}{2}\right)\right] \tag{A.20}$$

Using (4.6), (A.19), the maximum of $I_{B_r}(z_r(t); g(t) \mid x(t))$ is

$$
\begin{aligned}
I_{B_r}^{max}(z_r(t); g(t) \mid x(t)) &= T \int_{B_r} \ln\left[1 + \frac{4|X(f)|^2 \sigma_G^2(f)}{P_{ww}(f) T (1 + \rho)}\right] df \\
&= T \int_{B_r} \ln\left[1 + \frac{D - \left[r(f)\left(\frac{1+\rho}{2}\right)\right]}{r(f)\left(\frac{1+\rho}{2}\right)}\right] df \\
&= T \int_{B_r} \ln D - \ln\left[r(f)\left(\frac{1+\rho}{2}\right)\right] df \\
&= T B_r \ln D - T \int_{B_r} \ln\left[r(f)\left(\frac{1+\rho}{2}\right)\right] df \text{ (nats)}, \quad \text{(A.21)}
\end{aligned}
$$

where D is defined in (A.20).

Bibliography

Abramowitz, M. and **I. A. Stegun**, *Handbook of Mathematical Functions: With Formulas, Graphs, and Mathematical Tables*, volume 55. US Government printing office, 1948.

Ahmed, A., **Y. D. Zhang**, and **Y. Gu** (2018). Dual-function radar-communications using QAM-based sidelobe modulation. *Digital Signal Processing*, **82**, 166 – 174. ISSN 1051-2004.

Bakr, M. A. and **S. Lee** (2017). Distributed multisensor data fusion under unknown correlation and data inconsistency. *Sensors*, **17**(11). ISSN 1424-8220. URL `https://www.mdpi.com/1424-8220/17/11/2472`.

Bar-Shalom, Y. (1981). On the track-to-track correlation problem. *IEEE Transactions on Automatic Control*, **26**(2), 571–572.

Bar-Shalom, Y., **F. Daum**, and **J. Huang** (2009). The probabilistic data association filter. *IEEE Control Systems Magazine*, **29**(6), 82–100.

Bar-Shalom, Y., **X. R. Li**, and **T. Kirubarajan**, *Estimation with applications to tracking and navigation: Theory algorithms and software*. John Wiley & Sons, 2004.

Bar-Shalom, Y., **P. K. Willett**, and **X. Tian**, *Tracking and data fusion*, volume 11. YBS publishing Storrs, CT, USA, 2011.

Bell, M. R. (1993). Information theory and radar waveform design. *IEEE Transactions on Information Theory*, **39**(5), 1578–1597. ISSN 1557-9654.

Bertsekas, D. P., *Constrained optimization and Lagrange multiplier methods*. Academic press, 2014.

Bică, M. and **V. Koivunen** (2019). Radar waveform optimization for target parameter estimation in cooperative radar-communications systems. *IEEE Transactions on Aerospace and Electronic Systems*, **55**(5), 2314–2326.

Blackman, S. S. (2004). Multiple hypothesis tracking for multiple target tracking. *IEEE Aerospace and Electronic Systems Magazine*, **19**(1), 5–18.

Bliss, D. W., Cooperative radar and communications signaling: The estimation and information theory odd couple. *In 2014 IEEE Radar Conference*. 2014.

Blunt, S. D. and **E. S. Perrins** (eds.), *Radar and Communication Spectrum Sharing*. Radar, Sonar & Navigation. Institution of Engineering and Technology, 2018.

Bourgeois, F. and **J.-C. Lassalle** (1971). An extension of the Munkres algorithm for the assignment problem to rectangular matrices. *Communications of the ACM*, **14**(12), 802–804.

Carrick, M., **J. H. Reed**, and **C. M. Spooner** (2019). Mitigating linear-frequency-modulated pulsed radar interference to OFDM. *IEEE Transactions on Aerospace and Electronic Systems*, **55**(3), 1146–1159. ISSN 0018-9251.

Chen, L., **P. O. Arambel**, and **R. K. Mehra** (2002). Estimation under unknown correlation: Covariance intersection revisited. *IEEE Transactions on Automatic Control*, **47**(11), 1879–1882.

Cheng, Z., **C. Han**, **B. Liao**, **Z. He**, and **J. Li** (2018). Communication-aware waveform design for MIMO radar with good transmit beampattern. *IEEE Transactions on Signal Processing*, **66**(21), 5549–5562.

Chiriyath, A. R. and **D. W. Bliss**, Effect of clutter on joint radar-communications system performance inner bounds. *In 2015 49th Asilomar Conference on Signals, Systems and Computers*. 2015.

Chiriyath, A. R., **B. Paul**, and **D. W. Bliss** (2017). Radar-communications convergence: Coexistence, cooperation, and co-design. *IEEE Transactions on Cognitive Communications and Networking*, **3**(1), 1–12. ISSN 2332-7731.

Chiriyath, A. R., **S. Ragi**, **H. D. Mittelmann**, and **D. W. Bliss** (2019). Novel radar waveform optimization for a cooperative radar-communications system. *IEEE Transactions on Aerospace and Electronic Systems*, **55**(3), 1160–1173. ISSN 0018-9251.

Cover, T. M. and **J. A. Thomas**, *Elements of Information Theory*. John Wiley & Sons, 2012.

DeGroot, M. H. and **M. J. Schervish**, *Probability and Statistics*. Pearson Education, Boston, MA, United States, 2012.

Deng, H. and **B. Himed** (2013). Interference mitigation processing for spectrum-sharing between radar and wireless communications systems. *IEEE Transactions on Aerospace and Electronic Systems*, **49**(3), 1911–1919. ISSN 0018-9251.

Deng, L., **Y. Rui**, **P. Cheng**, **J. Zhang**, **Q. T. Zhang**, and **M. Li** (2013). A unified energy efficiency and spectral efficiency tradeoff metric in wireless networks. *IEEE Communications Letters*, **17**(1), 55–58. ISSN 2373-7891.

Forecast, G. *et al.* (2019). Cisco visual networking index: Global mobile data traffic forecast update, 2017–2022. *Update*, **2017**, 2022.

Gardner, W. A., **A. Napolitano**, and **L. Paura** (2006). Cyclostationarity: Half a century of research. *Signal Processing*, **86**(4), 639–697. ISSN 0165-1684.

Geng, Z., **H. Deng**, and **B. Himed** (2015). Adaptive radar beamforming for interference mitigation in radar-wireless spectrum sharing. *IEEE Signal Processing Letters*, **22**(4), 484–488. ISSN 1070-9908.

Gradshteyn, I. S. and **I. M. Ryzhik**, *Table of Integrals, Series, and Products*. Academic Press, San Diego, United States, 2014.

Hansen, V. G. and **H. R. Ward** (1972). Detection performance of the cell averaging LOG/CFAR receiver. *IEEE Transactions on Aerospace and Electronic Systems*, **AES-8**(5), 648–652.

Hassanien, A., **M. G. Amin**, **E. Aboutanios**, and **B. Himed** (2019). Dual-function radar communication systems: A solution to the spectrum congestion problem. *IEEE Signal Processing Magazine*, **36**(5), 115–126.

Hassanien, A., **M. G. Amin**, **Y. D. Zhang**, and **F. Ahmad** (2016). Signaling strategies for dual-function radar communications: An overview. *IEEE Aerospace and Electronic Systems Magazine*, **31**(10), 36–45.

He, X., **R. Tharmarasa**, **T. Kirubarajan**, and **T. Thayaparan** (2013). A track quality based metric for evaluating performance of multitarget filters. *IEEE Transactions on Aerospace and Electronic Systems*, **49**(1), 610–616.

Hernandez, M., **A. Farina**, and **B. Ristic** (2006). PCRLB for tracking in cluttered environments: Measurement sequence conditioning approach. *IEEE Transactions on Aerospace and Electronic Systems*, **42**(2), 680–704.

Herschfelt, A. and **D. W. Bliss**, Spectrum management and advanced receiver techniques (SMART): Joint radar-communications network performance. *In IEEE Radar Conference*. 2018.

Jiang, W., **Y. Huang**, and **J. Yang** (2016). Automatic censoring CFAR detector based on ordered data difference for low-flying helicopter safety. *Sensors*, **16**(7), 1055.

Jiang, X., **K. Harishan**, **R. Tharmarasa**, **T. Kirubarajan**, and **T. Thayaparan** (2014). Integrated track initialization and maintenance in heavy clutter using probabilistic data association. *Signal processing*, **94**, 241–250.

Jordan, E. and **K. Balmain**, *Electromagnetic Waves and Radiating Systems*. Prentice-Hall Electrical Engineering Series. Prentice-Hall, New Jersey, United States, 1968.

Karami, E., **O. A. Dobre**, and **N. Adnani**, Identification of GSM and LTE signals using their second-order cyclostationarity. *In 2015 IEEE International Instrumentation and Measurement Technology Conference (I2MTC) Proceedings*. 2015. ISSN 1091-5281.

Kay, S., *Fundamentals of Statistical Signal Processing: Detection Theory*. Prentice Hall Signal Processing Series. Prentice-Hall PTR, United States, 1998. ISBN 9780135041352.

Khawar, A., **A. Abdelhadi**, and **T. Clancy**, *Spectrum Sharing Between Radars and Communication Systems: A MATLAB Based Approach*. SpringerBriefs in Electrical and Computer Engineering. Springer International Publishing, 2018. ISBN 9783319566849.

Kirubarajan, T., **H. Chen**, and **Y. Bar-Shalom** (2001). Parameter estimation and the CRLB with uncertain origin measurements. *Methodology and Computing in Applied Probability*, **3**(4), 387–410.

Kuan-Wen Huang, **M. Bică**, **U. Mitra**, and **V. Koivunen**, Radar waveform design in spectrum sharing environment: Coexistence and cognition. *In IEEE Radar Conference*. 2015.

Lathi, B. and **Z. Ding**, *Modern Digital and Analog Communication Systems*. Oxford Series in Electrical and Computer Engineering. Oxford University Press, 2018. ISBN 9780190686840.

Levanon, N. (1988). Radar principles. *John Wiley and Sons, New York*.

Liu, F., **C. Masouros**, **A. Li**, **T. Ratnarajah**, and **J. Zhou** (2018). MIMO radar and cellular coexistence: A power-efficient approach enabled by interference exploitation. *IEEE Transactions on Signal Processing*, **66**(14), 3681–3695. ISSN 1053-587X.

Ma, D., **N. Shlezinger**, **T. Huang**, **Y. Liu**, and **Y. C. Eldar**, Automotive dual-function radar communications systems: An overview. *In 2020 IEEE 11th Sensor Array and Multichannel Signal Processing Workshop (SAM)*. IEEE, 2020.

Mallick, M. and **B. La Scala** (2008). Comparison of single-point and two-point difference track initiation algorithms using position measurements. *Acta Automatica Sinica*, **34**(3), 258–265.

Mao, X., **Y. Yang**, **H. Hong**, and **W. Deng** (2016). Multi-domain collaborative filter for interference suppressing. *IET Signal Processing*, **10**(9), 1157–1168. ISSN 1751-9675.

Martone, A. and **M. Amin** (2021). A view on radar and communication systems coexistence and dual functionality in the era of spectrum sensing. *Digital Signal Processing*, **119**, 103135.

Mendenhall, W., **R. J. Beaver**, and **B. M. Beaver**, *Introduction to Probability and Statistics*. Cengage Learning, CA, United States, 2012.

Meng, H., **M. Hernandez**, **Y. Liu**, and **X. Wang** (2009). Computationally efficient PCRLB for tracking in cluttered environments: Measurement existence conditioning approach. *IET Signal Processing*, **3**(2), 133–149.

Munir, M. F., **A. Basit**, **W. Khan**, **A. Saleem**, and **A. Al-salehi** (2022). A comprehensive study of past, present, and future of spectrum sharing and information embedding techniques in joint wireless communication and radar systems. *Wireless Communications and Mobile Computing*, **2022**.

Musicki, D. and **T. L. Song** (2013). Track initialization: Prior target velocity and acceleration moments. *IEEE Transactions on Aerospace and Electronic Systems*, **49**(1), 665–670.

Nartasilpa, N., **A. Salim**, **D. Tuninetti**, and **N. Devroye** (2018). Communications system performance and design in the presence of radar interference. *IEEE Transactions on Communications*, **66**(9), 4170–4185. ISSN 0090-6778.

Nartasilpa, N., **D. Tuninetti**, **N. Devroye**, and **D. Erricolo**, Let's share commrad: Effect of radar interference on an uncoded data communication system. *In 2016 IEEE Radar Conference (RadarConf)*. 2016.

Nuttall, A. (1975). Some integrals involving the Q_M-function. *IEEE Transactions on Information Theory*, **21**(1), 95–96. ISSN 0018-9448.

Paisana, F., **N. J. Kaminski**, **N. Marchetti**, and **L. A. DaSilva** (2017). Signal processing for temporal spectrum sharing in a multi-radar environment. *IEEE Transactions on Cognitive Communications and Networking*, **3**(2), 123–137.

Paisana, F., **G. A. Ropokis**, **N. Marchetti**, and **L. A. DaSilva** (2018). Cognitive beamforming in radar bands. *IEEE Transactions on Communications*, **66**(8), 3623–3637. ISSN 0090-6778.

Patel, P. and **J. Holtzman** (1994). Analysis of a simple successive interference cancellation scheme in a DS/CDMA system. *IEEE journal on selected areas in communications*, **12**(5), 796–807.

Paul, B. and **D. W. Bliss**, Extending joint radar-communications bounds for FMCW radar with doppler estimation. *In 2015 IEEE Radar Conference (Radar-Con)*. 2015.

Paul, B., **A. R. Chiriyath**, and **D. W. Bliss** (2017). Survey of RF communications and sensing convergence research. *IEEE Access*, **5**, 252–270.

Poor, H. V., *An Introduction to Signal Detection and Estimation*. Springer Science & Business Media, New York, United States, 2013.

Proakis, J. G. and **M. Salehi**, *Digital Communications*. McGraw-Hill, Boston, MA, United States, 2007. ISBN 9780072957167.

Qian, J., **M. Lops**, **X. Wang**, and **Z. He** (2018). Joint system design for coexistence of MIMO radar and MIMO communication. *IEEE Transactions on Signal Processing*, **66**(13), 3504–3519. ISSN 1053-587X.

Raghavan, R. (1992). Analysis of CA-CFAR processors for linear-law detection. *IEEE Transactions on Aerospace and Electronic Systems*, **28**(3), 661–665.

Ram, S. S., **S. Singhal**, and **G. Ghatak** (2022). Optimization of network throughput of joint radar communication system using stochastic geometry. *Front. Sig. Proc. 2: 835743. doi: 10.3389/frsip*.

Reinhardt, M., **B. Noack**, and **U. D. Hanebeck**, Closed-form optimization of covariance intersection for low-dimensional matrices. *In 2012 15th International Conference on Information Fusion*. IEEE, 2012.

Richards, M. A., *Fundamentals of Radar Signal Processing, Second Edition*. Tata McGraw-Hill Education, New York, United States, 2014.

Richards, M. A., **J. A. Scheer**, and **W. A. Holm** (eds.), *Principles of Modern Radar: Basic Principles*. Radar, Sonar & Navigation. Institution of Engineering and Technology, 2010.

Rohatgi, V. K. and **A. M. E. Saleh**, *An Introduction to Probability and Statistics*. John Wiley & Sons, New York, United States, 2015.

Rohling, H. (1983). Radar CFAR thresholding in clutter and multiple target situations. *IEEE Transactions on Aerospace and Electronic Systems*, **AES-19**(4), 608–621.

Sahin, C., **J. Jakabosky**, **P. M. McCormick**, **J. G. Metcalf**, and **S. D. Blunt**, A novel approach for embedding communication symbols into physical radar waveforms. *In 2017 IEEE Radar Conference (RadarConf)*. 2017.

Sanders, F. H., **R. L. Sole**, **B. L. Bedford**, **D. Franc**, and **T. Pawlowitz** (2006). Effects of RF interference on radar receivers. *NTIA Report*, (06-444).

Seybold, J. S., *Introduction to RF Propagation*. John Wiley & Sons, New York, United States, 2005.

Shajaiah, H., **A. Abdelhadi**, and **C. Clancy**, Spectrum sharing approach between radar and communication systems and its impact on radar's detectable target parameters. *In IEEE 81st Vehicular Technology Conference (VTC Spring)*. 2015. ISSN 1550-2252.

Shi, C., **F. Wang**, **M. Sellathurai**, **J. Zhou**, and **S. Salous** (2018). Power minimization-based robust OFDM radar waveform design for radar and communication systems in coexistence. *IEEE Transactions on Signal Processing*, **66**(5), 1316–1330.

Sijs, J., **M. Lazar**, and **P. Bosch**, State fusion with unknown correlation: Ellipsoidal intersection. *In Proceedings of the 2010 American Control Conference*. IEEE, 2010.

Sinha, A., **Z. Ding**, **T. Kirubarajan**, and **M. Farooq** (2012). Track quality based multitarget tracking approach for global nearest-neighbor association. *IEEE Transactions on Aerospace and Electronic Systems*, **48**(2), 1179–1191.

Smith, D. and **S. Singh** (2006). Approaches to multisensor data fusion in target tracking: A survey. *IEEE transactions on knowledge and data engineering*, **18**(12), 1696–1710.

Smith, M. and **P. Varshney** (2000). Intelligent CFAR processor based on data variability. *IEEE Transactions on Aerospace and Electronic Systems*, **36**(3), 837–847.

Sneh, A., **S. Jain**, **V. Sindhu**, **S. S. Ram**, and **S. Darak** (2022). IEEE 802.11 ad based joint radar communication transceiver: Design, prototype and performance analysis. *arXiv preprint arXiv:2209.04235*.

Steele, J. M., *The Cauchy-Schwarz Master Class: An Introduction to the Art of Mathematical Inequalities*. Cambridge University Press, New York, NY, USA, 2004.

Tang, A., **S. Li**, and **X. Wang** (2021). Self-interference-resistant IEEE 802.11 ad-based joint communication and automotive radar design. *IEEE Journal of Selected Topics in Signal Processing*, **15**(6), 1484–1499.

Tian, T., **T. Zhang**, **L. Kong**, **G. Cui**, **Q. Shi**, and **Y. Deng**, Performance of localization estimation rate for radar-communication system. *In IEEE Radar Conference*. 2019*a*. ISSN 1097-5659.

Tian, T., **T. Zhang**, **L. Kong**, **G. Cui**, and **Y. Wang**, Mutual information based partial band coexistence for joint radar and communication system. *In IEEE Radar Conference*. 2019*b*. ISSN 1097-5659.

Tian, T., **T. Zhang**, **G. Li**, and **T. Zhou** (2019). Mutual information-based power allocation and co-design for multicarrier radar and communication systems in co-existence. *IEEE Access*, **7**, 159300–159312.

Tian, X., **Y. Bar-Shalom**, and **G. Chen**, A no-loss covariance intersection algorithm for track-to-track fusion. *In Signal and Data Processing of Small Targets 2010*, volume 7698. International Society for Optics and Photonics, 2010.

Tichavsky, P., **C. Muravchik**, and **A. Nehorai** (1998). Posterior Cramer-Rao bounds for discrete-time nonlinear filtering. *IEEE Transactions on Signal Processing*, **46**(5), 1386–1396.

Tsinos, C. G., **A. Arora**, **S. Chatzinotas**, and **B. Ottersten** (2021). Joint transmit waveform and receive filter design for dual-function radar-communication systems. *IEEE Journal of Selected Topics in Signal Processing*, **15**(6), 1378–1392.

Van Trees, H., **K. Bell**, and **Z. Tian**, *Detection Estimation and Modulation Theory, Part I: Detection, Estimation, and Filtering Theory*. Detection Estimation and Modulation Theory. Wiley, New York, United States, 2013. ISBN 9781118539705.

Wang, B., **R. Xie**, **H. Xu**, **J. Zhang**, **H. Han**, **Z. Zhang**, **L. Liu**, and **J. Li** (2020). Target localization and tracking using an ultra-wideband chaotic radar with wireless synchronization command. *IEEE Access*, **9**, 2890–2899.

Whalen, A. D., *Detection of Signals in Noise*. Academic Press, San Diego, United States, 2013.

Woodward, P. M., *Probability and Information Theory, with Applications to Radar: International Series of Monographs on Electronics and Instrumentation*, volume 3. Elsevier, 2014.

Zhang, J. A., **F. Liu**, **C. Masouros**, **R. W. Heath**, **Z. Feng**, **L. Zheng**, and **A. Petropulu** (2021a). An overview of signal processing techniques for joint communication and radar sensing. *IEEE Journal of Selected Topics in Signal Processing*.

Zhang, J. A., **M. L. Rahman**, **K. Wu**, **X. Huang**, **Y. J. Guo**, **S. Chen**, and **J. Yuan** (2021b). Enabling joint communication and radar sensing in mobile networks-A survey. *IEEE Communications Surveys & Tutorials*.

Zhang, Q., **X. Wang**, **Z. Li**, and **Z. Wei** (2021*c*). Design and performance evaluation of joint sensing and communication integrated system for 5G MmWave enabled CAVs. *IEEE Journal of Selected Topics in Signal Processing*, **15**(6), 1500–1514.

Zheng, L., **M. Lops**, **Y. C. Eldar**, and **X. Wang** (2019). Radar and communication coexistence: An overview: A review of recent methods. *IEEE Signal Processing Magazine*, **36**(5), 85–99.

Zheng, L., **M. Lops**, and **X. Wang** (2018). Adaptive interference removal for uncoordinated radar/communication coexistence. *IEEE Journal of Selected Topics in Signal Processing*, **12**(1), 45–60. ISSN 1932-4553.

Zilz, D. P. and **M. R. Bell** (2018). Statistical modeling of wireless communications interference and its effects on adaptive-threshold radar detection. *IEEE Transactions on Aerospace and Electronic Systems*, **54**(2), 890–911. ISSN 0018-9251.

Zilz, D. P. and **M. R. Bell** (2019). Optimal linear detection of signals in cyclostationary, linearly modulated, digital communications interference. *IEEE Transactions on Aerospace and Electronic Systems*, **55**(3), 1123–1145. ISSN 0018-9251.

List of Publications

1. G. Srinath, Prashantha Kumar H., P. Srihari, R. Tharmarasa and T. Kirubarajan, "**Coherent Radar Target Detection With In-Band Cyclostationary Wireless Interference**," in IEEE Access, vol. 10, pp. 11173-11190, 2022, doi: 10.1109/ACCESS.2022.3144696.

2. G. Srinath, B. Pardhasaradhi, Prashantha Kumar H. and P. Srihari, "**Tracking of Radar Targets With In-Band Wireless Communication Interference in RadComm Spectrum Sharing**," in IEEE Access, vol. 10, pp. 31955-31969, 2022, doi: 10.1109/ACCESS.2022.3159623.

3. G. Srinath, B. Pardhasaradhi, Ashok Mahipathi, Prashantha kumar H, P. Srihari and Linga Reddy. R. C, "**Performance Analysis of Spectrum Sharing Radar in Multipath Environment**," in IEEE Open Journal of the Communications Society, doi: 10.1109/OJCOMS.2023.3240116.

4. G. Srinath, B. Pardhasaradhi, Prashantha Kumar H. and P. Srihari, "**Target Estimation Performance Improvement in Cooperative Radar and Communication system Spectrum Sharing**," 2021 12th International Conference on Computing Communication and Networking Technologies (ICCCNT), 2021, pp. 1-6, doi: 10.1109/ICCCNT51525.2021.9580023.

Biography

Gunnery Srinath received the B.Tech. degree in electronics and communication engineering from Jawaharlal Nehru Technological University, Anantapur, India, in 2013, the M.Tech. degree in digital communication from ABV-IIITM, Gwalior, India, in 2016, and the Ph.D. degree in electronics and communication engineering with the National Institute of Technology Karnataka Surathkal, Mangalore, India. From 2018 to 2019, he was a Visiting Ph.D. Student with the Estimation, Tracking and Fusion Research Laboratory (ETFL), McMaster University, Hamilton, ON, Canada. He is currently working as a Technical Specialist at ADAS, Continental Autonomous Mobility India Pvt. Ltd., Bengaluru. His research interests include cognitive radio, radar signal processing, convergence of RF communication and sensing, simultaneous localization and mapping (SLAM), and target tracking.